EXPERIMENTAL STUDY ON RECTANGULAR BARGE IN BEAM SEA

A Dissertation

by

KWANG HYO JUNG

Submitted to the Office of Graduate Studies of
Texas A&M University
in partial fulfillment of the requirements for the degree of

DOCTOR OF PHILOSOPHY

May 2004

Major Subject: Ocean Engineering

EXPERIMENTAL STUDY ON RECTANGULAR BARGE IN BEAM SEA

A Dissertation

by

KWANG HYO JUNG

Submitted to Texas A&M University
in partial fulfillment of the requirements
for the degree of

DOCTOR OF PHILOSOPHY

Approved as to style and content by:

Kuang-An Chang (Chair of Committee)	Hamn-Ching Chen (Member)
Cheung Hun Kim (Member)	Gerald L. Morrison (Member)
	Paul Roschke (Head of Department)

May 2004

Major Subject: Ocean Engineering

ABSTRACT

Experimental Study on Rectangular Barge in Beam Sea. (May 2004)
Kwang Hyo Jung, B.S.; M.S., Pusan National University
Chair of Advisory Committee: Dr. Kuang-An Chang

This study presents laboratory observations of flow characteristics for regular waves passing a rectangular barge in a two dimensional wave tank. The rectangular barge was fixed and free to roll (one degree of freedom) in a beam sea. Particle image velocimetry (PIV) was employed to measure the velocity field in the vicinity of the structure. The mean velocity and turbulence properties were obtained by phase-averaging the velocity profiles from repeated test runs. The quantitative flow characteristics were represented to elucidate the coupled interactions between the regular wave and the barge in roll motion or fixed condition. Additionally, the turbulence properties including the turbulence length scale and the turbulent kinetic energy budget were investigated to characterize the flow pattern due to the wave interaction. Because all the data including wave elevations, roll motion, and dynamic pressure were synchronized with velocity profiles, the results between the roll motion and the fixed condition were compared. The viscous effects due to the flow separation depend on the relative relation between the wave water particle motion and the roll motion of the barge. The viscous damping mechanism that reduces the roll motion at the roll natural period wave is illustrated. It shows that the vortex flow was mainly induced by the roll motion. For wave periods longer than the roll natural period, the flow was separated in different directions accompanying the roll natural period wave. The longer waves may help the roll motion with the vortex flow predominantly separated by the wave water particle motion rather than the barge motion. This may be called the viscous exciting effect. Moreover, the variations of dynamic pressures near the corners were measured and analyzed along with the viscous effect for both the roll motion and the fixed barge cases.

DEDICATION

To my lovely wife Mi Jeong Kim and son Ho Joon Jung

for their endless love, patience, and devotion

and also to my parents and parents-in-law

ACKNOWLEDGMENTS

I would like to express my sincere gratitude to my advisor, Dr. Kuang-An Chang, not only for his advice but also for his encouragement and help during my whole study. I would also like to thank Dr. Cheung Hun Kim, Hamn-Ching Chen, and Dr. Gerald L. Morrison for their help and guidance as my committee members. I appreciate all the professors of the Coastal and Ocean Engineering Division in the Civil Engineering Department. In particular, I would like to thank Dr. Billy L. Edge for providing me the opportunity to work with him and for his support. I heartily acknowledge that I owe numerous favor to Mr. John Reed in the laboratory.

I would like to express my heartfelt thanks to Dr. Hyo Jae Jo for his help in finding a way out of difficulty in my study. I am grateful to Dr. Sun Hong Kwon and Dr. Jong Sung Yoon for their counsel and encouragement. I would also like to express my appreciation to Dr. Ho Hwan Chun and Dr. Jung Hwan Chung in Korea who inspired me to study harder. Special thanks go to my colleagues, Yong Uk Ryu and Ho Joon Lim, who assisted me in the arduous work in the laboratory. The help and friendship of Hae Jin Choi, Seung Jae Lee, and Hee Sung Lee are sincerely acknowledged. Also, I am thankful to Mr. Kent D. McLeod for the English corrections in my dissertation.

I have no word to express my deepest gratitude for my parents and my parents-in-law who have devoted themselves to support my study. Also, I offer my sister, brother-in-law, brother, and sister-in-law my heartfelt thanks for their love. I am sure that I could not have realized this work without the steadfast love of my wife, Mi Jeong Kim, and my son, Ho Joon Jung. I would like to express my thanks and love to them with my whole heart and soul.

Although I cannot name all the people who have helped me on this page, I am deeply grateful to them for their supports and concerns for me.

TABLE OF CONTENTS

CHAPTER Page

LIST OF FIGURES

FIGURE Page

LIST OF TABLES

Table Page

CHAPTER I

INTRODUCTION

The floating and submerged rectangular or circular structures have been constructed for the purpose of the coastal and ocean engineering for decades. Also, floating structures in seas have played a crucial role in transporting cargos for military and civilian uses. All the structures installed in ocean or coastal environments have interacted with the gravity wave. A variety of ships, offshore structures, and the like have been investigated in the 6-degree of freedom motion to study the interactions between the waves and the structures. The wave interaction has disturbed the fluid flow to be vortical and turbulent in the vicinity of structures. The flow pattern due to the interaction between the wave and the motion of floating structures is very complicated and has a significant effect on the behavior of structures. The roll motion, unlike other motions, is highly nonlinear because of the roll damping effect. Therefore, it is not easy to evaluate the roll damping quantitatively due to the difficulty to quantify the viscous effect in the vicinity of the structures. In this study, the vortical and turbulent flow characteristics due to the wave interaction is going to be investigated with the comparison between the rectangular structure in the roll motion and the fixed condition.

Various investigations have been conducted to better understand the vortical and turbulent problems of the flow around the surface piercing structures due to wave interactions. Numerous analytical, numerical and experimental studies have been reported on the problem of wave-circular cylinder interaction. Typically, vortices and turbulence were generated in the vicinity of the cylinder. Sarpkaya (1968) formulated the relationship between the vortices and loading on a circular cylinder analytically through the use of a potential flow model. Lighthill (1986) demonstrated the feasibility of separating the hydrodynamic loads on offshore structures into the vortex-induced forces and the potential-flow forces. Bearman *et al*. (1985) provided a method to decompose

---

This dissertation follows the style and format of the Journal of Ocean Engineering.

the forces on a structure into three parts: due to the inertia of the accelerating flow, due to the influence of the viscous boundary layer, and due to the effect of the vortex shedding.

Several numerical models were developed to investigate the flow around submerged or floating structures. Milne-Thomson's circle theorem was used to study the characteristics of a two-dimensional irrotational flow around a horizontal cylinder under long-crested waves by Chaplin (1981), while the discrete vortex method was employed by Sarpkaya (1989). Braza *et al*. (1986) presented numerical simulations on the flow field at the near wake of a circular cylinder based on a finite volume velocity-pressure formulation of the unsteady Navier-Stokes equations. A Navier-Stokes time-stepping model was employed to compute the orbital flow motion around a circular cylinder by Chaplin (1993).

One of the typical floating structures in seas is the breakwater which was categorized for its limitations and some design considerations by Bruce and McCartney (1985). Fugazza and Natale (1988) presented the energy losses and floating breakwater responses in comparison between experiments and a linear model. Williams and Abul-Azm (1997) and Williams *et al.* (2000) applied linear potential theory to calculate the hydrodynamic properties of floating pontoon breakwaters of rectangular section. Mays (1999) analyzed the wave attenuation caused by breakwaters that consisted of submerged and moored horizontal cylinders using linear potential theory. Chen *et al*. (2002) simulated vortex structures and flow separation patterns for a partially submerged pontoon structure using the Reynolds averaged Navier-Stokes (RANS) equations in conjunction with a domain decomposition approach. Chang *et al*. (2001) studied vortex generation and evolution by interactions of a solitary wave and a submerged rectangular obstacle using particle image velocimetry (PIV) and a RANS model.

The viscous effect caused by the flow separation is known to heavily influence the roll motion of a blunt-shaped floating structure. Potential flow theories, although reproduceing the heave and pitch motions very well, are much less effective in predicting the roll motion due to the negligence of fluid viscosity and rotation. This shortfall is normally compensated by introducing a viscous roll damping coefficient. However, it is not a simple task in finding a proper viscous damping coefficient owing to its highly nonlinear nature. Current practice often turns to empirical formulas that require extensive laboratory or field experiments. Yet the results, either experimentally or theoretically, have not demonstrated consistencies with the physical reality featuring the viscous phenomenon. A rational approach, such as some CFD based simulation models, to determine the viscous damping is therefore highly desirable. Cozen (1987) simulated the vortex shedding from the bilges of rolling ships using computational models with forced oscillations in the calm water. Yeung *et al.* (1998) proposed a composite roll moment equation to address separately the wave damping and the viscous damping related to flow separations. Chen *et al*. (2002) studied vortex structures and flow separation using a Reynolds-averaged Navier-Stokes (RANS) model in conjunction with a domain decomposition approach in an attempt to simulate the roll motion of a free floating pontoon barge. Chakrabarti (2001) further decomposed the roll damping coefficient for a ship hull form to the skin friction of the hull, eddy shedding from the hull, free surface waves, lift effect damping, and bilge keel damping. Flow separations are remarkable at the sharp edges of a blunt body such as the rectangular structure (hull) in the present study. These phenomena with the presence of surface waves have been investigated experimentally and theoretically by Roddier *et al*. (2000). The effect of viscous damping is significant on the roll motion at a frequency near the roll natural frequency. According to Yeung and Liao (1999), it could reduce the roll response amplitude as much as one half. Ikeda *et al.* (1977) proposed an empirical formula in which the eddy making component of the roll damping force for a two-dimensional body is proportional to the square of its frequency. They deduced the amplitude of roll motion from the semi-experimental technique based on theoretical and experimental results.

With substantial advances in fluid measurement techniques in recent years, particle image velocimetry (PIV) is now capable of measuring fluid velocity fields at a sufficient resolution to determine the structures of vortex and turbulence in the flow. Using PIV, the origination of vorticity in a wave field and its relationship to the flow near the free surface and the shape of the waves were addressed by Rood (1994) and Dabiri and Gharib (1997). Dong *et al*. (1997) applied the PIV technique to study the flow structure near the bow of a ship model subject to surface waves. Unal *et al*. (1997) computed the instantaneous force using the quantitative imaging of vortex shedding from a cylinder with a momentum-based method. Oshkai and Rockwell (1999) extended Lighthill's (1986) work to calculate the effective force acting on a cylinder under waves using the spatial and temporal evolution of the instantaneous velocity field around the cylinder. Yeung *et al*. (1996) measured the flow pattern generated by a plate undergoing a forced harmonic roll motion at the free surface using the PIV technique. They followed with a numerical simulation to reproduce the observed flow pattern of the rolling rectangular cylinder using the random vortex method with the presence of the free surface (Yeung *et al*. 1998). Based on the results, they proposed a composite roll moment equation that separately addresses the effect of wave damping and quadratic damping associated to vortex generation induced by a rectangular cylinder that undergoes periodic rolling motion at the free surface. Although a significant amount of research has studied the wave-structure interaction problem numerically or experimentally, it was rarely included and examined that the vortical flow pattern and turbulence characteristics were associated with the interaction between the wave and the roll motion of the structure.

The purpose of this study is the investigation of the wave interaction with the rectangular barge in the roll motion and the fixed condition. The flow profile obtained by PIV technique is represented to understand the vortical and turbulent flow characteristics due to the wave interaction in the roll motion and the fixed condition. Also, its turbulent structure is illustrated with turbulent length scale analysis and the turbulent kinetic energy budget. Because the mechanism of vortex generation is illustrated in the relative roll motion of the barge under the wave condition, it helps to understand the viscous effect on the roll motion with the relative motion to the wave. This can show the different result with the traditional experimental method like the forced motion in calm water which was not including the wave exiting force and the relative motion for the incident wave. Although the roll viscous damping effect to reduce the motion is not quantified in this study, it is presented that its generation process is demonstrated at the different wave frequency including the roll natural frequency.

CHAPTER II

EXPERIMENTAL INSTRUMENTATION AND TECHNIQUE

2.1 Laboratory facilities

The experiments were performed in a glass-walled wave tank that is 36 m long, 0.9 m wide, and 1.2 m deep as shown in Fig. 2.1. A 1:5.5 sloping beach was installed at the end of the tank. A layer of horsehair was placed on the beach to absorb the wave energy and reduce reflection. The wavemaker is of dry back flap type. The flap is driven by a synchronous servo-motor controlled by a computer and hydrostatically balanced using an automatic near constant force and a pneumatic control system.

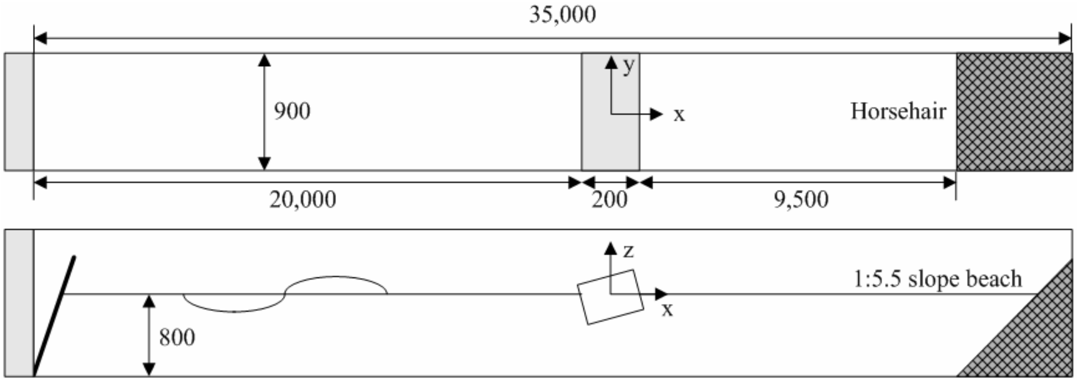

Fig. 2.1 Sketch of the wave tank (unit: mm).

Three double-wired resistant-type wave gauges were used to measure the free surface elevation. The signal from the wave gauges was converted to voltage and sent to a data acquisition board housed in a computer. Two gauges were located at 4 cm in front and behind the rectangular structure, respectively, to measure the wave elevation at the PIV fields of view. The third wave gage was placed at 3 m behind the barge to measure the transmitted wave. A rotary position sensor was utilized to measure the rotating motion of the barge induced by the wave. Its full range was ±60° and the combined error, a sum of a linearity error and a nonrepeatability error, is less than 0.2 % of the full scale output. Pressure information at 2 locations near each barge corner was measured with piezoresistive pressure transducers, which have a combined error less than 1% of the full scale output. All data from wave gages, the rotary position sensor, and pressure gages were measured at a sampling rate of 100 Hz.

PIV was used to map the velocity field in the study. The PIV system used in this study is sketched in Fig. 2.2. The PIV system and the wavemaker were synchronized by the computer A housing a data acquisition board (National Instruments AT-AO-6/10) which generated analog output DC voltage. The timing of laser pulses was controlled by the CCD camera by the computer B housing the Programmable-Timing-Unit-Board (Fig. 2.2). Also, the control signals of the PIV system and the wavemaker were synchronized with all the data from wave gages, pressure transducers, and a rotary position sensor.

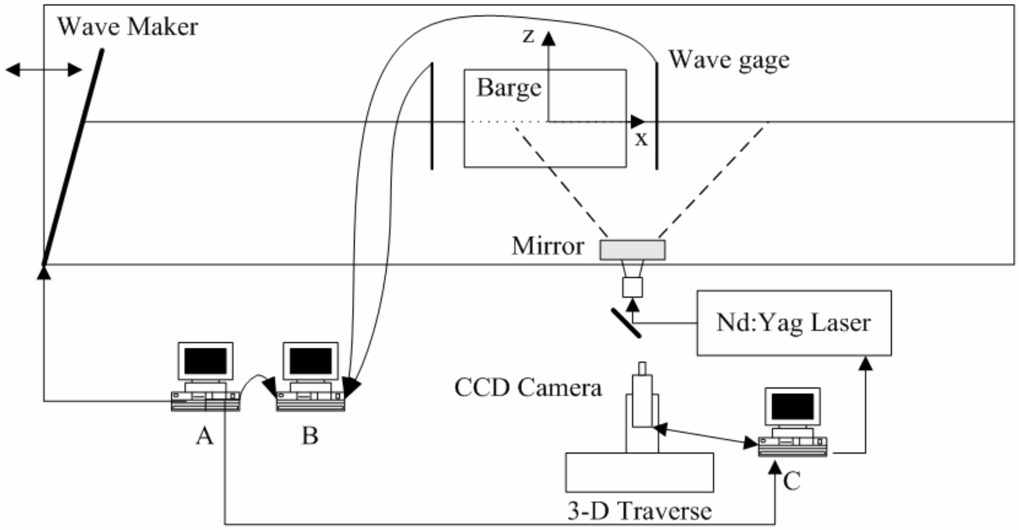

Fig. 2.2 Schematic sketch of the experimental set-up. Computer A: to control the wavemaker and trigger the PIV system. Computer B: to take data from wave gages, a rotary position sensor, and pressure gages. Computer C: to control the laser and CCD camera.

2.2 Particle image velocimetry technique

Particle image velocimetry (PIV) was employed to measure the velocity profile in the experiment. The PIV technique is a non-intrusive, indirect, and whole field method. Therefore, no probe was used to disturb the fluid in the experiment. Artificial seeding particle is added for velocity measurement, and thousands of velocity vectors can be obtained simultaneously.

In the experiment, the PIV illumination source was a dual-head Spectra-Physics Nd:YAG laser. The laser contains a crystal harmonic generator that is used to generate the frequency doubled 532 nm green light from the original 1064 nm invisible light. The laser has a maximum energy output of 400 mJ/pulse in the 532nm wavelength, a pulse duration of 10 ns, and a repetition rate of 10 Hz in each head so that 20 pulses are generated per second. The light sheet optic used a combination of two spherical lenses and one cylindrical lens to generate a thin light sheet (about 1mm) from the 3-mm diameter laser beam (Fig. 2.3).

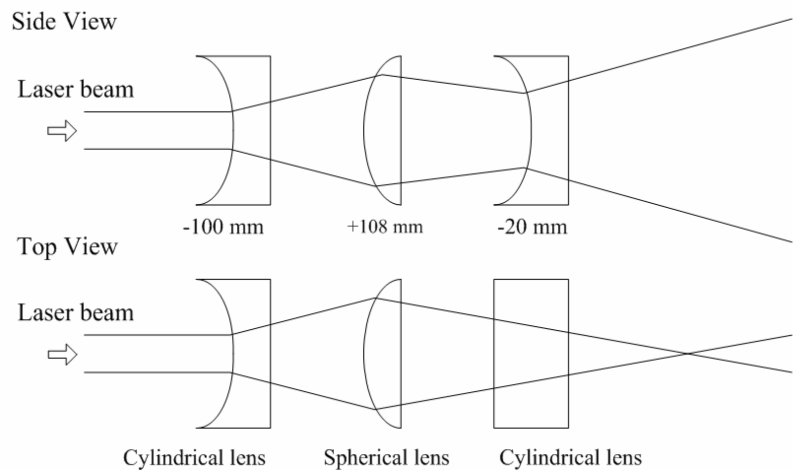

Fig. 2.3 Sketch of the light sheet optics.

Vestosint 2157 natural which is made of polyamid 12 was used as the seeding particle which has a mean diameter of 57μm and a specific weight of 1.02. Particle image diameter (d_τ) can be estimated by (Adrian, 1995)

$$d_\tau = \sqrt{M^2 d_p^2 + d_{diff}^2} \tag{2.2.1}$$

where M is the magnification factor which is the ratio of the width of the CCD sensor to the width of the field of view, d_p the particle diameter, and d_{diff} the diffraction limited minimum image diameter is given by

$$d_{diff} = 2.44(1+M)f_{\#}\lambda \tag{2.2.2}$$

where $f_{\#}$ is the *f*-number of the lens and λ is the wave length of the light. The measurement uncertainty (RMS random error) in digital cross-correlation PIV evaluation is related to the particle image diameter (Raffel *et al.* 1998). Because the conditions have been slightly changed in each experiment (3 different sets of experiments in this study), the measurement uncertainty will be discussed in each case.

The camera used to capture images is a digital CCD (Charge-Coupled Device) camera mounted with a 105mm f/1.8 micro focal lens set at f/2.8~4.0. It has 1280×1024 pixels, a 6.7μm×6.7 μm pixel size, 12 bit dynamic range, and 8 Hz framing rate. The PIV images were recorded by the double-frame/single-pulsed method shown in Fig. 2.4.

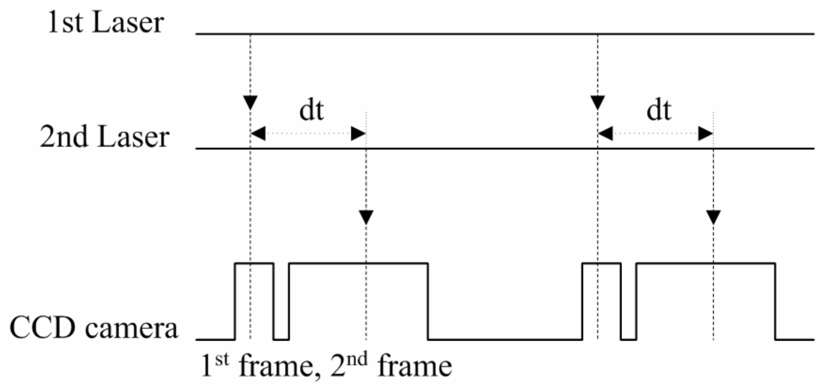

Fig. 2.4 Image recording method: double-frame/single-pulsed method.

The main advantage of this technique is to remove the directional ambiguity. The time difference (*dt*) between the 1st frame and 2nd frame was adjusted to be about 3~5 ms, which was determined by the maximum displacement to be less than a third of the width of the interrogation window size. A pair of images (1280×1024 pixels, *dt*= 5 ms) obtained by the double-frame/single-pulsed method is shown in Fig. 2.5.

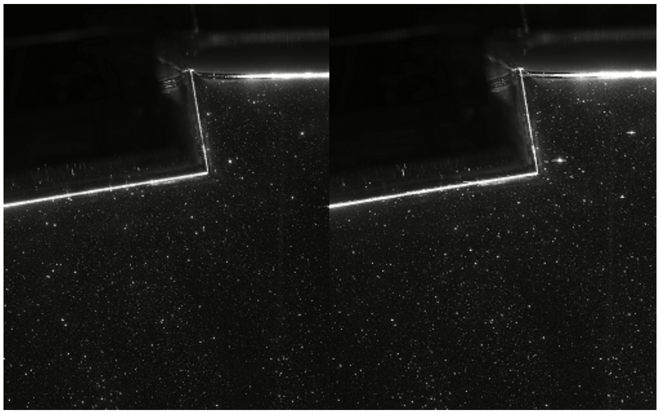

Fig. 2.5 Pair of images taken by the double-frame/single-pulsed method.

A pair of PIV images (in Fig. 2.5) was used to compute the velocity field using the commercial software (DaVis) from LaVision. The background noise was subtracted before the evaluation of velocity vectors. The complex 2-D fast Fourier transform was calculated from the two small areas (called interrogation windows), and the result was multiplied by its complex conjugate. Then, the inverse FFT was applied to yield the cross correlation function. The use of FFT can simplify and significantly speed up the cross-correlation process of two interrogation windows from a pair of images (Willert and Gharib, 1991). The adaptive multi-pass algorithm was applied to reduce faulty vectors. Firstly, it has calculated a reference velocity vector for each rectangle section which was an initial cell size (four times of an interrogation area). At the next step, this reference velocity vector was used as a cell shift to compute the more accurate vector field. Because this method has shifted an interrogation area to the location where particles moved, the stronger cross-correlation can be taken. Once the velocity vectors have been calculated in the interrogation area (32 × 32 pixels) with a 50% overlap, spurious false vectors were eliminated by the median filter (Westerweel, 1994). The left-over empty spaces were filled-up with interpolated vectors and smoothed by a simple 3×3 smoothing filter to reduce noise.

CHAPTER III

VORTICITY OF MEAN FLOW AND TURBULENCE ENERGY EQUATION

The mean velocity, turbulence intensity, and turbulent kinetic energy were obtained by phase-averaging the measured instantaneous velocities at each phase, i.e.,

$$\langle u_k \rangle = \frac{1}{N}\sum_{l=1}^{N} u_k^{(l)} = U_k \tag{3.1}$$

where the symbol $\langle\ \rangle$ represents phase average, $u_k^{(l)}$ the *k*-component velocity obtained from the l^{th} instantaneous velocity measurement, *N* the total number of instantaneous velocities at that phase, and U_k the phase-averaged mean velocity.

By definition the vorticity is related to the circulation by Stokes theorem

$$\Gamma = \oint U \cdot dl = \int (\nabla \times U) \cdot dS = \int \Omega \cdot dS \tag{3.2}$$

where l describes the path of integration around a surface S, Γ the circulation, and Ω the vorticity. The vorticity for a fluid element is computed by reducing the surface S to zero and applying Stokes theorem to the *xz*-gridded PIV velocity data (Raffel and Willert, 1998). The following formula provides the vorticity at the point (*i*, *j*) was obtained based on the circulation calculated using its eight neighboring points, i.e.,

$$(\Omega_y)_{i,j} \hat{=} \frac{\Gamma_{i,j}}{4dxdz} \quad \text{with} \quad \begin{aligned} \Gamma_{i,j} = {} & \frac{1}{2}dx\left(u_{i-1,j-1} + 2u_{i,j-1} + u_{i+1,j-1}\right) \\ & + \frac{1}{2}dz\left(w_{i+1,j-1} + 2w_{i+1,j} + w_{i+1,j+1}\right) \\ & - \frac{1}{2}dx\left(u_{i+1,j+1} + 2u_{i,j+1} + u_{i-1,j+1}\right) \\ & - \frac{1}{2}dz\left(w_{i-1,j+1} + 2w_{i-1,j} + w_{i-1,j-1}\right) \end{aligned} \tag{3.3}$$

Equation (3.3) is equivalent to applying the center difference scheme to a smoothed (3×3kernel) velocity field (Westerweel, 1993). With uncorrelated velocity, the uncertainty estimated in the vorticity reduces to $\varepsilon_\Omega \approx 0.61\varepsilon_u / dx$ which is less than $\varepsilon_\Omega \approx \varepsilon_u / dx$ for center differences or $\varepsilon_\Omega \approx 1.34\varepsilon_u / dx$ for the Richardson extrapolation method (Raffel and Willert, 1998).

Using Reynolds decomposition, the instantaneous velocity can be decomposed into the mean velocity and turbulent fluctuations as following

$$u_i = \langle u_i \rangle + u_i' \tag{3.4}$$

where prime denotes turbulent fluctuations. Because only two velocity components were measured, the turbulence intensity is defined as

$$I = \langle u'u' + w'w' \rangle^{1/2} \tag{3.5}$$

where u' and w' are the velocity fluctuations in the x and z directions, respectively.

To investigate the turbulent kinetic energy budget, each term in the transport equation for turbulent kinetic energy needs to be measured or estimated. The equation is as following (Tennekes and Lumley, 1972)

$$\frac{\partial k_t}{\partial t} = \underbrace{-U_j \frac{\partial k_t}{\partial x_j}}_{\text{advection}} \underbrace{- \frac{\partial}{\partial x_j} \frac{1}{\rho} \langle u_j' p' \rangle}_{\substack{\text{pressure}\\ \text{transport}}} \underbrace{- \frac{\partial}{\partial x_j} \left\langle \frac{1}{2} u_i' u_i' u_j' \right\rangle}_{\substack{\text{turbulent}\\ \text{transport}}} - \underbrace{\langle u_i' u_j' \rangle S_{ij}}_{\substack{\text{turbulent}\\ \text{production}}} - \underbrace{2\nu \langle s_{ij} s_{ij} \rangle}_{\substack{\text{turbulent}\\ \text{dissipation}}} \tag{3.6}$$

where k_t is the turbulent kinetic energy, p' the pressure fluctuation, ρ the density of fluid, and ν the kinematic viscosity. k_t is approximated as

$$k_t \approx \frac{1.33}{2} \langle u'u' + w'w' \rangle = \frac{1.33}{2} I^2 \tag{3.7}$$

in which the coefficient 1.33 came from the assumption that the flow around the rectangular structure is similar to a plane wake (Svendsen, 1987). Note that the viscous diffusion term was neglected due to its small magnitude compared to the rest of the terms at a large Reynolds number. In the equation, the mean rate of strain S_{ij} and the fluctuating rate of strain s_{ij} are defined as

$$S_{ij} \equiv \frac{1}{2}\left(\frac{\partial U_i}{\partial x_j} + \frac{\partial U_j}{\partial x_i} \right), \quad s_{ij} \equiv \frac{1}{2}\left(\frac{\partial u_i'}{\partial x_j} + \frac{\partial u_j'}{\partial x_i} \right) \tag{3.8}$$

Equation (3.6) states that the time rate of change of turbulent kinetic energy is balanced by the mean flow convective transport, the turbulent pressure transport, the turbulent transport, the turbulent production, and the turbulent dissipation. The pressure transport term was neglected in the study, partly because the pressure fluctuation tends to be poorly correlated with the velocity fluctuation except near the wall (Townsend, 1956), and partly because of the inability of measuring it inside the fluid body. Accordingly, the transport equation for the turbulent energy budget can be reduced to

$$\frac{\partial k_t}{\partial t} = A + T + P - \varepsilon \tag{3.9}$$

in which A, T, P and ε represent the turbulent advection, turbulent transport, turbulent production, and turbulent dissipation, respectively.

In this study, the turbulent dissipation rate was estimated using the assumption of isotropic turbulence, i.e.

$$\varepsilon = 15\nu \left\langle \left(\frac{\partial u'}{\partial x} \right)^2 \right\rangle \tag{3.10}$$

CHAPTER IV

WAVE INTERACTIONS WITH FIXED RECTANGULAR BARGE

4.1 Experimental condition

A wooden rectangular structure that was 0.900 m long (L), 0.200 m wide (B), and 0.064 m high (T_B) was used in the experiments. The structure with a length extended across the entire width of the wave tank was fixed at the position 20 m from the wavemaker. The draft (D) was fixed at 0.032 m and the water depth (h) was kept as 0.800 m throughout the experiments. The wavemaker generated regular waves of 1.0 second wave period (T), 0.040 m wave height (H), and 1.56 m wave length (λ) in the experiments therefore the experiments were conducted close to a deep-water condition of $h/\lambda > 0.5$. Two double-wired resistant-type wave gauges were used with the sampling rate set at 100 Hz. One wave gauge was placed at 4 cm in front of the structure while the other at 4 cm behind the structure to measure the free surface elevation at the structure and within the PIV fields of view at both the seaward and leeward sides. All the measurements were taken after the quasi-steady state was reached after running the wavemaker for more than 15 minutes. The Reynolds number ($Re = U_{\max} B / 2\nu$) is 2.25×10^4 in the experiments with $U_{\max}$ being the maximum wave particle velocity obtained from linear wave theory and ν the kinematic viscosity.

4.2 Data acquisition

The measurements were taken at about 30 minutes after the wave generator was started to ensure that the quasi-steady condition has been reached. This allows the mean flow and turbulence to be extracted using the phase-average method. Ninety pairs of images were taken at each phase for eight different phases for PIV velocity measurements. The velocity components (*u* and *w*) in the vortical and turbulent area were chosen to check the convergence of the mean velocity for the number of velocity samples used in the phase-averaging process (shown in Fig. 4.1). The mean velocities by the phase averaging became steady over sixty velocity profiles.

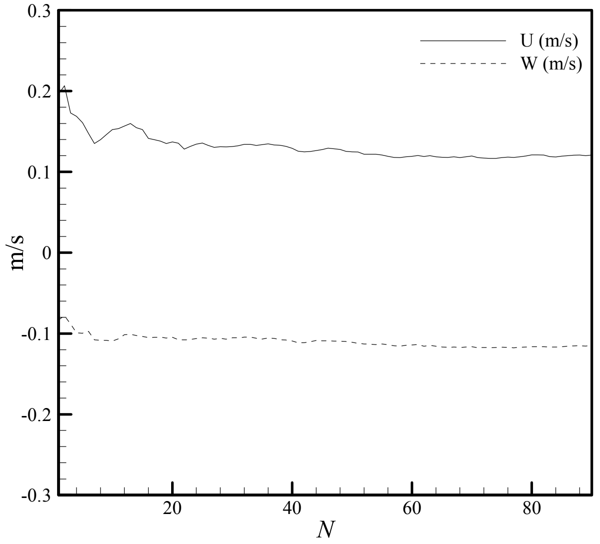

Fig. 4.1 Mean velocities for the number of velocity profiles used to average.

Four fields of view (FOV) were arranged to obtain the velocity field in the vicinity of each corner of the structure, as shown in Fig. 4.2. The sizes of the FOVs are 142×113 mm^2 for FOV 1 and FOV 2, and 57×47 mm^2 for FOV 3 and FOV 4. Note that the area covered by FOVs 1 and 2 are 6 times that of FOVs 3 and 4.

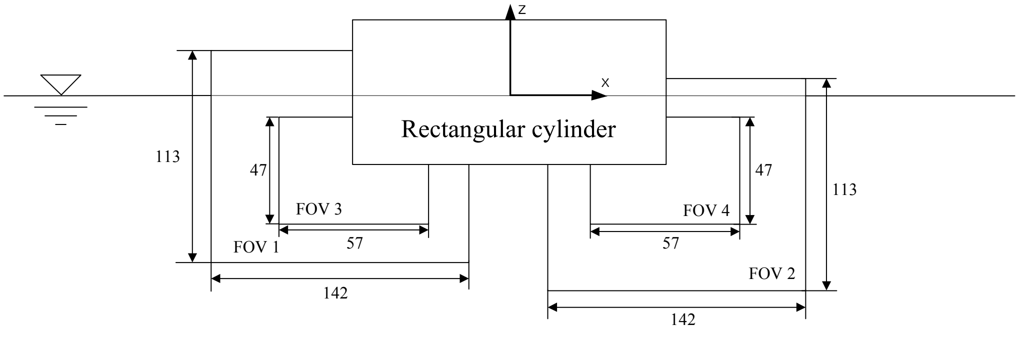

Fig. 4.2 PIV fields of view (unit: mm).

The two larger FOVs were used to cover the relatively large areas in which the major parts of vorticity and turbulence were induced and the free surface in the captured images. The two smaller FOVs were used to obtain more detailed velocity information with a better spatial resolution and accuracy because the flow characteristics, especially the vorticity and the turbulent energy budget, need to be examined for their variation of spatial resolution. In the experiments, images in FOVs 1 and 2 were captured at a short period of 0.05 seconds ahead of those in FOVs 3 and 4. The coordinate system is also shown in Fig. 4.1 with z = 0 being the stationary free surface elevation and x = 0 the center of the structure. The 32×32 pixels interrogation windows corresponded to a spatial resolution of 3.6×3.6 mm^2 for FOVs 1 and 2, and 1.48×1.48 mm^2 for FOVs 3 and 4. The time separation (*dt*) between the first and second laser pulses was 3.0 ms for FOVs 1 and 2 and 1.5 ms for FOVs 3 and 4.

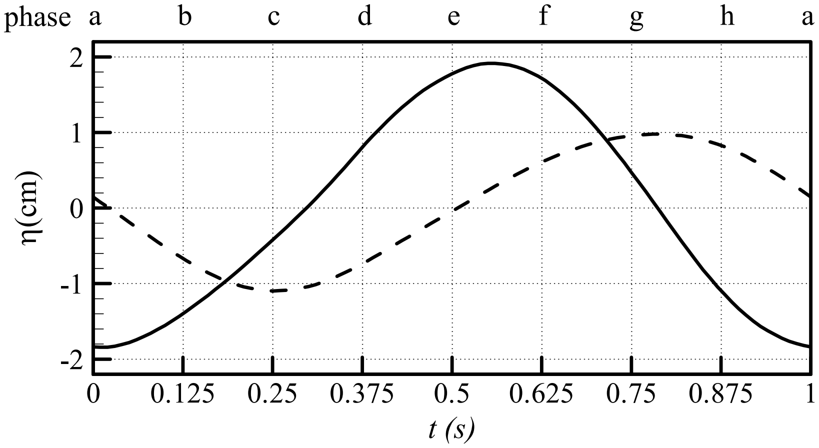

Fig. 4.3 Free surface profile measured at 4 cm in front of the structure (solid line) and 4 cm behind the structure (dashed line). The eight phases correspond to the timing of the PIV velocity measurements.

Fig. 4.3 shows the free surface profile taken using the wave gauges at a distance 4 cm from each side of the rectangular structure. The eight phases in the figure, namely phase “a” to phase “h”, correspond to the timing of PIV velocity measurements. Since the wave period was 1.0 s, the time interval between each PIV phase was 0.125 s. From the figure one can see that the seaward side free surface elevation is significantly higher than that of the leeward side. This indicates wave transmission is relatively low (which will be discussed later).

4.3 Experimental results

4.3.1 Energy transmission, reflection, and dissipation

Wave reflection and transmission due to the existence of the structure were measured because they implicitly stand for the amount of energy passing the structure. They were estimated from the wave elevation taken by wave gages under the assumption of an identical partition between the potential energy and the kinetic energy. To measure the transmission coefficient, two wave gauges were used with one located at 10 m in front of the rectangular structure (10 m from the wavemaker) and another located at 2 m behind the structure. The transmission coefficient, K_T, is defined as the ratio of the transmitted wave height (H_T) to the incident wave height (H_I). In the experiment, it was measured before the incident wave reflected from the beach and re-reflected from the wavemaker. The transmission coefficient was found to be 0.75 for $B/\lambda = 0.125$ which is close to the value of 0.7 in Fugazza and Natale (1988).

The reflection coefficient, K_R, was obtained when the quasi-steady state was reached. The wave elevation was measured by the wave gauges moving along the tank at every 5 cm for a distance of about one wavelength to find the values of maximum ($H_{\max}$) and minimum ($H_{\min}$) heights of the standing wave envelop (Hughes, 1993). The reflection coefficient is then obtained using

$$K_R = \frac{H_R}{H_I} = \frac{H_{\max} - H_{\min}}{H_{\max} + H_{\min}} \tag{4.1}$$

The reflection coefficient between the wavemaker and the rectangular structure was found to be 0.49, and the reflection coefficient between the structure and the horsehair covered beach was 0.06. Using linear wave theory, the transmitted energy

(K_T^2) is 0.56 and reflected energy (K_R^2) is 0.24. Therefore, the fixed structure in this experiment dissipated roughly 20% of the wave energy during the interaction. Note that the transmission coefficient was measured before the refection from the beach while the reflection coefficient was measured after the quasi-steady state was achieved. Therefore the amount of energy dissipated may not be exact.

4.3.2 Vorticity and turbulent kinetic energy

Fig. 4.4 shows the mean velocity, mean vorticity, and turbulent kinetic energy calculated using the phase averaged PIV measurements. The phases of the velocity maps from Figs. 4.4 (a) to (h) correspond to phases “a” to “h” shown in Fig. 4.2. The measurements were taken from FOVs 3 and 4 (the two smaller FOVs) so more accurate and detailed results on the generation and evolution of vortices and turbulent kinetic energy are displayed. The cycle from phase “a” to phase “h” provides the flow structure over one wave period. Note that only every other velocity vector in each row and column was plotted, i.e., only one-quarter of the total measured velocity vectors are displayed in each figure. Fig. 4.4 (a) corresponds to the instant that the wave trough is at the seaward side of the structure, and near zero down crossing at the leeward side. At the seaward side, the mean velocity shows a jet-like flow pattern between the two counter-rotating vortices near the lower corner of the structure. The negative vortex starts to separate from the structure corner. At the leeward side, a negative vortex also starts to separate from the structure corner. The positive vortices at both sides of the structure are convected seaward and decay gradually [evident from the next two phases in Figs. 4.4 (b) and 4.4 (c)]. The pattern of turbulent kinetic energy is consistent with that of vorticity at both sides. The two peaks of turbulent kinetic energy are very close to the peaks of vorticity at the seaward side. The pattern is not that clear at the leeward side, perhaps due to the spatial resolution of the measurement and the relative small size of the vortices. Fig. 4.4 (b) shows that the negative vortices generated in Fig. 4.4 (a) at both the seaward and leeward sides are convected seaward by the return flow.

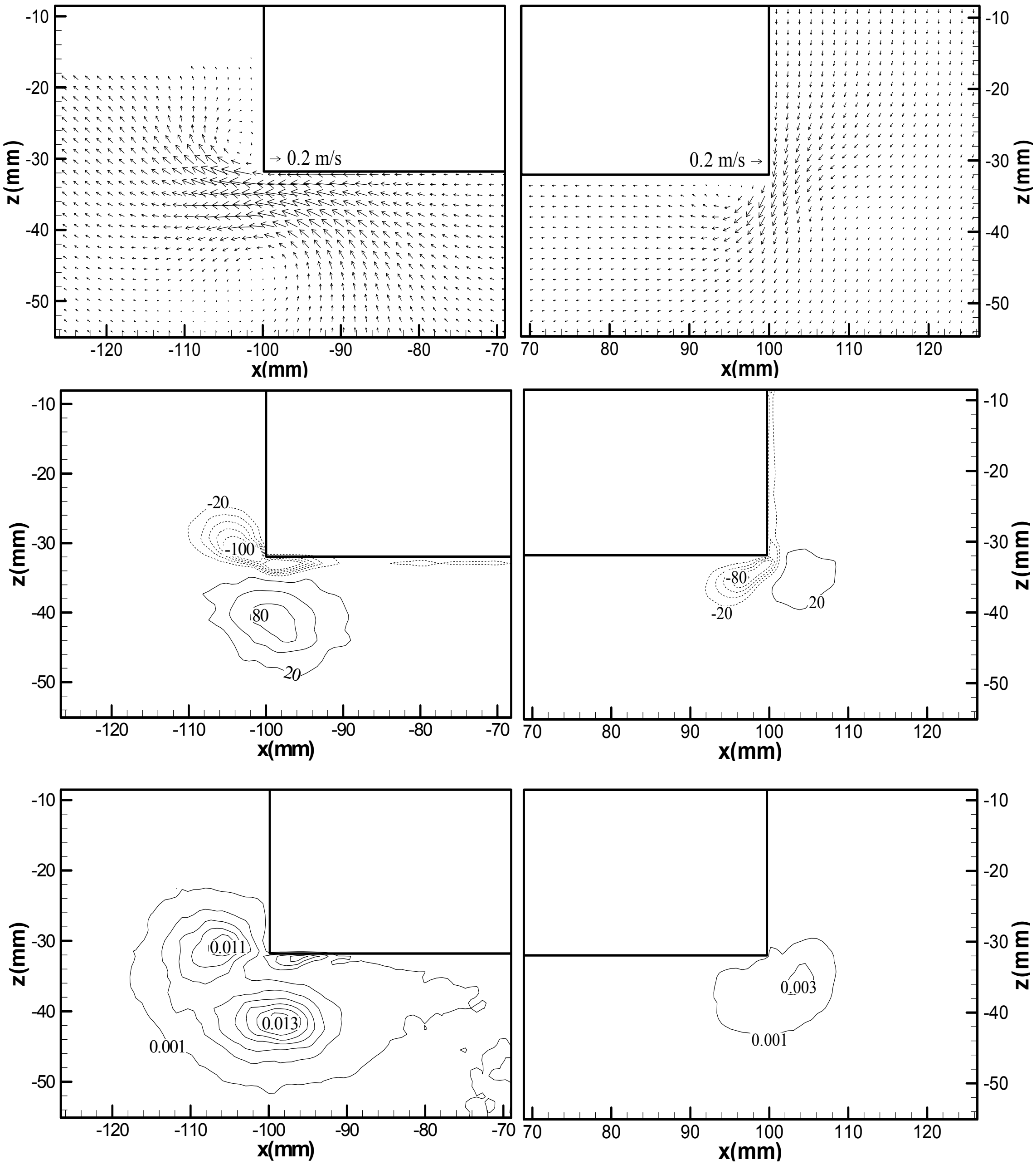

Seaward side Leeward side

(a)

Fig. 4.4 Mean velocity (the 1st row), mean vorticity (the 2nd row), and turbulent kinetic energy (the 3rd row). Figs. (a) to (h) correspond to phases "a" to "h" in figure 4.2. The solid and dashed contour lines in the vorticity plots represent the positive and negative vorticity, respectively, with an increment of $\Delta\Omega = 10\ s^{-1}$ between the lines. The contour lines of turbulent kinetic energy have an increment of $\Delta k_t = 0.002\ m^2/s^2$ between the lines.

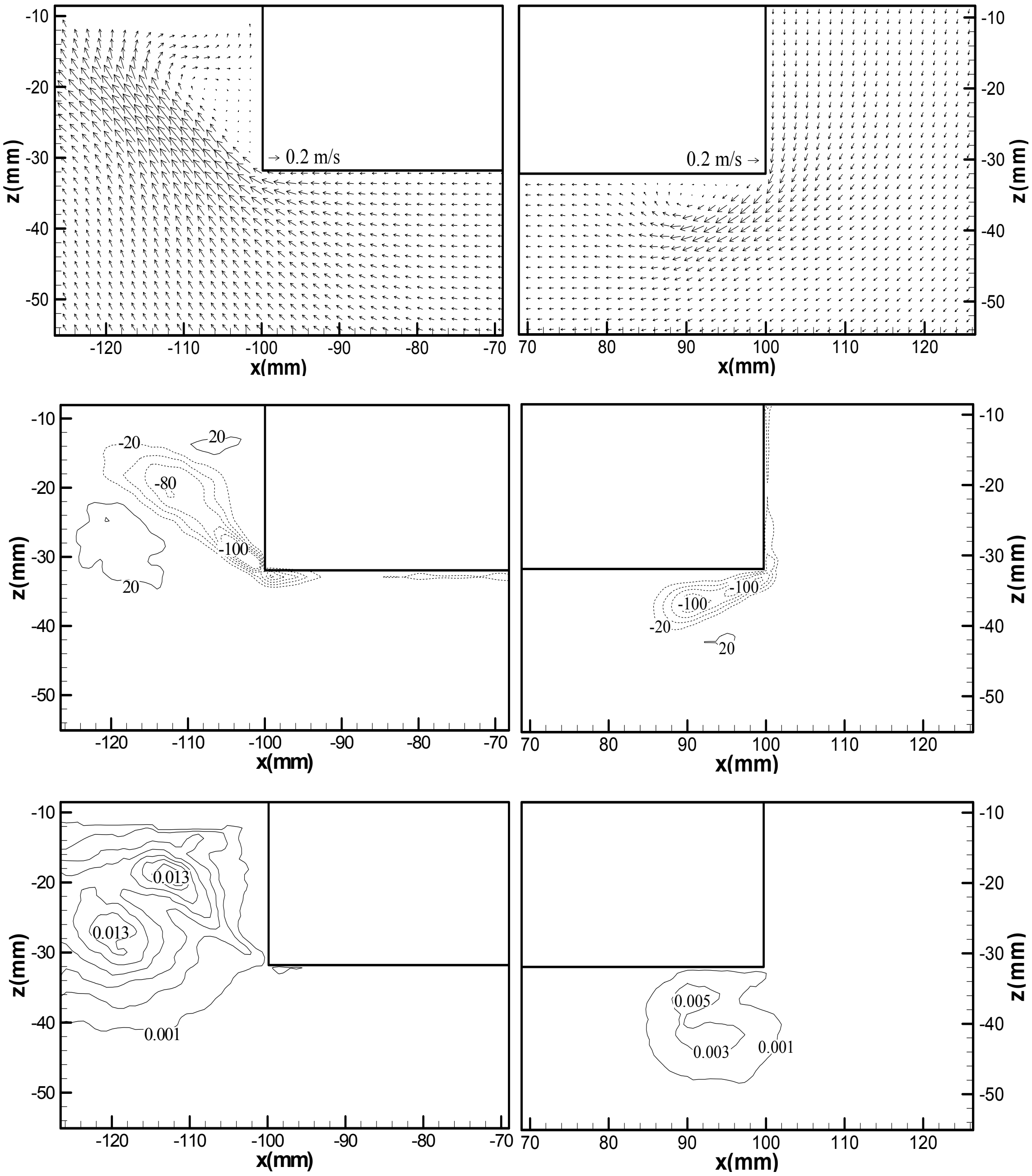

Seaward side Leeward side

(b)

Fig. 4.4 Continued

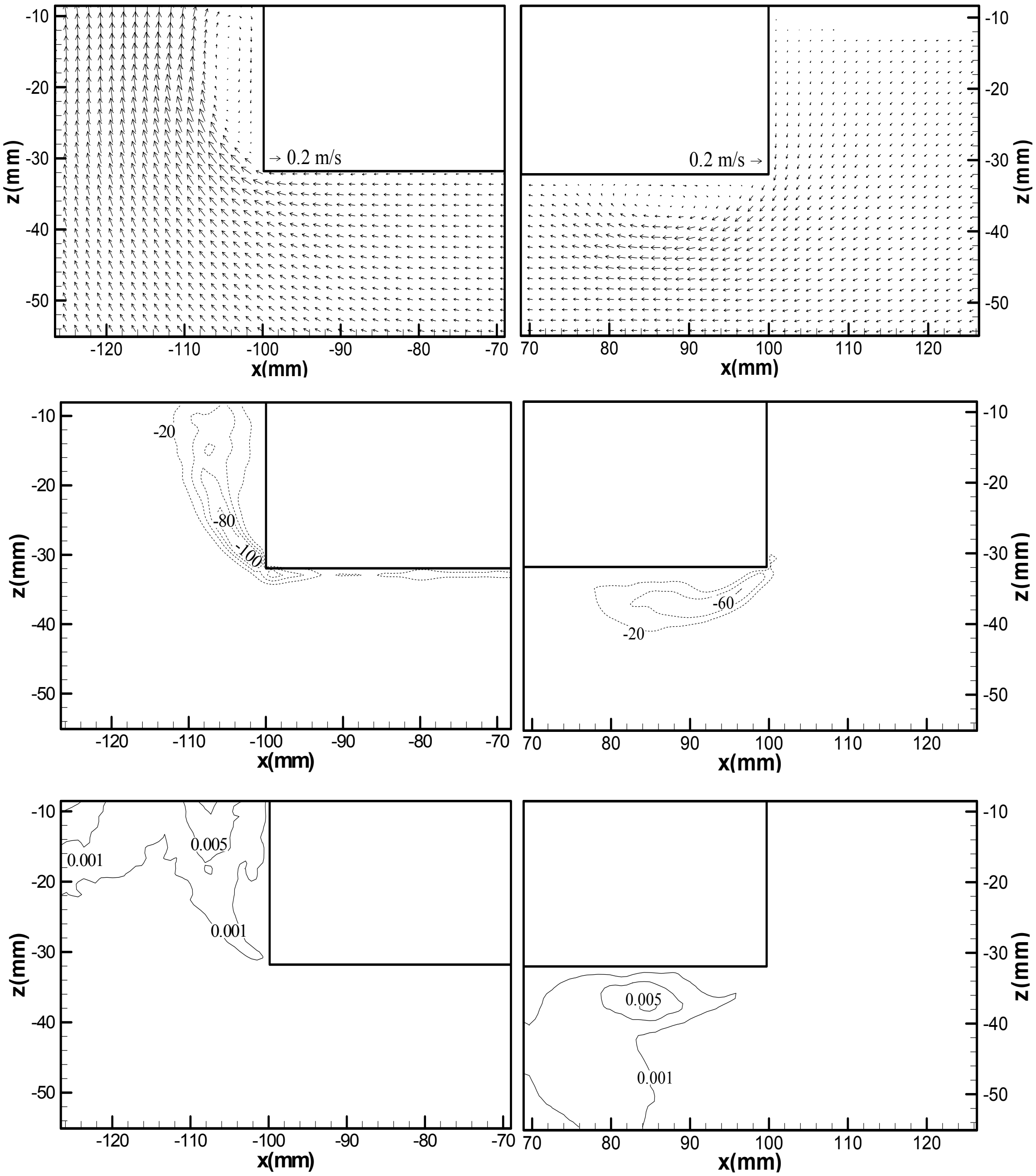

Seaward side Leeward side

(c)

Fig. 4.4 Continued

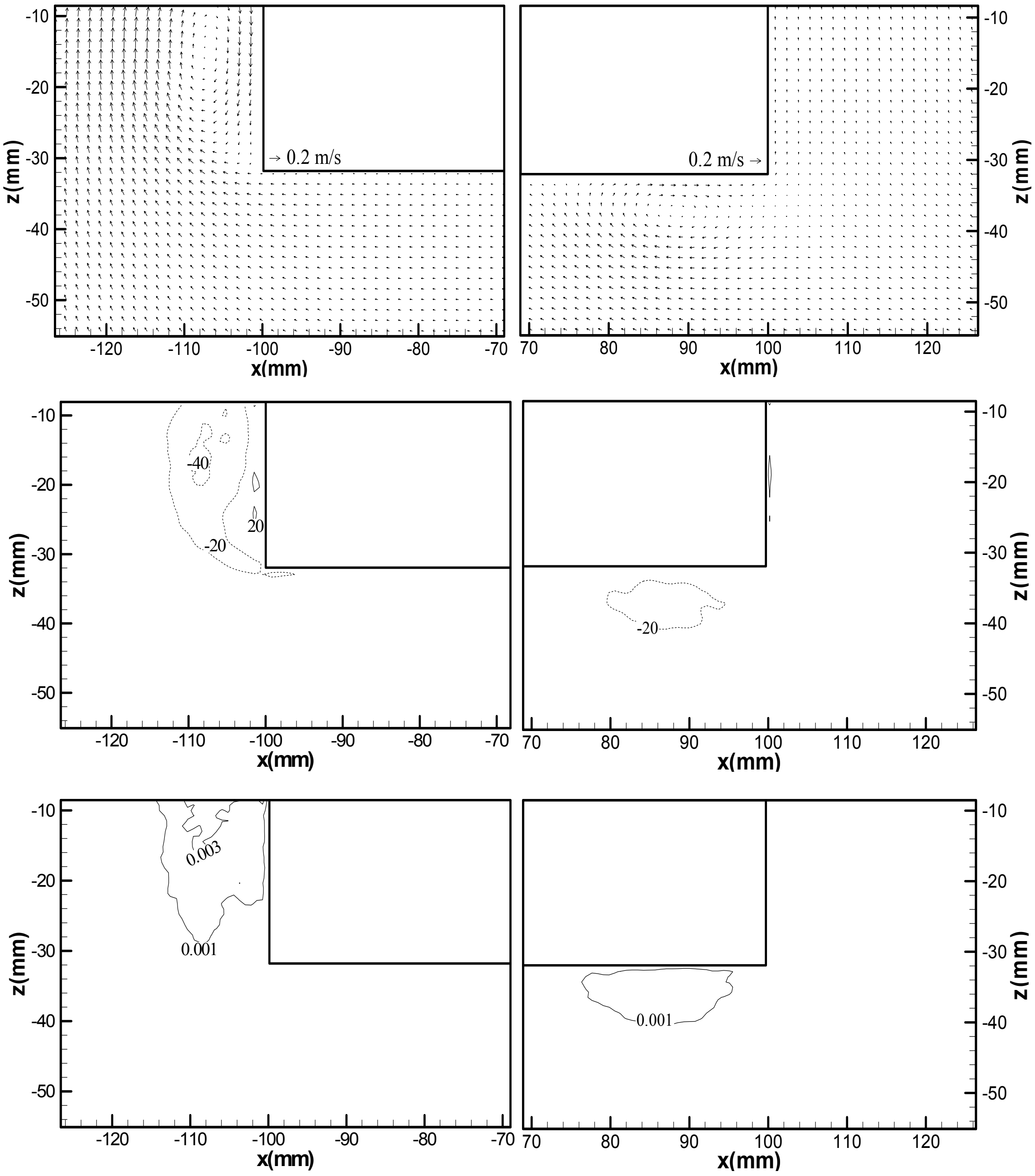

Seaward side

Leeward side

(d)

Fig. 4.4 Continued

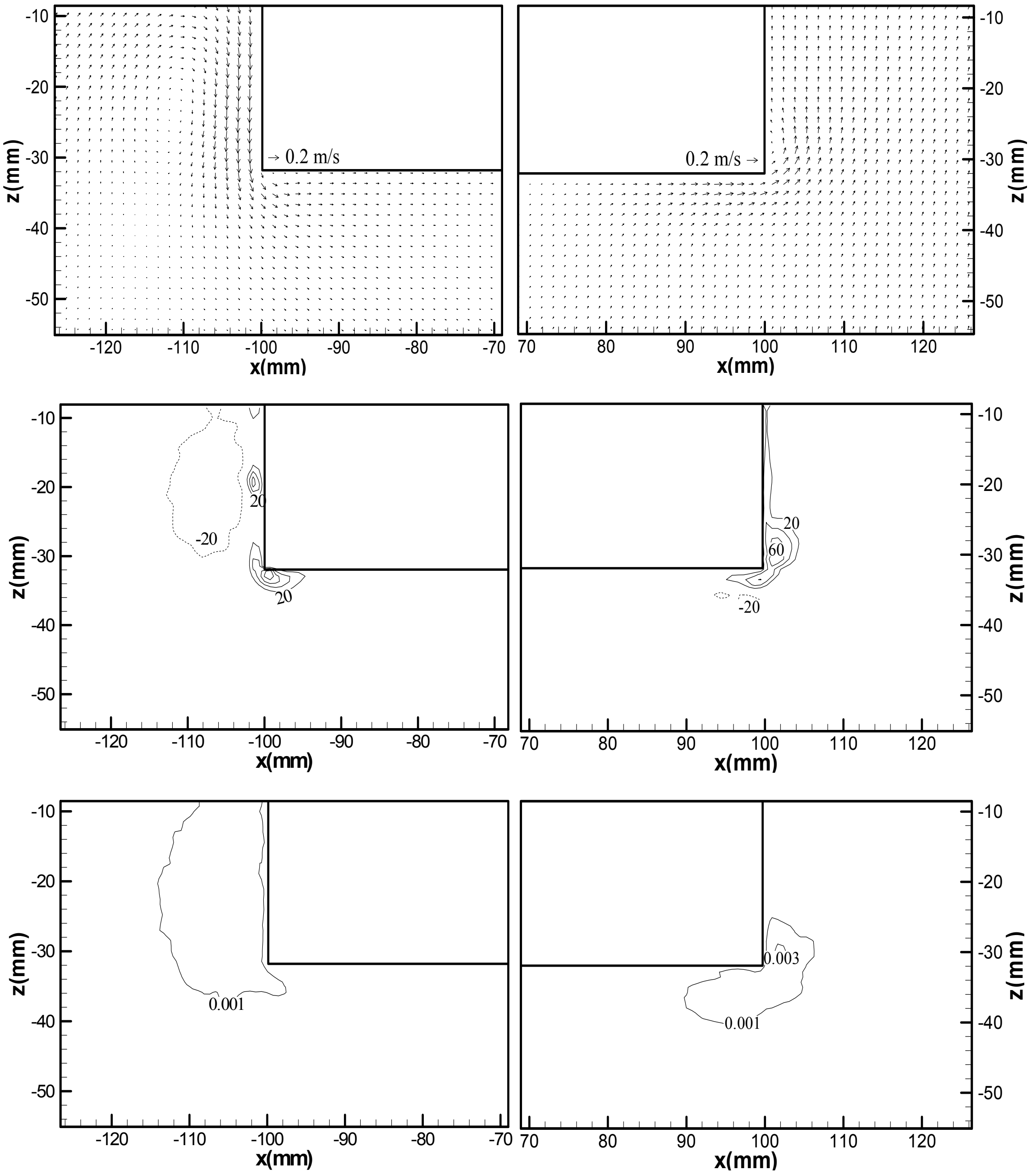

Seaward side Leeward side

(e)

Fig. 4.4 Continued

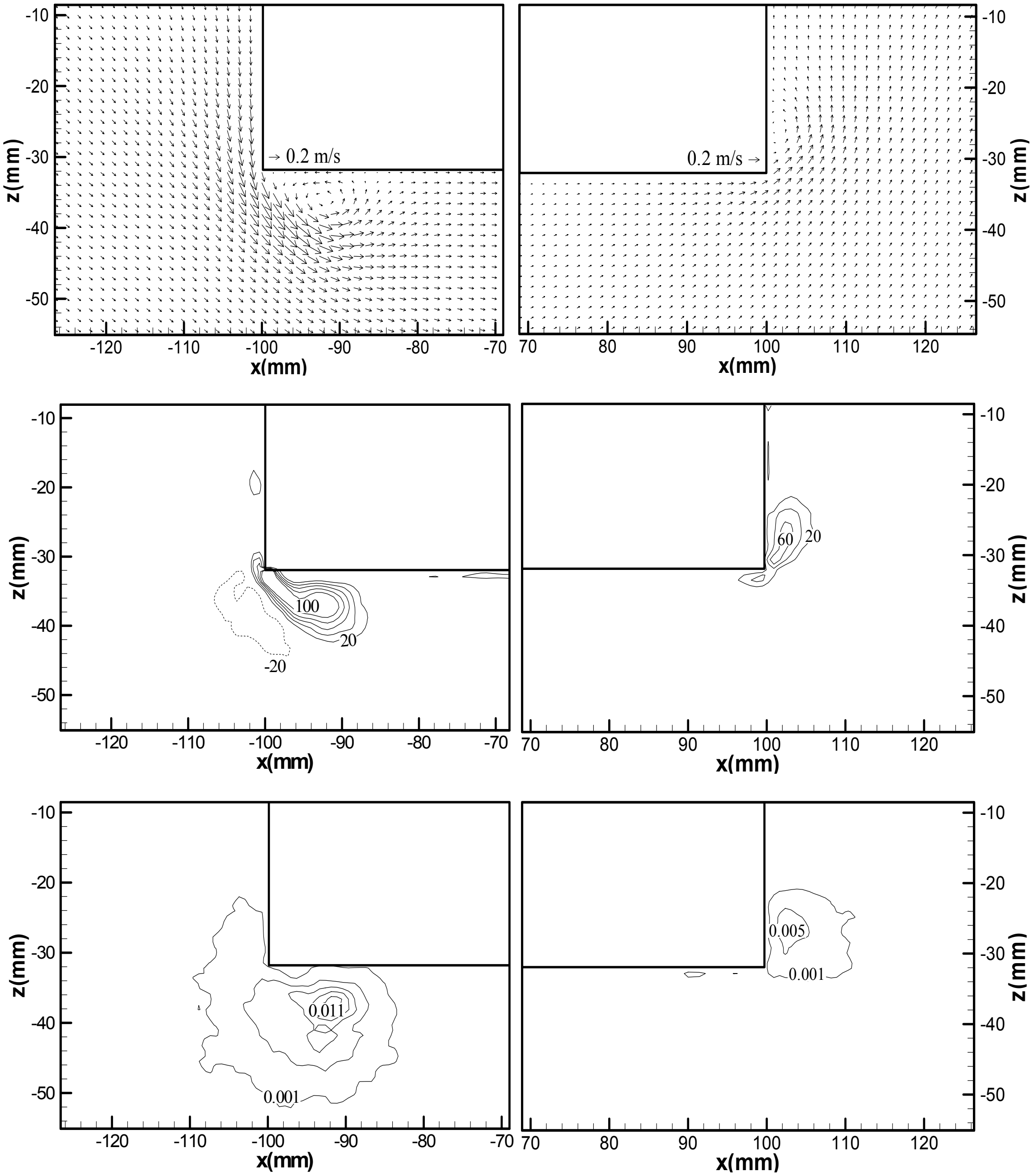

Seaward side Leeward side

(f)

Fig. 4.4 Continued

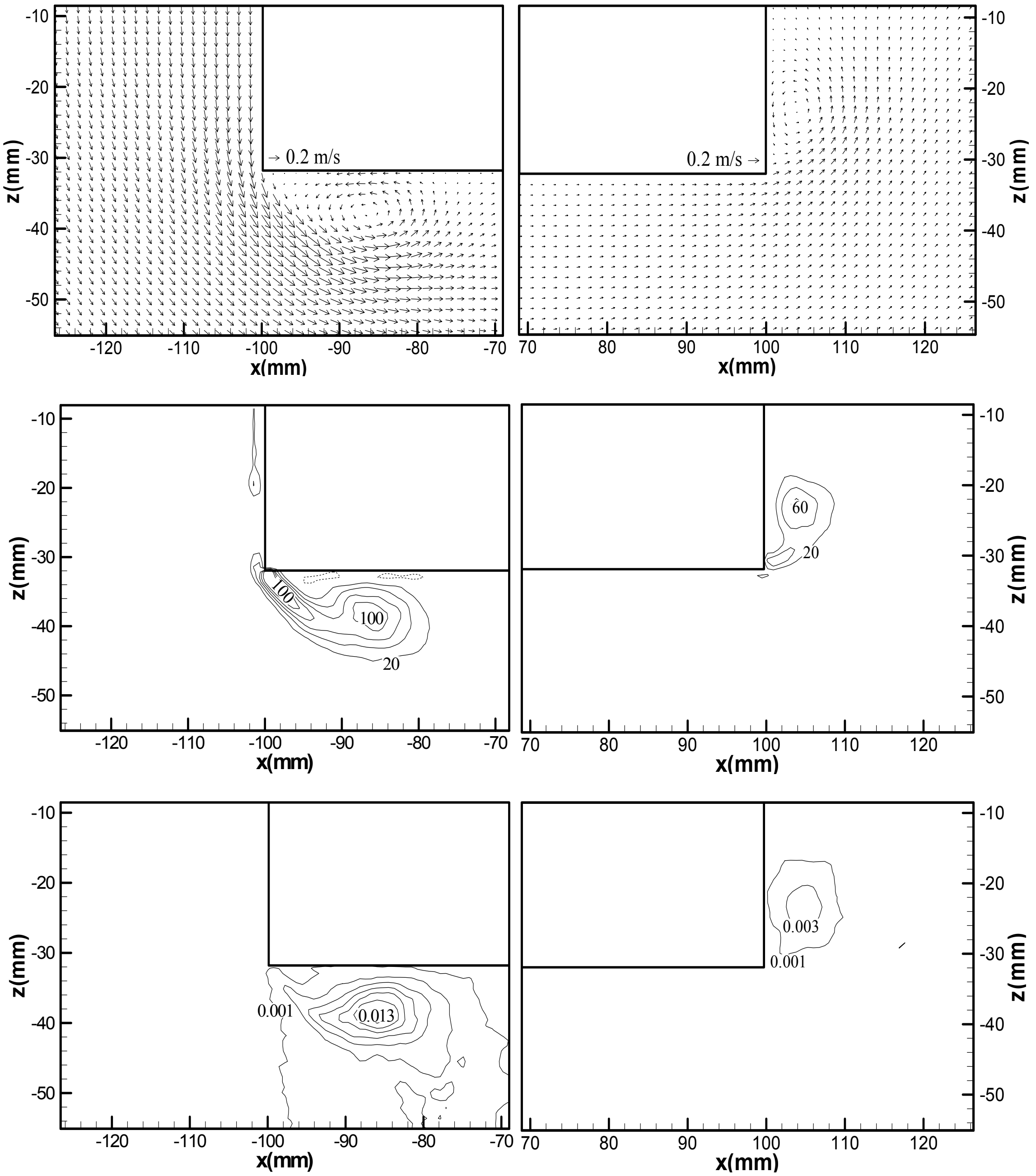

Seaward side

Leeward side

(g)

Fig. 4.4 Continued

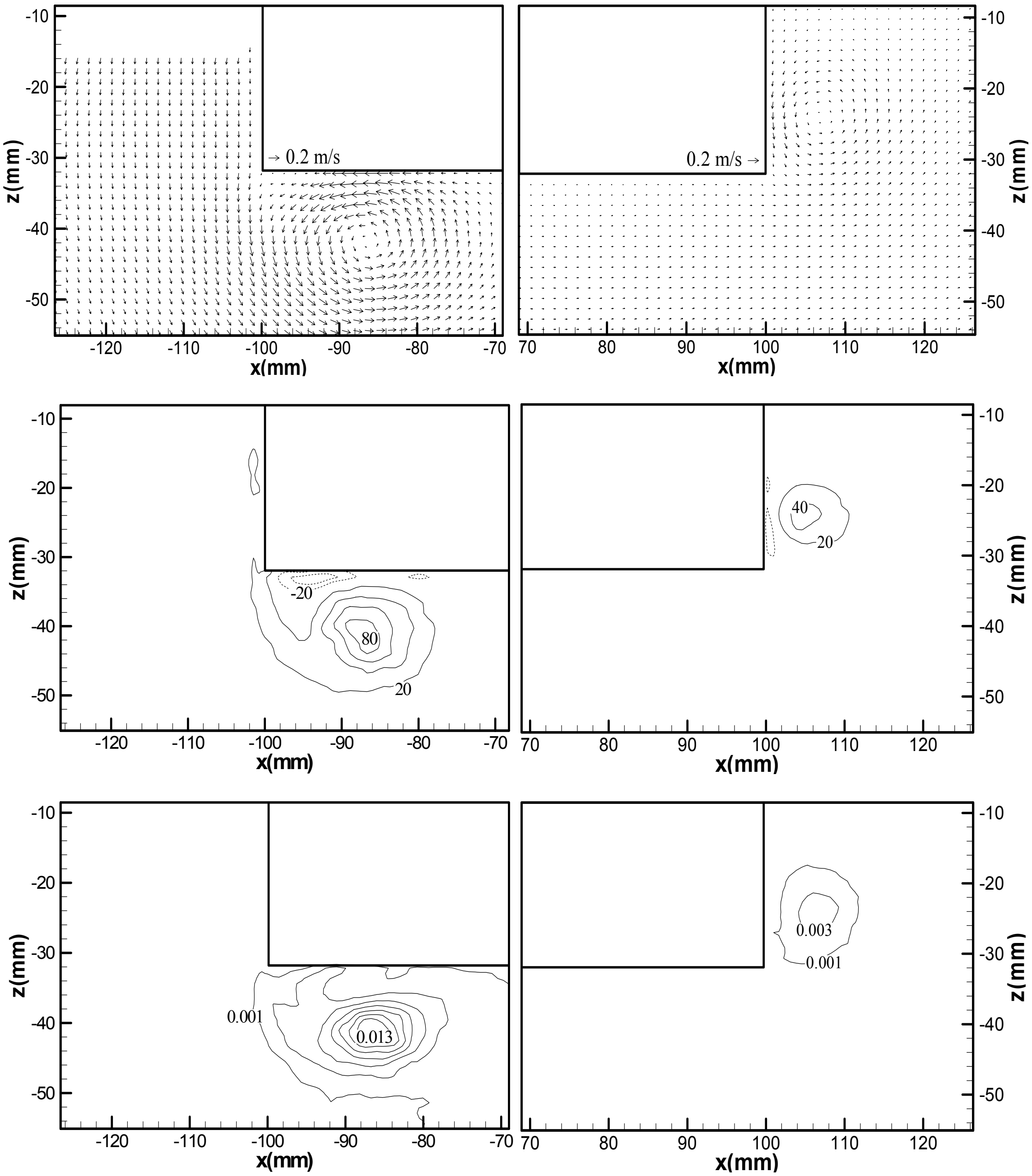

Seaward side Leeward side

(h)

Fig. 4.4 Continued

The negative vortices become larger and stronger while the positive vortices decay. The reattachment point moves upward (+*z*) at the seaward side and backward (-*x*) at the leeward side with a pattern similar to the flow passing a sudden contraction and expansion channel. The region with high turbulent kinetic energy coincides to that of the vortices. While the positive vorticity weakens and dissipates, the strength of turbulent kinetic energy seems to be sustained. This may be due to that the positive and negative vortices interacting with each other and canceling out their strength because of different signs. This renders that the magnitude of vorticity decays much faster than that of turbulent kinetic energy.

Further development of the negative vortices at phase c is shown in Fig. 4.4 (c). The negative vortex at the seaward side moves towards the free surface (seen from the larger FOV 1 but not shown here), while the negative vortex at the leeward side continues to be convected seaward by the mean flow. The diminishing positive vortex at the seaward side moves outside FOV 3 but still exists in FOV 1 (not shown here) and continues to move further to the left. This vortex with its corresponding turbulent kinetic energy migrates to the region beneath the free surface and gradually fades away until phase f. The movement of these vortices and turbulent kinetic energy can be seen in FOV 1 in Jung *et al.* (2002). In Fig. 4.4 (d) the negative vortices continue to reduce their strength as does the corresponding turbulent kinetic energy. In Fig. 4.4 (e), the positive vortices start to form at both corners when the wave crest is at the seaward side and the zero up crossing at the leeward side. The shedding of vortices and production of turbulent kinetic energy continues from Figs. 4.4 (e) to (g). In Fig. 4.4 (g), the positive vorticity and the corresponding turbulent kinetic energy grow to the maximum strength while the negative vorticity generated at the previous cycle disappears. The vortices almost completely shed out and separate from the corners. After this phase, the strength of both the vorticity and turbulent kinetic energy starts to diffuse and decrease, as seen in Fig. 4.4 (h). The flow is then about to change its direction again with the completion of one cycle and back to Fig. 4.4 (a). The level of turbulence intensity over the maximum mean velocity for the phases of strong turbulence and mean flows [Figs. 4.4 (b) and (h)] is about 0.5. This magnitude is very close to the value of 0.5 for the wake behind a circular cylinder (Townsend, 1956).

The uncertainties in PIV measurements can be expressed as the sum of the bias error and random error. Both the errors are a function of d_τ/d_{pix} with d_τ being the particle image diameter and d_{pix} the pixel spacing (Prasad, 1992). In this study, the measurement error is estimated to be about 0.1 pixel for the measurements taken in FOVs 3 and 4 ($d_\tau/d_{\text{pix}} = 1.5$). This corresponds to an uncertainty of about 3 mm/s in the velocity measurement and an error less than 2% of the local maximum velocity. In addition, the error in vorticity is estimated by $\Omega_e \approx u_e/\Delta z + w_e/\Delta x \approx 4\,\text{s}^{-1}$ with the subscript *e* being the error (Chang *et al.*, 2001). This result is comparable to the error estimation from applying the continuity equation, $|\partial u/\partial x + \partial w/\partial z| < 8\,\text{s}^{-1}$. Therefore, the error in vorticity calculation is less than 10% of the local maximum vorticity (Ω_{max}>80 s^{-1}).

4.3.3 Trajectory of key vortices

The trajectories of key vortices over one wave period, defined as the pair of main vortices generated at each phase from the structure corners due to flow separation, are shown in Fig. 4.5. The vortex motion is obtained from the flow fields of the two larger fields of view (FOVs 1 and 2). The location of each vortex is defined as the coordinates of the maximum absolute value of vorticity at a given moment. The positive vortex at the seaward side is transported from the structure corner to the free surface (above the stationary water level) and fades beneath the free surface. In addition, the negative vortex is transported from the structure corner to the region below the structure and dissipated there. While the positive vortex at the seaward side moves to the location above the stationary water level, the negative vortex at the leeward side does not due to its relatively short trajectory. Note that the trajectories of both the positive and negative vortices are not a close loop. The distance of the vortex trajectory at the seaward side is longer than that of the leeward side due to the differences in the water particle displacement.

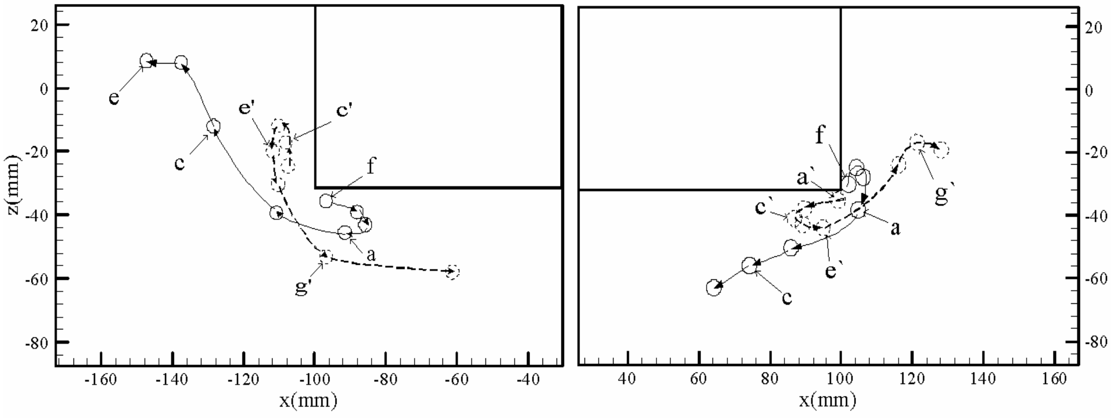

(a) Seaward side (b) Leeward side

Fig. 4.5 Trajectories of key vortices. Solid line and circle: maximum positive vorticity and its trajectory; dashed line and circle: maximum negative vorticity and its trajectory. The letters in the figure correspond to the phase in Fig. 4.2.

4.3.4 Rotational and turbulent region

To distinguish the rotational and turbulent flow region around the fixed structure, the absolute value of vorticity ($|\Omega|$) and turbulent kinetic energy (k_t) are averaged over one wave period and shown in Fig. 4.6. The figure shows that the vortical region and the turbulent region are strongly correlated to each other. For the seaward side, the vortical and turbulent region is confined within one wave particle trajectory of the incoming wave (20 mm calculated from linear wave theory) from the structure wall and near the structure corners. Because of the wave transmission/reflection effect due to the existence of the structure, the vortical and turbulent region on the leeward side is confined within only about 3/4 the wave particle trajectory of the incoming wave. Below the structure and away from the lower corners, the relatively weak vorticity is generated by the boundary layer. The result implies that the potential flow theory may be applicable to such a problem except in the region within one or two wave particle trajectories from the structure wall.

An obvious difference shown between Figs. 4.6 (a) and 4.6 (b) is that the turbulent kinetic energy seems to move farther away from the seaward structure corner and towards the free surface. This is due to the fact the vorticity dissipates faster due to the interaction of vortices of different signs while turbulence does not. This causes turbulence to take a longer time to dissipate and therefore moves farther by mean flow convection. Fig. 4.6 (b) also shows that the time averaged turbulent kinetic energy on the leeward side reduces to one order of magnitude smaller than that on the seaward side while the same phenomenon does not occur in vorticity. This is due to the fact that the vorticity generation is influenced primarily by the wave (and thus the velocity) transmission while turbulence kinetic energy is influenced by the square of the wave transmission that comes with a much smaller value.

The spatial-averaged vorticity and turbulent kinetic energy in the rotational region are shown in Fig. 4.7. At the seaward side, the magnitude of the positive vorticity is stronger than that of the negative vorticity. This is not observed at the leeward side. It could be due to the smaller size of vortices and thus lack of resolution in the measurement that tends to smooth out the vorticity. The magnitude of vorticity at the leeward side is smaller than that at the seaward side but remains the same order and magnitude, and similar to the value of the wave transmission coefficient. However, the magnitude of turbulent kinetic energy at the leeward side is significantly smaller than that at the seaward side due to the small energy transmission that is approximately the square of the wave transmission coefficient. Although the flow at the seaward and leeward sides has a phase lag of T/8 due to the width of the structure, the patterns of both vorticity and turbulence at both sides vary coincidently with time. The variation of turbulent kinetic energy seems to follow the summation of absolute vorticity of both signs. The two picks of turbulent kinetic energy coincide with each peak of vorticity of different signs.

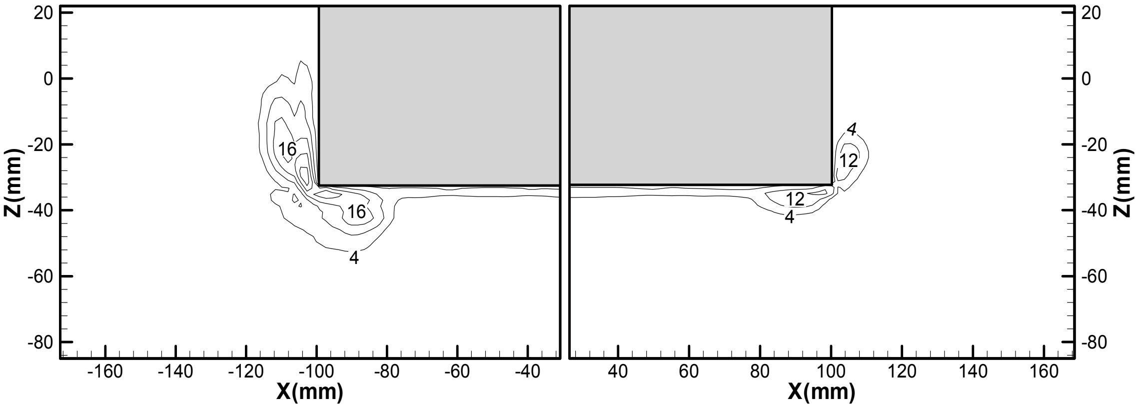

Seaward side Leeward side

(a)

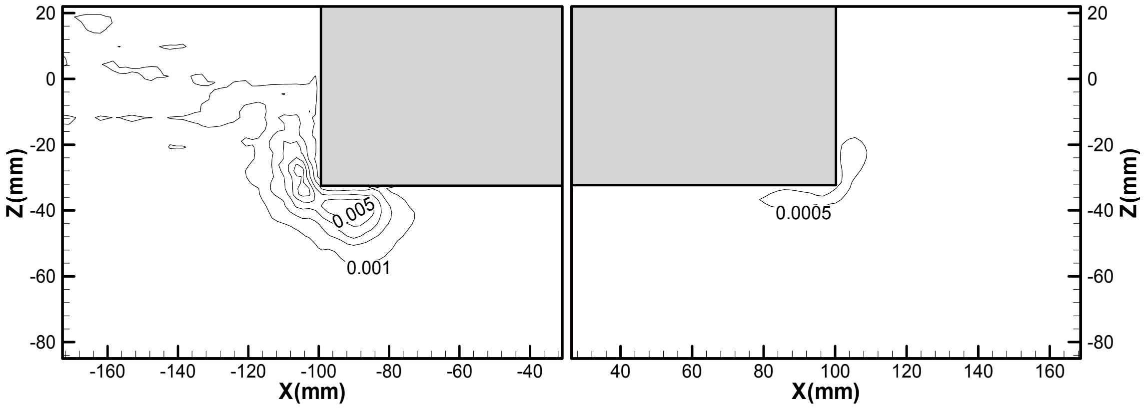

Seaward side Leeward side

(b)

Fig. 4.6 Time-averaged vorticity with an increment of $\Delta\Omega = 4$ s^{-1} between contour lines and time-averaged turbulent kinetic energy with an increment of $\Delta k_t = 0.001$s^{-1} between contour lines for the seaward side, and 0.0005 s^{-1} for the leeward side.

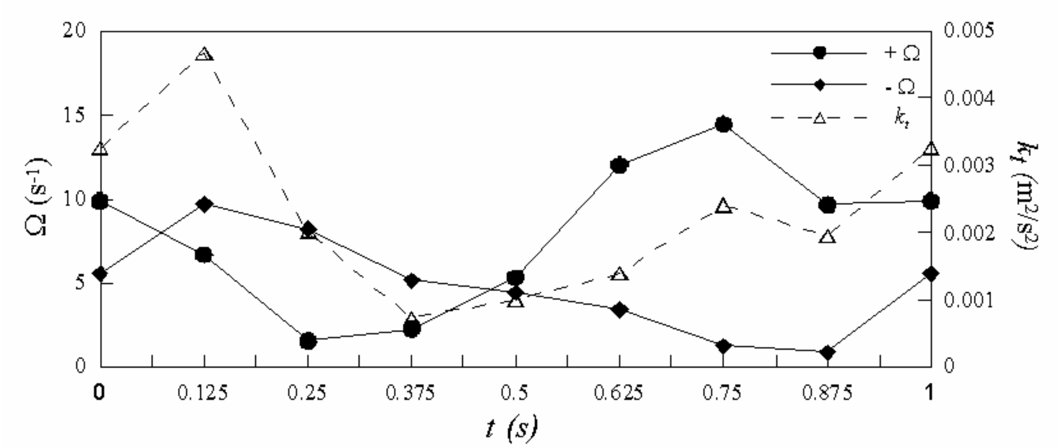

(a) Seaward side

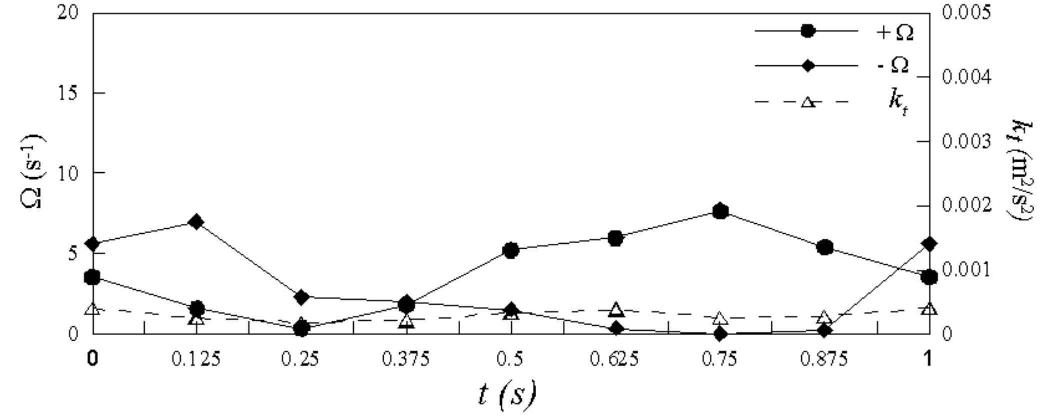

(b) Leeward side

Fig. 4.7 Spatial-averaged vorticity and turbulent kinetic energy.

4.3.5 Turbulent energy budget

The turbulent kinetic energy budget at both sides of the structure is present in Fig. 4.8. Each term in the equation of turbulent kinetic energy budget [see equation (3.6)] was averaged over the turbulent region which was confined within the wave particle trajectory from the structure corners as shown in Fig. 4.6. Note that the vertical scale for the seaward side in Fig. 4.8 (a) is twice that for the leeward side in Fig. 4.8 (b). As expected, more turbulent kinetic energy is produced and dissipated at the seaward side than at the leeward side. From the figure, most of the turbulent kinetic energy in the turbulent region is gained by turbulent production and then lost mainly by turbulent transport and advection moving the energy out of the region. The turbulent energy is then dissipated outside the region. The pattern of turbulent production is nearly identical to the spatial-averaged turbulent kinetic energy shown in Fig. 4.8. Note that turbulent dissipation was estimated using equation (3.10) with the assumption of isotropic dissipation.

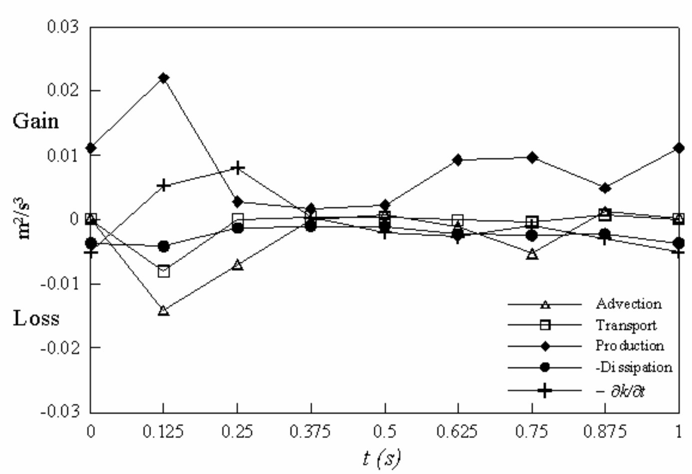

(a) Seaward side

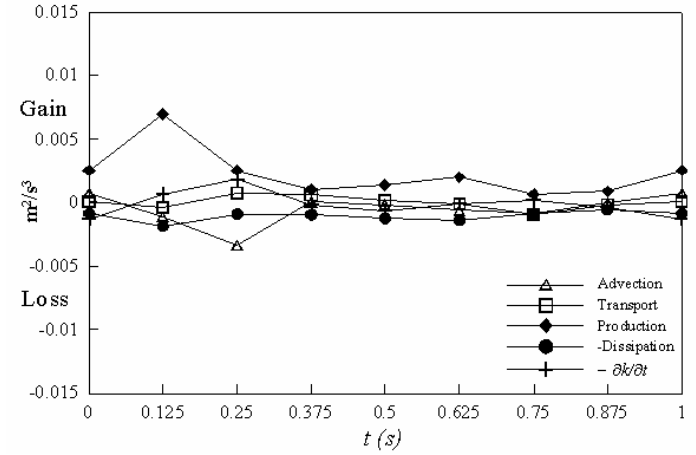

(b) Leeward side

Fig. 4.8 Turbulent kinetic energy budget.

The Taylor microscale, λ_T, is frequently used to estimate turbulent dissipation. The microscale was computed, following its definition, from the longitudinal velocity correlation function using the measured velocity shown in Fig. 4.9. In this study it was found that $\lambda_T \approx 5.8$ mm while the largest turbulent eddy size is approximately 15.2 mm. In addition, the Kolmogorov length scale was estimated as $\eta_K \approx 0.13$ mm using the measured data at the seaward side along $z = -42$ mm under the structure bottom at phase h (see Fig. 4.2 and Fig. 4.3). The PIV spatial resolution, defined as the size of the interrogation window, for the two smaller FOVs (FOVs 3 and 4) is about 10 times the Kolmogorov length scale but only one-quarter of the Taylor microscale.

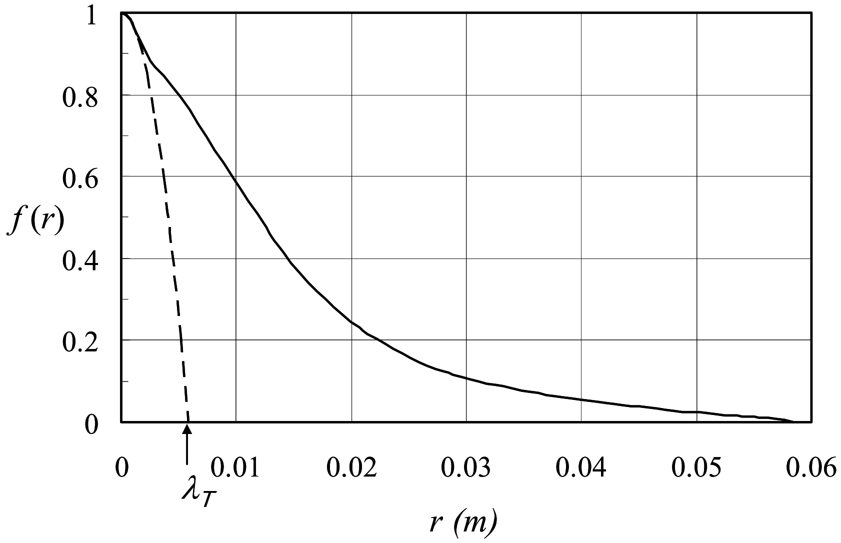

Fig. 4.9 Longitudinal velocity correlation function and microscale (λ_T).

In order to measure the total turbulent dissipation rate, the spatial resolution is required to be of the size of the Kolmogorov length scale. However, with a spatial resolution of $10\eta_K$ approximately 80% of the total dissipation rate can still be obtained, estimated by using the dissipation spectrum (Pope, 2000). Since the velocity in the y-direction is not measured, the turbulent dissipation was computed by applying equation (3.10) directly to the measured velocity. Browne *et al.* (1987) reported that using the assumption of isotropic turbulence in the cylinder wake region underestimates the dissipation by almost 45% at the centerline where the flow is fully turbulent. Therefore, assuming isotropic dissipation in this study may underestimate the dissipation by one-half. However, it will provide the correct order of magnitude, if not the exact magnitude, for the calculated value.

Although the viscous diffusion and the turbulent pressure transport terms are not included in the turbulent kinetic budget in equation (3.6), turbulent dissipation can still be calculated by applying the equation since those two terms are expected to be relatively small. The calculated turbulent dissipation by the assumption of isotropic dissipation is comparable to that calculated from the balance of budget of the other terms in equation (3.6). The comparison is shown in Fig. 4.10. The agreement is reasonably well, meaning that the estimation of turbulent dissipation may be accurate, at least to the order of magnitude.

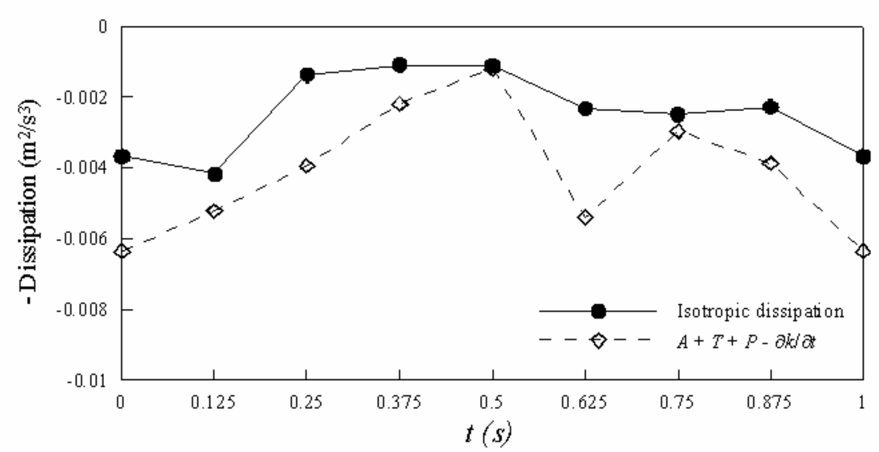

(a) Seaward side

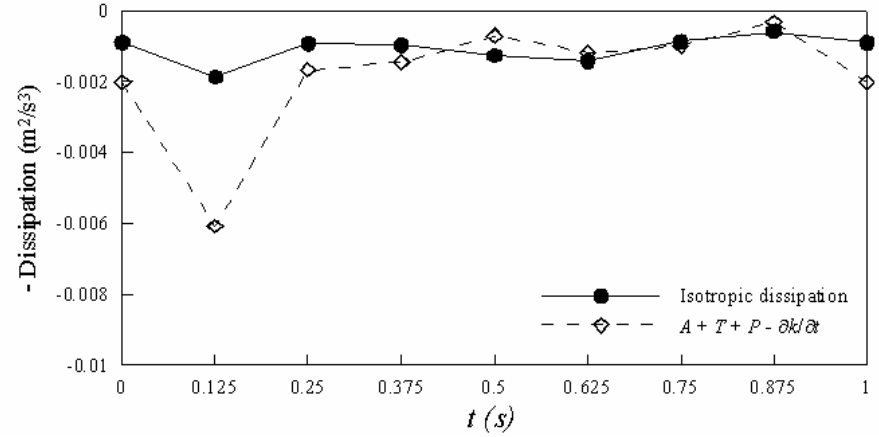

(b) Leeward side

Fig. 4.10 Comparison of turbulent dissipation estimated using different methods.

4.4 Concluding remarks

Flow characteristics, including velocity, vorticity, and turbulence, of wave interaction with a fixed rectangular structure, similar to a barge in a beam sea condition, are investigated experimentally using Particle Image Velocimetry (PIV). The generation and evolution of vortices due to the periodical wave motion are demonstrated from the phase-averaged mean velocity using 90 measured instantaneous velocities at the same phase. The positive and negative vortices are generated due to corner separation and migrated with each distinct open trajectory. The dissimilarity nature between the seaward side and leeward side of the structure is illustrated by the mean and turbulent flow characteristics. The vorticity and turbulent kinetic energy are stronger at the seaward side than those at the leeward side.

The rotational and turbulent region in the flow is distinguished by the time-averaged vorticity and turbulent kinetic energy. It is found that the region is confined within one wave particle trajectory of the incoming waves from the structure wall near the corners. This indicates that the potential flow theory could be applicable except in this region. The pattern of the turbulent kinetic energy is highly correlated with that of vorticity, and the peaks of the turbulent kinetic energy are consistent with the loci of the vortices. Each term in the turbulent kinetic energy budget is measured, except the pressure transport term and the viscous dissipation term (being neglected). Turbulent dissipation is estimated using both the isotropic dissipation assumption and from the balance of the turbulent kinetic energy budget with comparable results between them.

CHAPTER V

WAVE INTERACTIONS WITH ROLLING RECTANGULAR BARGE

5.1 Experimental set-up and condition

A rectangular wooden structure with the dimensions of 0.900 m long (*L*), 0.200 m wide (*B*), and 0.064 m high (T_B) was used in the experiment as shown in Fig. 5.1. The structure was located at 20 m from the wavemaker with its long axis extending across the entire width of the tank. The structure was mounted using a steel rod through the center of gravity across the tank on a pair of hinges on the tank walls. These hinge supports allow the structure to roll but restrain it from heave and sway. The hinges were adjusted so the axis aligns with the calm water level. Consequently, the structure floated at a draft that equals one half of its height.

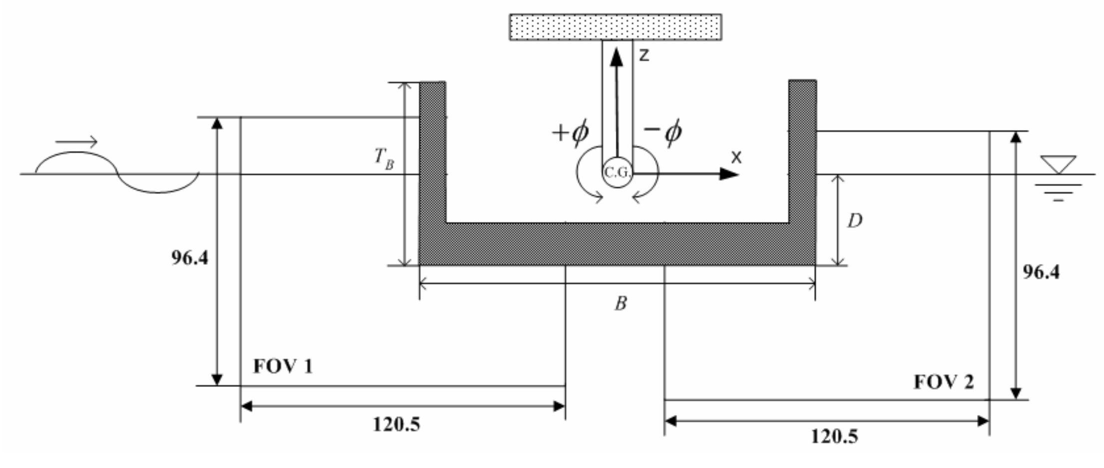

Fig. 5.1 Sketch of the rectangular structure and the PIV fields of view (unit: mm).

Water depth was maintained at 0.800 m throughout the experiment. Two regular wave trains with periods of T = 1.0 s and 2.0 s were generated with a wave height (*H*) of

0.040 m. The corresponding wavelengths (λ) are 1.56 m and 4.85 m. Measurements were taken after the incident waves reached the quasi-steady state, roughly 15 minutes after the wavemaker was started. The Reynolds number, defined as Re = $U_{max}B/(2\nu)$, is 2.8×10^4 for the 1.0 s waves and 2.5×10^4 for the 2.0 s waves with U_{max} being the maximum water particle velocity and ν the kinematic viscosity. The roll natural frequency of the structure is $w_N = 10.13$ rad/s ($T_N = 0.62$ s), obtained using the free decay test performed in the calm water condition. Regular waves with $H = 0.02$ m and a wave period the same as the roll natural period of the structure were also used to demonstrate the typical eddy making damping that reduces the roll motion. The measurements for the natural period waves were conducted before the reflected waves coming back to the structure so problems caused by wave reflection were eliminated.

5.2 Data acquisition

The CCD camera was operated at 4 Hz for the cases of $T = 1.0$ s and $T = 2.0$ s. The measurements were taken at about 30 minutes after the wave generator was started to ensure that the quasi-steady condition had been reached. This allows the mean flow and turbulence to be extracted using the phase-average method. For the PIV velocity measurements, the time interval between the consecutive phases was set as 0.125 s, resulting in 8 phases per period for the case of $T = 1.0$ s, and 16 phases per period for $T = 2.0$ s. Ninety pairs of images were taken at each phase for obtaining turbulent statistics. The double-frame/single-pulsed cross-correlation method was used for PIV velocity computation. Two fields of view (FOV) covering the two lower corners of the structure were used for the PIV velocity measurements, as shown in Fig. 5.1. The sizes of the FOVs were fixed as 120.5×96.4 mm^2. FOV 1 and FOV 2 were intended to cover the region in which vortices and turbulence were generated due to the interactions between the waves and the structure. Interrogation windows of 32×32 pixels (a physical dimension of 3.0×3.0 mm^2) with a 50% overlap between the adjacent windows were used in the PIV velocity determination, i.e., the distance between the adjacent vectors is

1.5 mm. The time separation (*dt*) between two laser pulses in an image pair was set at 3.0 ms.

The uncertainties in PIV measurements can be expressed as the sum of the bias error and the random error. These errors are a function of d_τ/d_{pix} with d_τ being the particle image diameter and d_{pix} the pixel size (Prasad *et al.*, 1992). In this study, the measurement error is estimated to be about 0.1 pixel for d_τ/d_{pix} being equal to 0.97. This corresponds to an uncertainty of about 3.5 mm/s in the velocity measurements and an error less than 2% of the local maximum velocity. In addition, the error in vorticity is estimated as $\Omega_e \approx u_e/\Delta z + w_e/\Delta x \approx 5\,\text{s}^{-1}$ with the subscript *e* indicating error (Chang *et al.*, 2001). The result is comparable to the error estimation applying the continuity equation by computing $\left|\partial U/\partial x + \partial W/\partial z\right|$. The estimated error in vorticity is about 10 s^{-1}, which is less than 20% of the local maximum vorticity.

Two double-wired resistant-type wave gauges were used to measure the free surface elevation at a sampling rate of 100 Hz. The gages were located at 4 cm in front and 4 cm behind the rectangular structure, respectively, to measure the wave elevation at the PIV fields of view. Fig. 5.2 shows the free surface elevation taken by the wave gages and the corresponding phases in the later PIV velocity maps. The transmission coefficient, K_T, defined as the ratio of the transmitted wave height (H_T) to the incident wave height (H), was found to be 0.75 for the T = 1.0 s waves (B/λ = 0.125) and 0.91 for the T = 2.0 s waves (B/λ = 0.062). The inclined angle, ϕ, of the rectangular structure was measured using the PIV images and plotted in Fig. 5.3. The sign of ϕ was defined as positive for the counterclockwise rotation (roll-away) and negative for the clockwise rotation (roll-in).

The measurements were taken at about 30 minutes after the wave generator was started to ensure that the quasi-steady condition had been reached. This allows the mean flow and turbulence to be extracted using the phase-average method. For the PIV velocity measurements, the time interval between the consecutive phases was set as 0.125 s, resulting in 8 phases per period for the case of T = 1.0 s and 16 phases per period for T = 2.0 s.

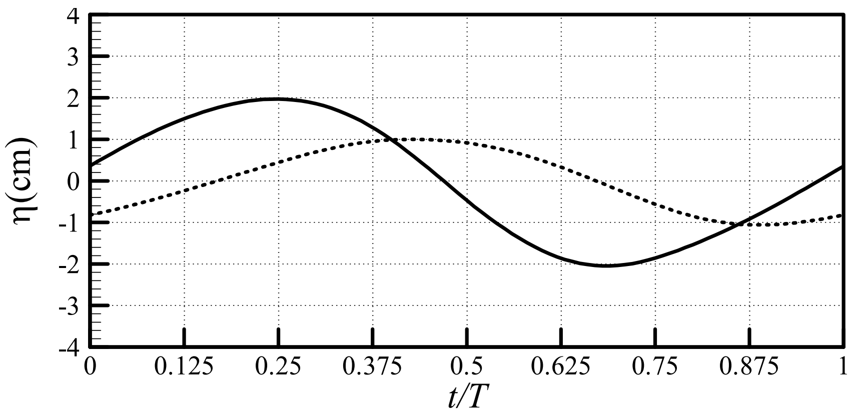

(a) $T = 1.0$ s

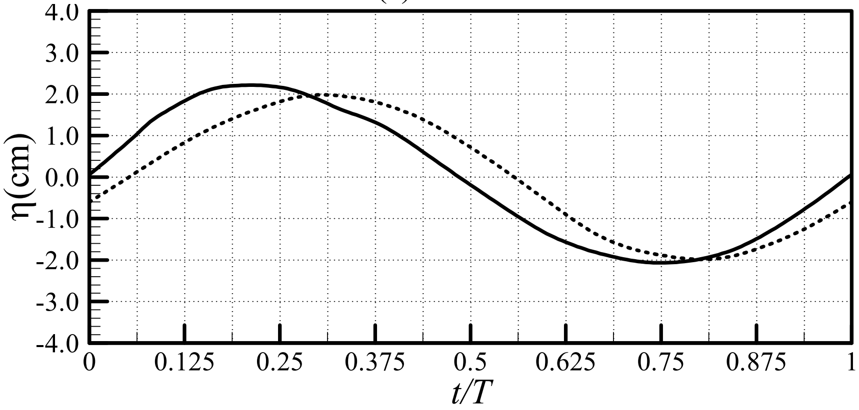

(b) $T = 2.0$ s

Fig. 5.2 Wave profiles at a distance of 4 cm from each side of the rectangular structure. Solid line: seaward side; dashed line: leeward side.

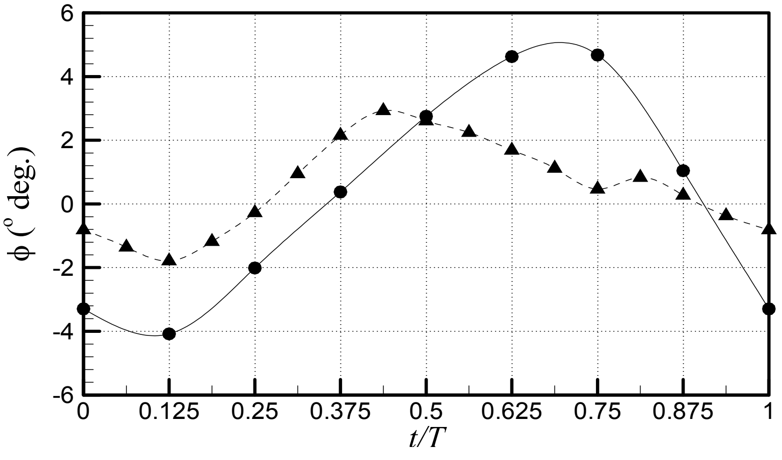

Fig. 5.3 Roll motion for the $T = 1.0$ s, solid line, and $T = 2.0$ s, dotted line.

5.3 Experimental results

Mean velocity, mean vorticity and turbulence property at 8 different phases for the case of $T = 1.0$ s and at 16 phases for $T = 2.0$ s were measured using PIV. Note that only every other velocity vector in each row and column was plotted, i.e., only one-quarter of the total measured velocity vector are displayed in the velocity plots shown in this section. The phases of the velocity maps correspond to those in Fig. 5.2 and Fig. 5.3 for free surface elevation and inclined angle, respectively.

5.3.1 Mean flow pattern

The mean velocity fields over one wave period at the seaward side of the structure for the $T = 1.0$ s case are displayed in Fig. 5.4. In Fig. 5.4 (a) and (b), the structure rolled away (i.e., inclined in the negative or clockwise direction). A negative vortex separated at the corner while the free surface and the fluid moved upwards. In Fig. 5.4 (c), the structure was about to pass the wave crest and ready to turn to roll in (i.e., inclined in the positive or counterclockwise direction) while the strength of the negative vortex decreased.

From Fig. 5.4 (d), the flow started to reverse its direction and a positive vortex was initiated at the corner. This positive vortex separated at the structure corner and moved underneath the structure. The structure reached and then passed its maximum roll angle at the wave trough between Figs. 5.4 (e) and 5.4 (g). The positive vortex became fully developed in Fig. 5.4 (f) while the water level started to rise. The flow again reversed its direction in Fig. 5.4 (g) and created a jet-like upward flow pattern in Figs. 5.4 (h) and 5.4 (a). The positive vortex disappeared and the negative vortex was created.

From the flow pattern in Fig. 5.4 for the $T = 1.0$ s case for wave interactions with the free-rolling rectangular structure, we found that the generation of vortices is dominated by the fluid motion instead of the structure motion for waves with a period longer than the roll natural period of the structure (0.62 s in the present study). In other words, the velocity of the fluid motion is relatively faster than that of the structure if the wave period is longer than the roll natural period. This causes the generated vortices to be at the same side of the roll motion. This indicates that the vortices generated at the corners of the rolling structure tend to amplify the structure motion. No eddy damping effect was found for such condition.

The flow pattern is, interestingly, somewhat similar to that of the fixed structure in Jung *et al.* (2004) if we fix our coordinates following the rolling structure. Obviously, the strength of the vortices in the rolling case is weaker than that of the fixed case because the rolling structure moved in the same direction as that of the fluid.

It is well known that certain vortex patterns cause the so-called eddy-making damping and reduce the structure roll motion. Fig. 5.5 shows the typical flow pattern measured using PIV for the eddy making damping with the wave period being the same as the roll natural period of the structure, i.e., $T = 0.62$ s. Note that the velocity maps shown in the figure are instantaneous results, not phase averaged. The structure was rolling clockwise in the left panel of Fig. 5.5 and rolling counterclockwise in the right panel. The vortices were generated following the structure motion and located behind the structure. From the flow pattern, it is clear that the vortices cause the form drag and reduce the structure roll motion, which is the typical eddy making damping effect. In practice, vortices created by the interactions between waves and a ship or a barge-like structure in a beam sea condition reduce the structure roll motion due to the eddy making damping if the wave period is near the roll natural period of the structure. The evidence is clearly shown in Fig. 5.5. However, for waves with a period longer than the roll natural period, the generated vortices do not help to reduce the structure roll.

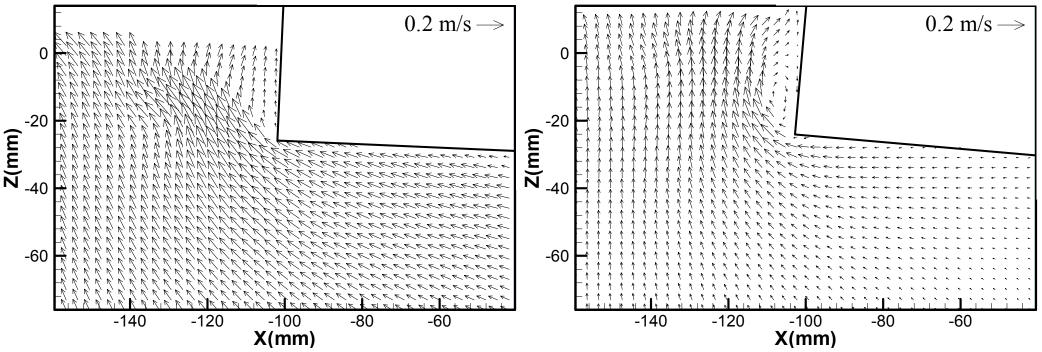

(a) *t/T* 0.000 (b) *t/T* = 0.125

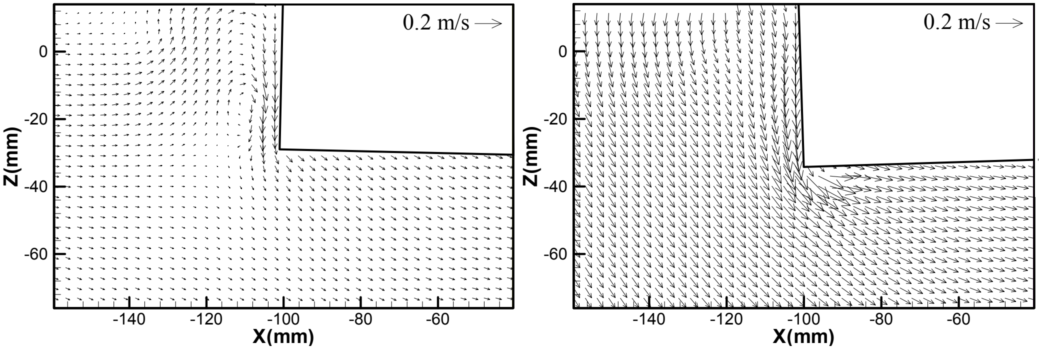

(c) *t/T* = 0.250 - (d) *t/T* = 0.375

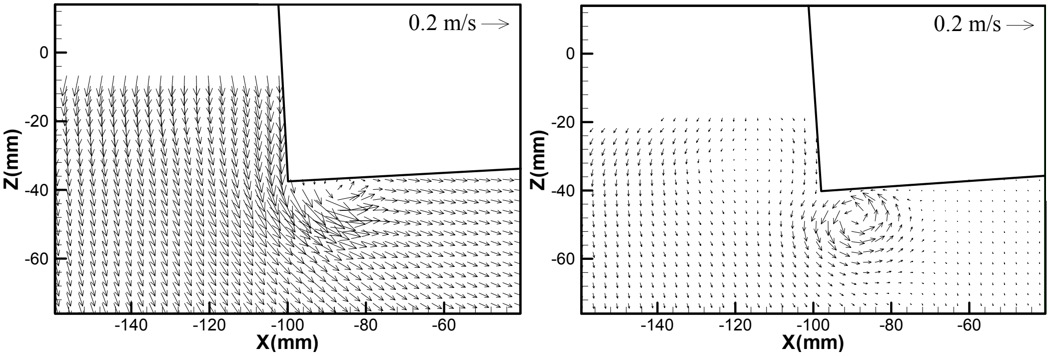

(e) *t/T* = 0.500 (f) *t/T* = 0.625

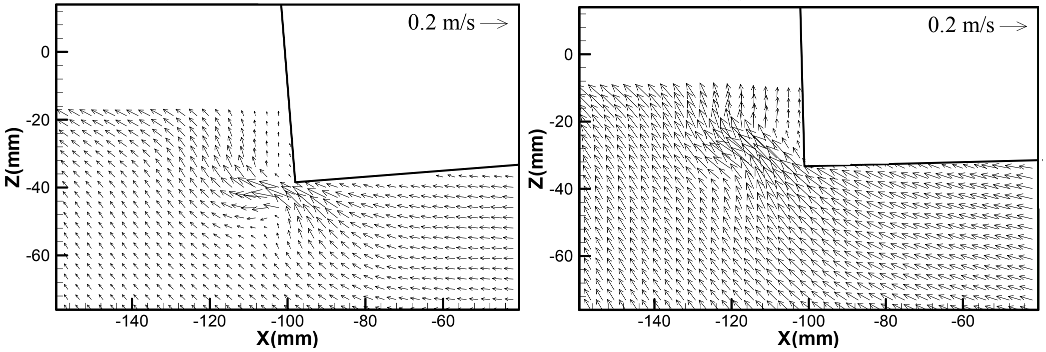

(g) *t/T* = 0.750 (h) *t/T* = 0.850

Fig. 5.4 Seaward side mean velocity over one wave period for the case of *T* = 1.0 s.

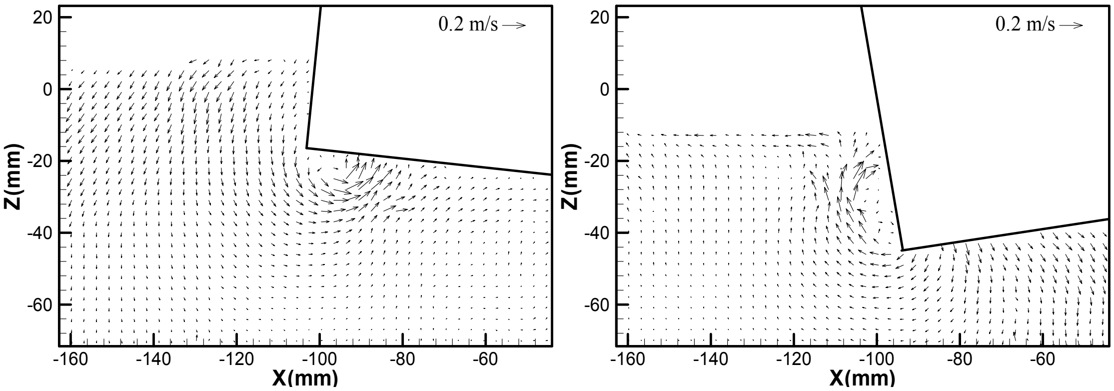

(a) ϕ = -8.5° (b) ϕ = 8.8°

Fig. 5.5 Instantaneous velocity maps of the typical eddy making damping. The wave period is equal to the roll natural period (T = 0.62 s). The structure was rolling clockwise in the left panel and rolling counterclockwise in the right panel.

5.3.2 Vorticity and turbulence characteristics

Fig. 5.6 and Fig. 5.7 show the mean velocity, mean vorticity, and turbulent kinetic energy at the instants of the most developed clockwise and counterclockwise vortices in the cases of T = 1.0 s and T = 2.0 s, respectively. The development of turbulent kinetic energy was consistent and highly correlated in terms of phase and location with vorticity in roll motion. This is similar to what was previously found using a fixed structure (Jung *et al.* 2004). In Fig. 5.6 (a), the negative vorticity at the seaward side was the most developed, occurred at the maximum negative roll motion t/T = 0.125 (see Fig. 5.3), and the positive vorticity was almost faded away. While the counterclockwise vortices quickly weakened, the strength of turbulent kinetic energy was sustained relatively longer [see the area close to (x, z) = (-140, 0) mm]. This is due to the fact that the positive and negative vortices interacted with each other and cancelled out their strength. This renders the magnitude of vorticity to decay much faster than that of turbulent kinetic energy.

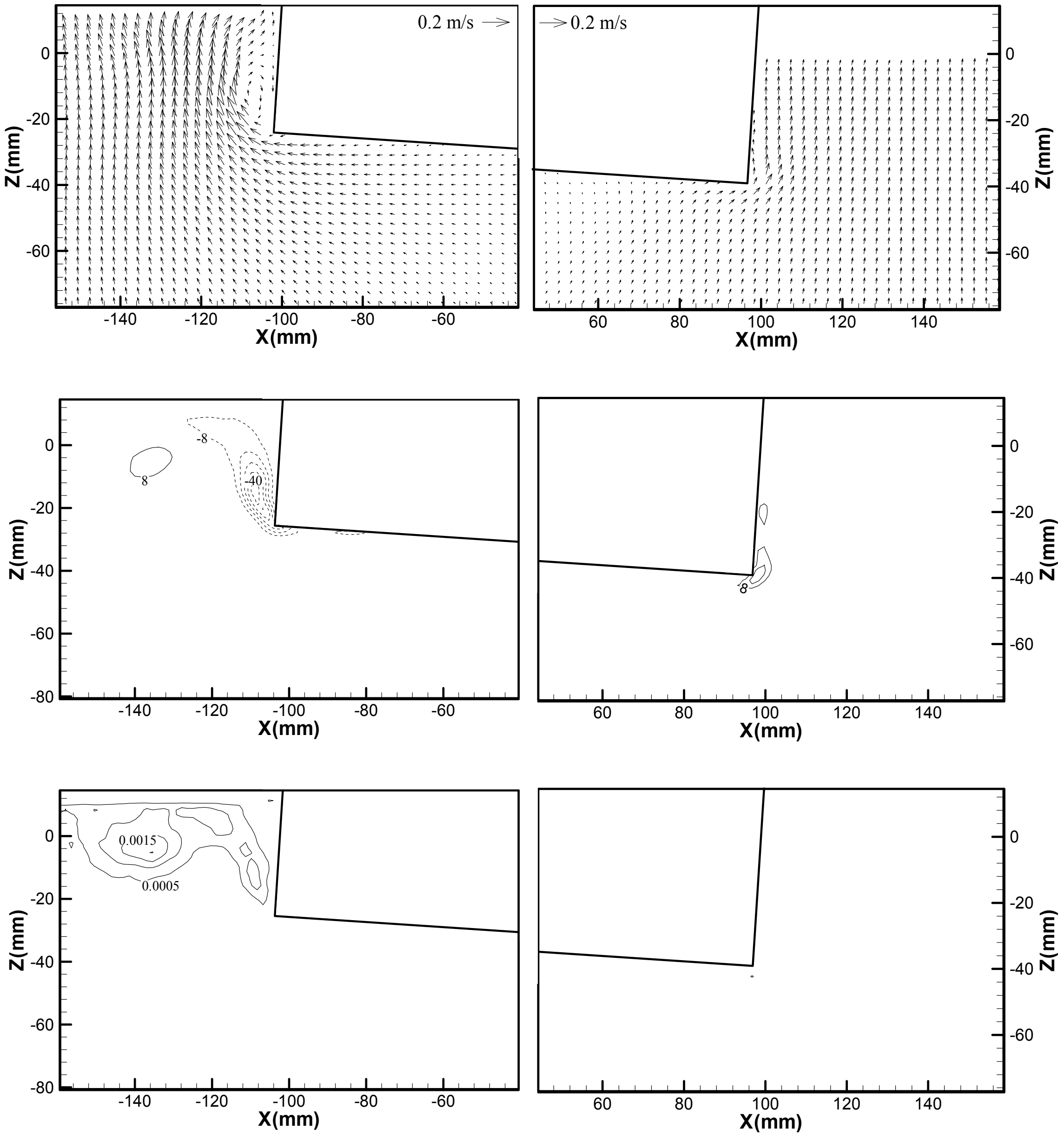

(a)

Fig. 5.6 Mean velocity (the first row), mean vorticity (the second row), and turbulent kinetic energy (the third row) for the case of T = 1.0 s. The increment of contours in vorticity is $\Delta\Omega = 8\ \mathrm{s}^{-1}$ while the increment of contours in turbulent kinetic energy is $\Delta k_t = 0.0005\ \mathrm{m}^2/\mathrm{s}^2$. (a) $t/T = 0.125$ and (b) $t/T = 0.625$.

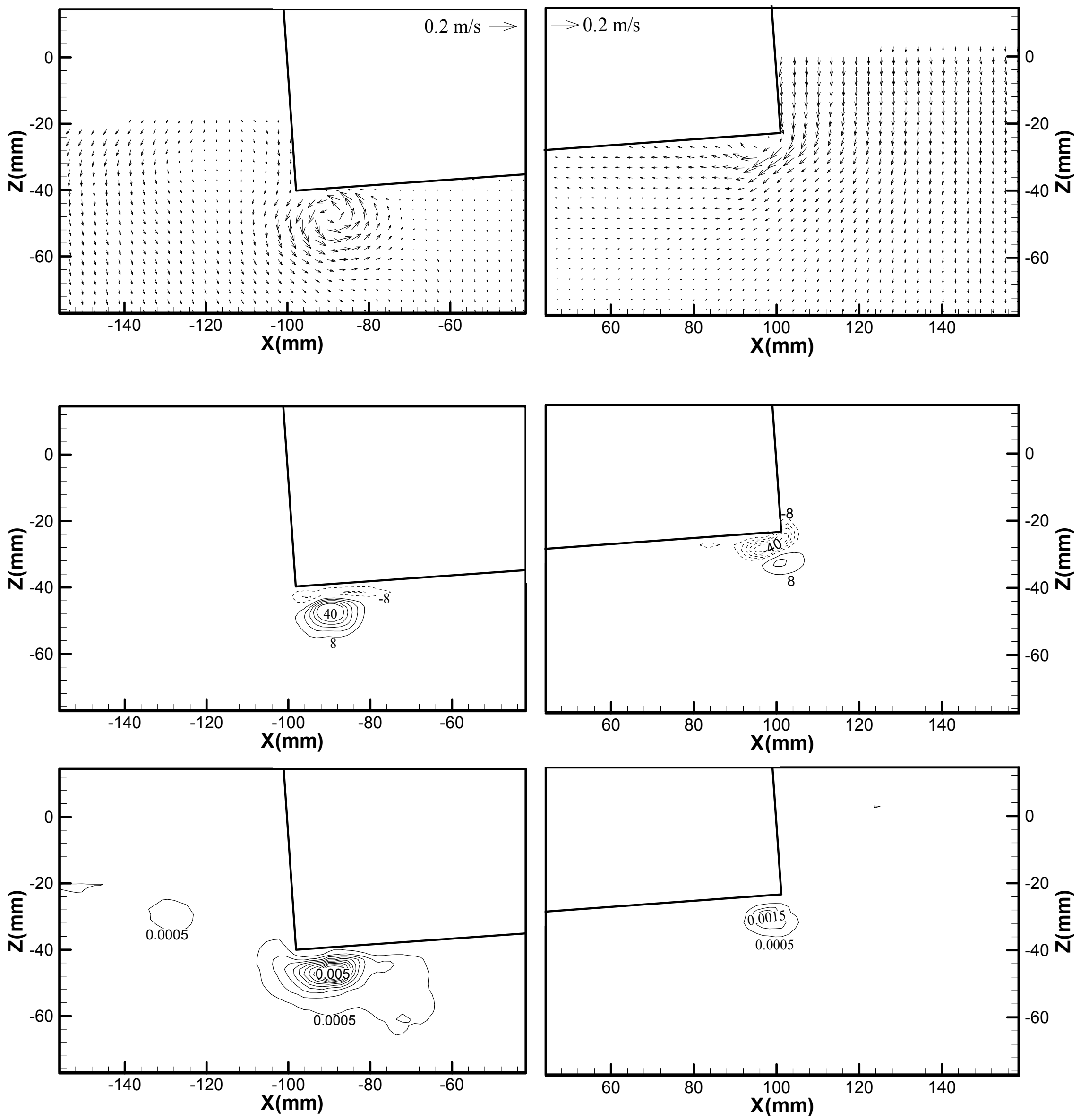

(b)

Fig. 5.6 Continued

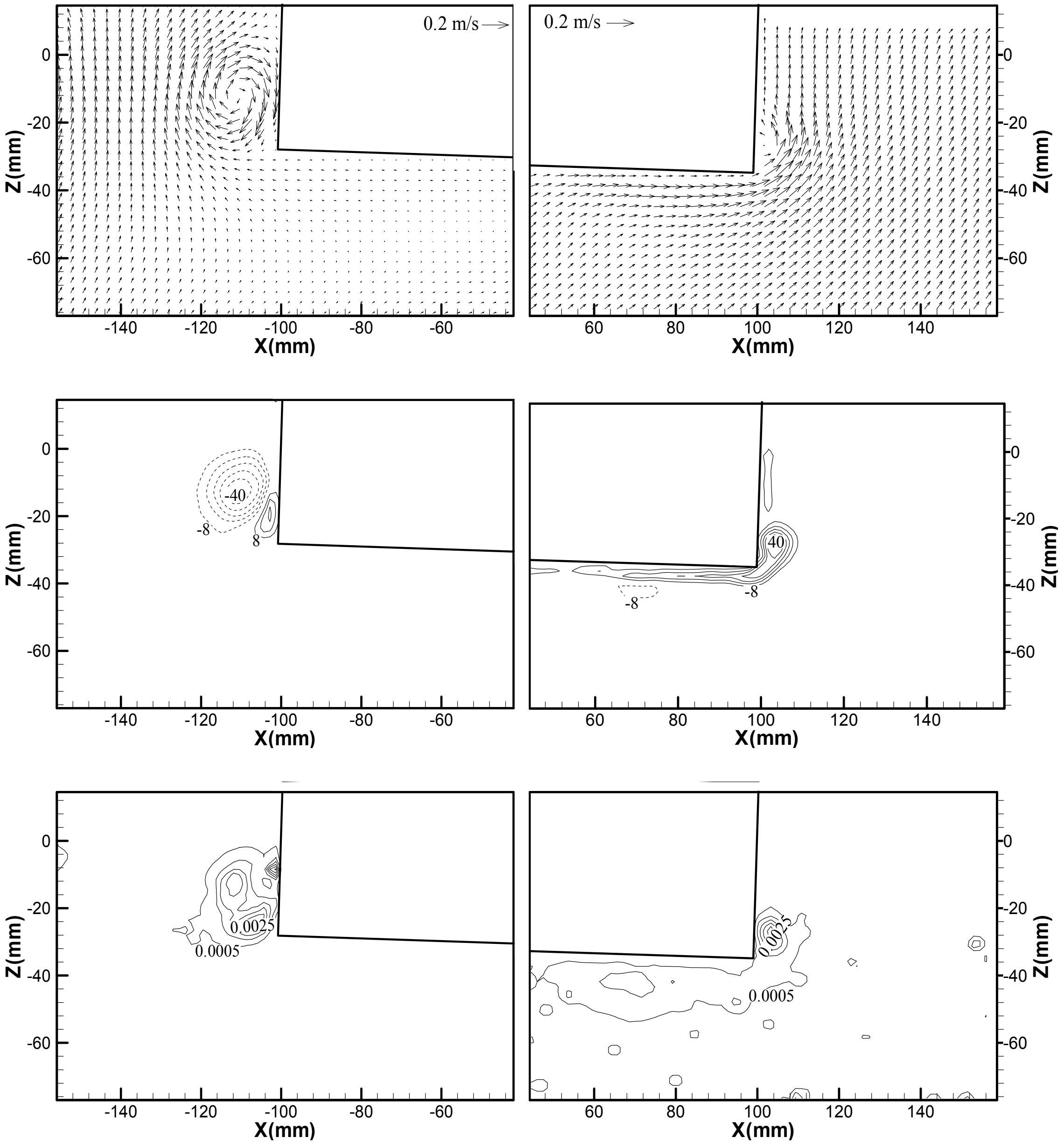

(a)

Fig. 5.7 Mean velocity (the first row), mean vorticity (the second row), and turbulent kinetic energy (the third row) for the case of *T* = 2.0 s. See Fig. 5.6 for the increment of contours in vorticity and turbulent kinetic energy. (a) *t/T* = 0.125 and (b) *t/T* = 0.438.

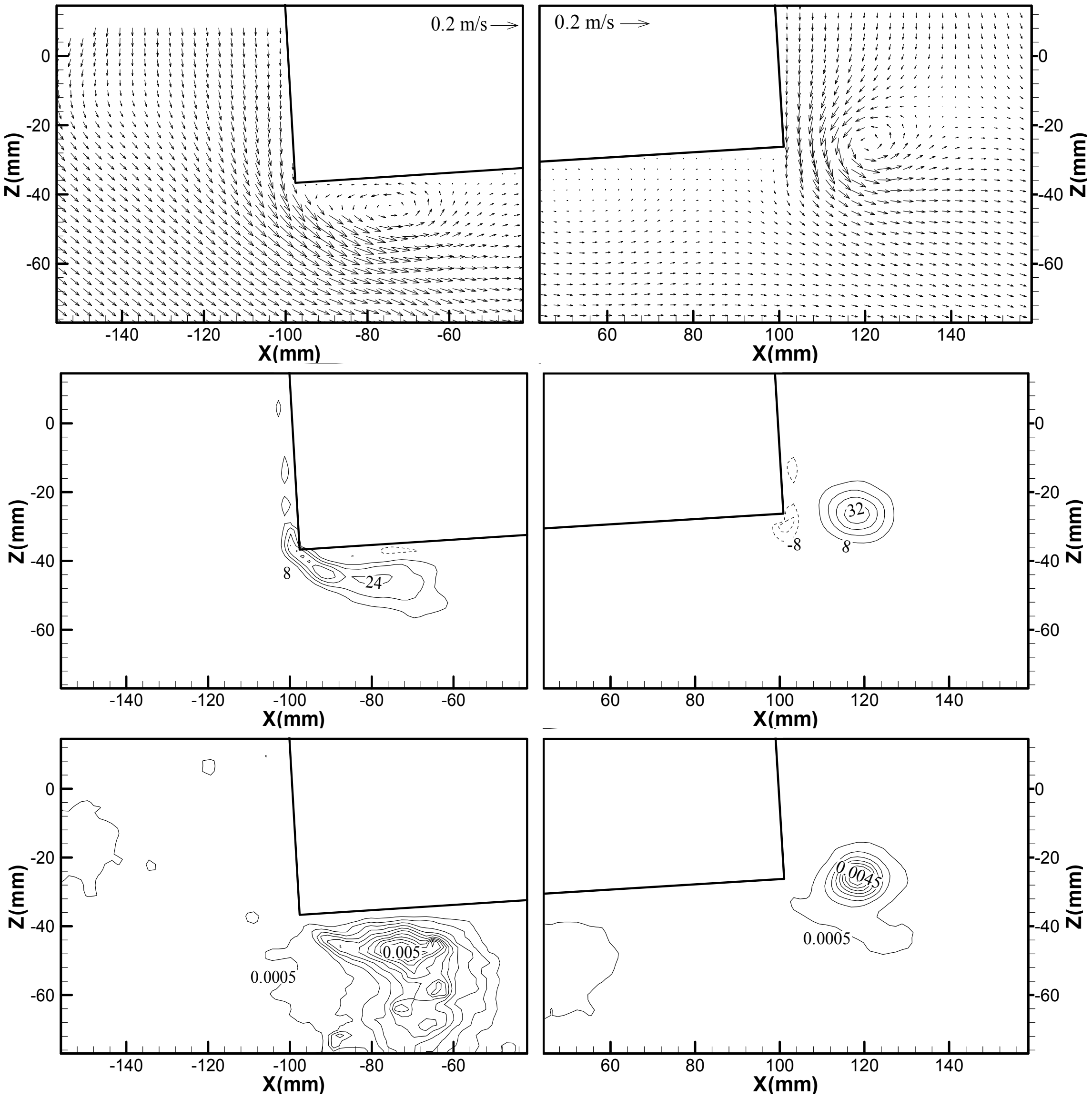

(b)

Fig. 5.7 Continued

Fig. 5.6 (b) shows that the seaward side positive vortex at $t/T = 0.625$ was the most developed under the structure with a large positive roll motion. High correlation between vortex and turbulence is again clearly seen. For the case of $T = 2.0$ s in Fig. 5.7 (a), the negative vortex at the seaward side was completely detached from the corner and well developed at the maximum negative roll motion ($t/T = 0.125$). Fig. 5.7 (b) shows the most developed positive vortex under the corner at the maximum roll angle ($t/T = 0.438$). Note that in both Figs. 5.6 and 5.7, the key vortices were at the side that the structure was moving towards. Therefore there existed no eddy making damping in these two cases with wave periods longer than the structure roll natural period. The pattern of turbulent kinetic energy is similar to that with a fixed rectangular structure in Jung *et al.* (2004). The turbulence intensity over the maximum mean velocity was about 0.25. This level is about one half of its magnitude in wave interactions with a fixed structure (Jung *et al.*, 2004) and in the wake behind a circular cylinder (Townsend, 1956). The reason for such a relatively low level of turbulence is that the structure moved in the same direction with the flow, thus resulting in a lower relative velocity between the structure and the flow.

The trajectories of the key vortices (defined as the two main vortices shed out from each corner during one wave period) for the cases of $T = 1.0$ s and $T = 2.0$ s are shown in Fig. 5.8. Note that the two lower corners of the structure are located at $(x, z) = (-100, -32)$ mm and $(x, z) = (100, -32)$ mm at zero roll angle. The location of each vortex is defined at the maximum absolute vorticity. In both cases, the positive (counterclockwise) vortex at the seaward side was developed under the structure, separated near the corner of the structure, transported towards the free surface by reverse flow, and faded beneath the free surface. In addition, the negative (clockwise) vortex was also generated at the structure corner, developed at the left side of the structure, and decayed back near the structure corner. While the positive vortices at the seaward side reached the free surface and decayed at the location above the stationary water level, the negative vortices at the leeward side did not move that far due to its relatively short trajectory. The length of trajectories at the seaward side is longer than that at the leeward side due to the differences in the water particle displacement resulting from the wave energy transmission. Similarly, it also occurred between the $T = 1.0$ s and $T = 2.0$ s cases. The transmitted wave energy was about 56% ($K_T = 0.75$) and 83% ($K_T = 0.91$) for $T = 1.0$ s and $T = 2.0$ s waves, respectively. Note that none of the trajectories are of closed loops.

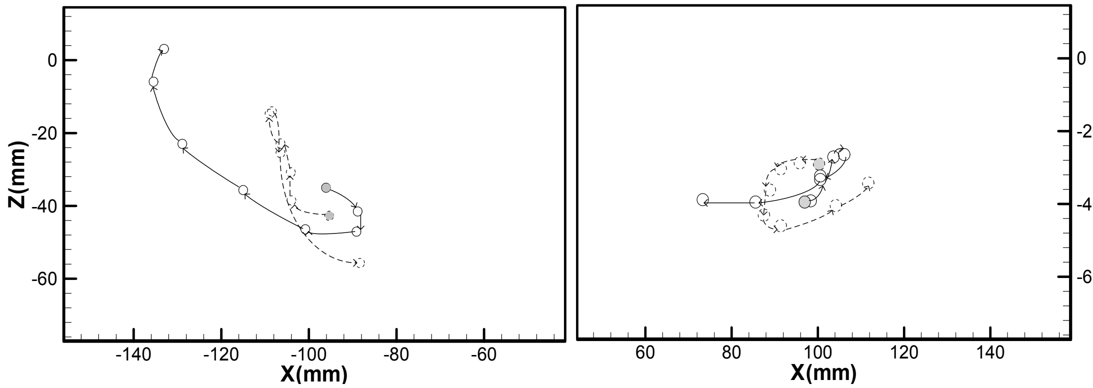

(a) Seaward side ($T = 1.0$ s) (b) Leeward side ($T = 1.0$ s)

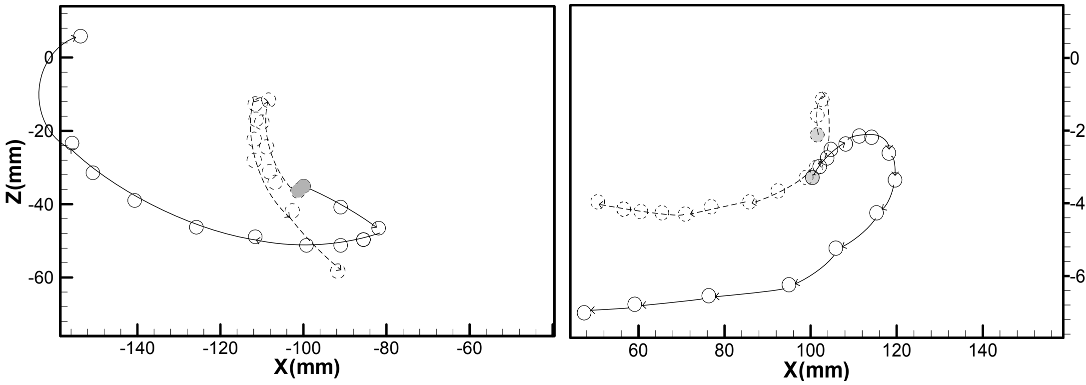

(c) Seaward side ($T = 2.0$ s) (d) Leeward side ($T = 2.0$ s)

Fig. 5.8 Trajectories of the key vortices. Solid circles and lines, positive (counter-clockwise) vortices; dashed circles and lines, negative (clockwise) vortices. The filled circles are the beginning locations when the vortices were generated.

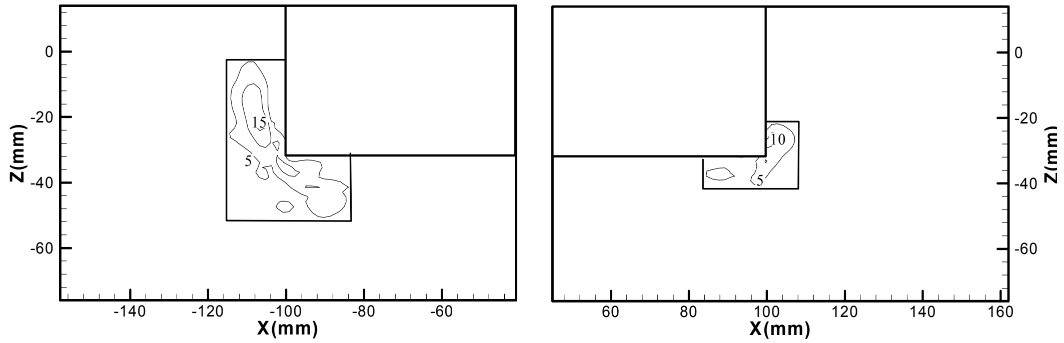

(a) Seaward side, *T*=1.0s (b) Leeward side, *T*=1.0s

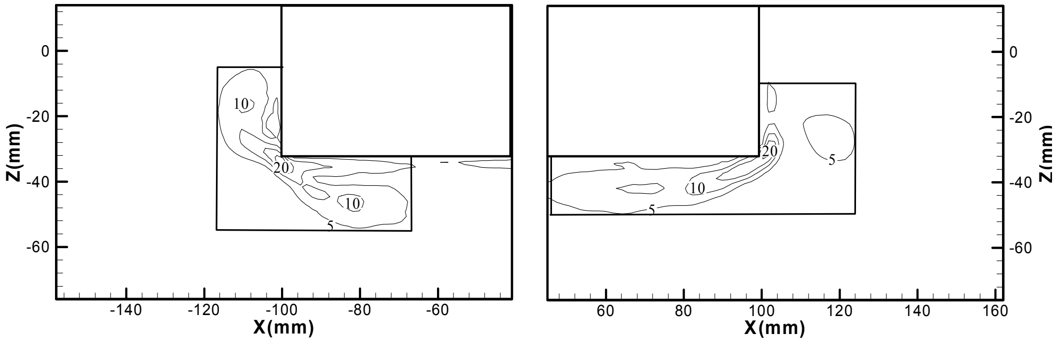

(c) Seaward side, *T*=2.0s (d) Leeward side, *T*=2.0s

Fig. 5.9 Time-averaged (over one wave period) absolute vorticity with an increment of $\Delta\Omega = 5\ \mathrm{s}^{-1}$ between contour lines.

The absolute value of vorticity, $|\Omega|$, and turbulent kinetic energy were averaged over one wave period to distinguish the rotational and turbulent flow region around the structure. The results are plotted in Fig. 5.9 and Fig. 5.10. The Figs. show that the rotational region is strongly correlated with the turbulent region, while the turbulent kinetic energy seems to move farther from the structure. Again, the reason that the vorticity dissipated faster is due to the interaction of vortices of different signs. At the seaward side, the rotational region is confined within one wave particle trajectory of the incoming waves (20 mm for T = 1.0 s and 24 mm for T = 2.0 s, calculated using linear wave theory) from the structure wall or near the structure corners. Because of the relatively low wave transmission for the 1.0 s waves, the vorticity level and rotational area at the leeward side are relatively small. However, this does not apply to the 2.0 s waves because of the higher wave transmission. These results imply that the potential flow theory may be applicable to such a problem except in the region within approximately one or two wave particle trajectories from the structure wall.

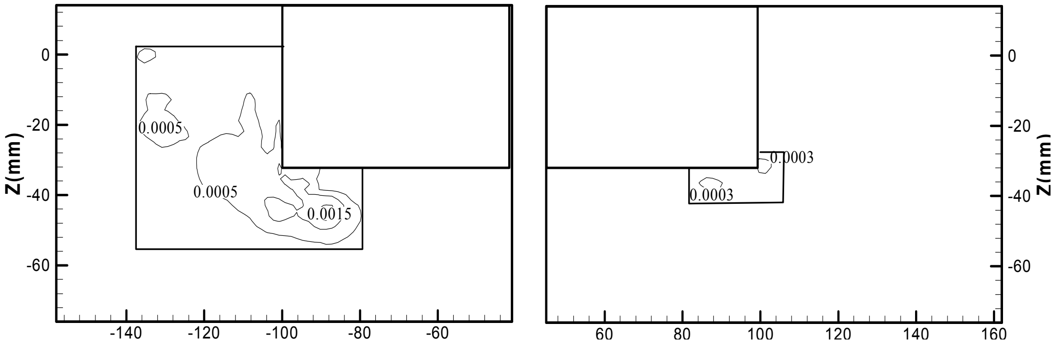

(a) Seaward side, T=1.0s (b) Leeward side, T=1.0s

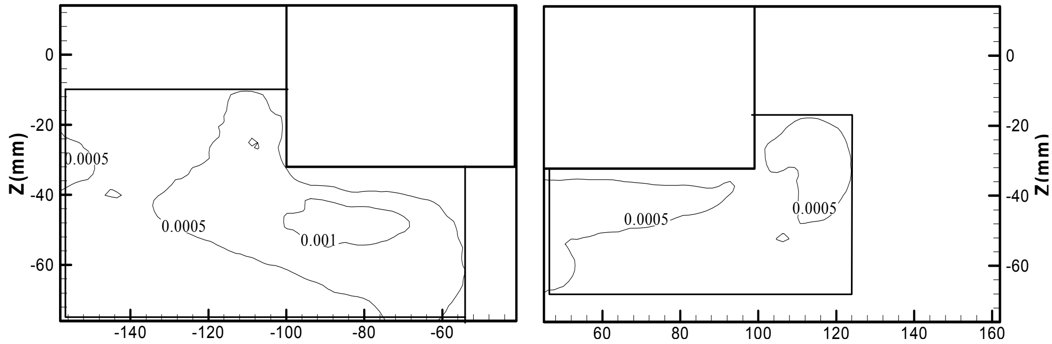

(c) Seaward side, T=2.0s (d) Leeward side, T=2.0s

Fig. 5.10 Time-averaged (over one wave period) turbulent kinetic energy with an increment of $\Delta k_t = 0.0005$ m^2/s^2 between contour lines.

The turbulent length scales and the dissipation rate of the turbulent flow in the vicinity of the rolling structure were estimated and shown in Table 5.1. Since the turbulent flow in this study is far from uniform, the scales were calculated based on the developed turbulent regions at the phases as indicated in the second column in Table 5.1. The Taylor microscale, λ_T, has been frequently used to estimate the turbulent dissipation rate. Following its definition, the Taylor microscale was computed from the longitudinal velocity correlation of the turbulent velocities. The dissipation rate estimated using Taylor microscale is of the same order of magnitude with that directly computed using the PIV velocity field. Because more wave energy was being transmitted in the case of T= 1.0 s than the case of T = 2.0 s, the dissipation rate at the leeward side of the T = 1.0 s case is apparently smaller than that of the T = 2.0 s case. Note that the integral scale is a measure of size of the large energy containing eddies, while the Kolmogorov microscale (η_K) is the length scale of the smallest eddies dissipated by viscosity.

Table 5.1

Estimation of length scales and dissipation rate

Wave period T (s)	Location and phase	Taylor microscale λ_T (m)	Dissipation rate ε (m^2/s^3)	Integral scale Λ (m)	Kolmogorov microscale η_K (m)
1.0	Seaward side Z=-48mm, t/T=0.000	0.0071	0.0021	0.017	0.000148
	Leeward side Z=-48mm, t/T=0.875	0.0052	0.0008	0.007	0.000189
2.0	Seaward side Z=-43mm, t/T=0.438	0.0071	0.0012	0.023	0.000170
	Leeward side Z=-34mm, t/T=0.625	0.0063	0.0011	0.012	0.000174

In the measurements, the PIV spatial resolution, defined as the size of the interrogation window, is about 20 times the Kolmogorov length scale, but equals one-third to one-half of the Taylor microscale at the developed turbulent regions. In order to measure the total turbulent dissipation rate, the spatial resolution is required to be of the size of the Kolmogorov length scale. However, with a spatial resolution of $20\eta_K$ approximately 50% of the total dissipation rate can still be obtained, estimated by using the dissipation spectrum (Pope, 2000). Since the velocity in the y-direction was not measured, the turbulent dissipation was computed by applying equation (3.10) directly to the measured velocity. Although assuming isotropic dissipation in this study could underestimate the dissipation by one-half (Browne *et al.*, 1987), it at least provides the correct order of magnitude.

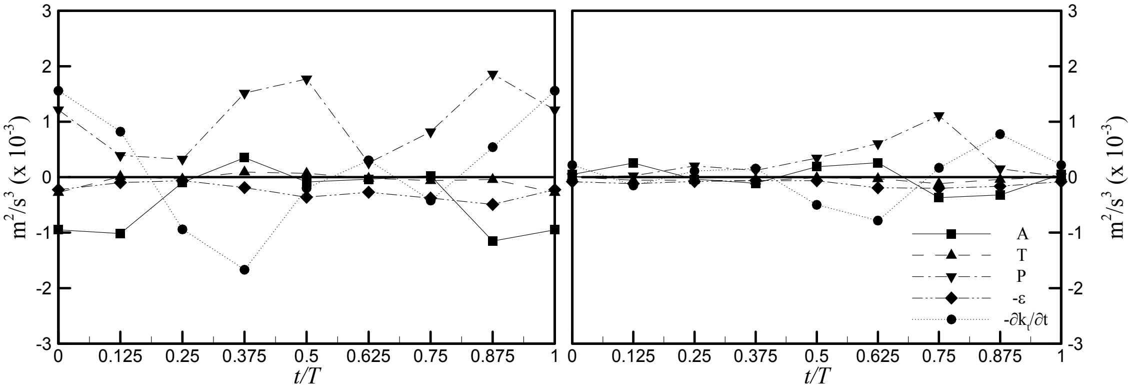

(a) Seaward side, *T*=1.0s (b) Leeward side, *T*=1.0s

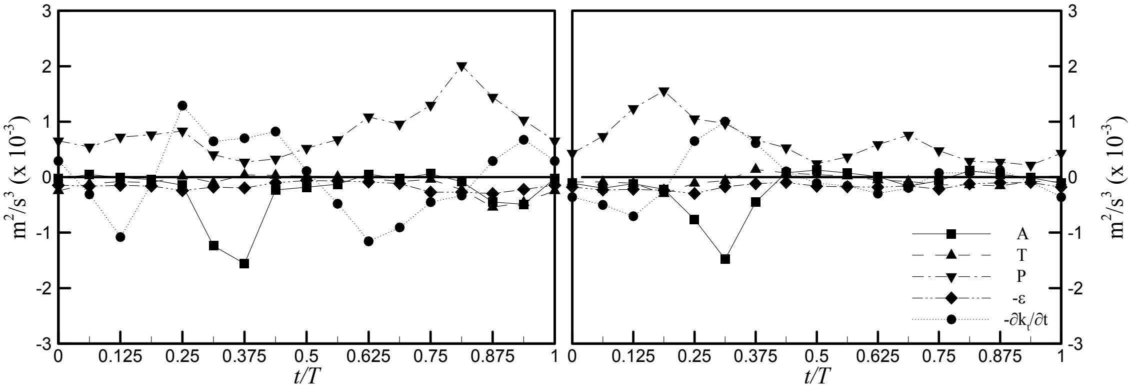

(c) Seaward side, *T*=2.0s (d) Leeward side, *T*=2.0s

Fig. 5.11 Turbulent kinetic energy budget. *A*, turbulent advection; *T*, turbulent transport; *P*, turbulent production; *ε*, turbulent dissipation.

The turbulent kinetic energy budget at both sides of the structure is present in Fig. 5.11. Each term in equation (3.6) was averaged over the turbulent region as shown in Fig. 5.10. Note that the turbulent dissipation term, *ε*, was calculated based on equation (3.10) using the assumption of isotropic turbulence. As expected, more turbulent kinetic energy was produced and dissipated at the seaward side than the leeward side, especially for the case of *T* = 1.0 s. From Fig. 5.11, most turbulent kinetic energy in the turbulent region was gained from turbulent production. The energy was then lost mainly due to the turbulent advection that moved energy out of the region. As expected, most turbulent kinetic energy was produced during the highly vortical and turbulent phases. The value of *ε* is relatively low compared to production, indicating that turbulence was dissipated mostly outside the turbulent region. Note that the calculated turbulent dissipation assuming isotropic dissipation is in good agreement with that calculated based on the balance of turbulent energy budget using equation (3.10) (Jung *et al.*, 2004).

5.4 Concluding remarks

An experimental study on the flow characteristics of regular wave interactions with a two-dimensional rectangular structure was performed using PIV. The rectangular structure was allowed only the roll motion excited by the waves. Three wave trains were tested in the study, of which two have a longer wave period than the structure roll natural period, while the third equals the roll natural period. The flow pattern around the structure varied based on the relative motion between the structure rotation and wave oscillation. The results in the present study showed very distinct features to that reported using a forced oscillatory structure. The effect of typical eddy making damping, which is caused by vortices generated behind the moving body, was illustrated for waves with a period the same as the roll natural period of the structure. For waves with a longer period than the roll natural period, the study showed that the generated vortices were ahead of the rolling body. This means that the generated vortices do not help in reducing the body roll motion when the structure is in waves with a period longer than its roll natural period.

Positive and negative vortices were generated due to corner separation and caused the flow in the vicinity of the structure to become rotational and turbulent. The rotational and turbulent region was confined within one to two times the water particle trajectory of the incoming waves, indicating potential flow theory may be applicable outside such region. The turbulent region is relatively larger than the rotational region. The difference in flow pattern between the seaward side and leeward side of the structure was strongly influenced by wave transmission through the structure. The level of turbulence intensity over the maximum mean velocity at the phases with strong turbulence was about 25% for the two tested cases, which is about one-half of the value in wave interactions with a fixed structure. This is because the relative velocity between the fluid and the structure in the rolling case is slower than that in the fixed case.

CHAPTER VI

DYNAMICS OF RECTANGULAR BARGE IN BEAM SEA

6.1 Experimental set-up and condition

A rectangular acrylic barge with the dimensions of 0.900 m long (*L*), 0.300 m wide (*B*), and 0.05 m high (*D*) was used in the experiment as shown in Fig. 6.1. The barge was located at 20 m from the wavemaker across the entire width of the wave tank in a beam sea condition and the water depth (*h*) was kept as 0.900 m throughout the experiment. The barge was mounted on the tank walls with bars and a pair of hinges through the center of gravity of the barge (0.05m from the keel). These hinge supports allowed the barge to roll and aligned with the water level but restrained it from heave and sway motions.

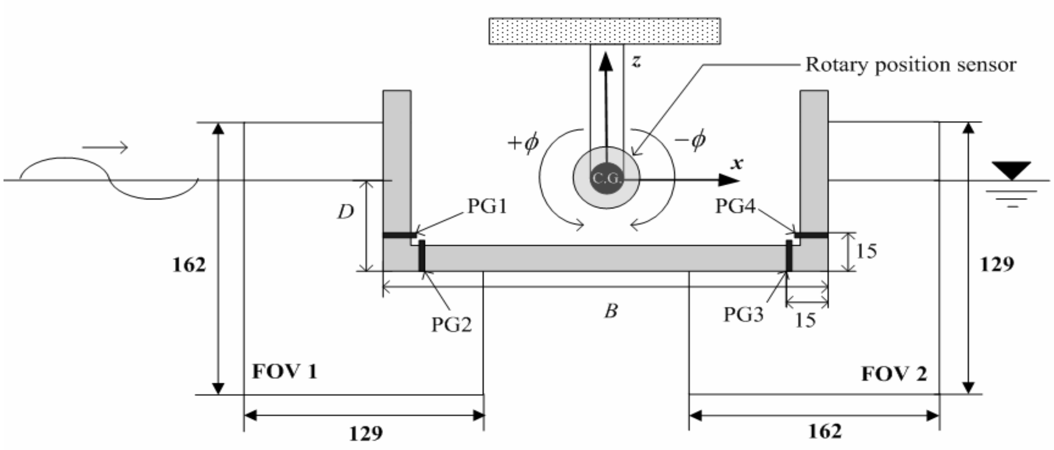

Fig. 6.1 Schematic of the experimental setup and PIV fields of view (unit: mm).

To measure the roll motion of the barge, a the rotary position sensor was installed at the center of rotation which was coincident with the center of gravity. Due to the wave interaction with the fixed and rolling barge, the vortices were separated at the barge corners and the wave motion of fluid, including the incoming, reflected, radiated, and transmitted waves, dynamically varied the pressure field on the barge surface. The variation of dynamic pressure has a significant effect on the exciting moment and the body motion. To measure the dynamic pressure near the barge corner, four pressure transducers were inserted into the side wall and bottom 15 mm apart from each barge corner at both sides as shown in Fig. 6.1. The geometric description of a rectangular barge is schematized in Fig. 6.1 and Fig. 6.2. In Fig. 6.2, G means the center of gravity, B_C the center of buoyancy, and M the metacenter. Metacentric height, $\overline{GM}$, is 0.125m for the barge in calm water. The roll natural frequency (ω_N=6.78 rad/s) was obtained from the free decay test conducted in calm water. The results of the free decay test will be represented with details later.

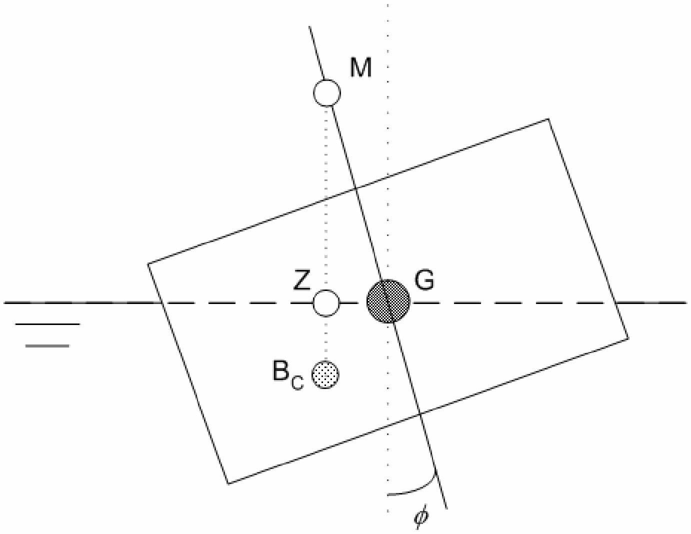

Fig. 6.2 Definition of geometric characteristics.

To understand the interaction between the rectangular barge and waves with the plain condition, regular waves with periods of T=0.5 s~2.0 s, including the roll natural period (T_N=0.93 s) were tested in the experiments. The corresponding wave lengths (λ) and wave heights (H) are listed in Table 6.1. Regular waves were kept in the similar maximum wave slope ($k\zeta_a$, with ζ_a being the mean wave amplitude) for the wave period between 0.5 s and 1.2 s. Because the stroke of the wave maker has a limit in generating a large wave height for the longer wave period, regular waves with a wave period longer than 1.2 s are tested at the similar wave height. To observe the effect of wave height, the experiments were conducted with several wave heights for wave periods, T=0.7 s, 0.93 s, 1.2 s, and 2.0 s.

Table 6.1

Regular wave condition: Bold numbers mean the cases of PIV measurements.

T (s)	ω (rad/s)	λ (m)	H_I(m)	$K\zeta_a$
0.5	12.57	0.39	0.010	0.0805
0.6	10.47	0.56	0.017	0.0950
0.7	8.98	0.77	0.015	0.0616
			0.023	0.0944
			0.029	0.1191
0.8	**7.85**	**1.00**	**0.029**	**0.0912**
0.85	7.39	1.13	0.033	0.0919
0.93	**6.76**	**1.35**	**0.016**	**0.0372**
			0.027	**0.0628**
			0.032	0.0745
			0.040	0.0931
1.0	6.28	1.56	0.044	0.0887
1.1	5.71	1.88	0.057	0.0953
1.2	**5.24**	**2.22**	0.032	0.0453
			0.060	**0.0849**
			0.067	0.0948
1.3	4.83	2.57	0.060	0.0732
1.4	4.49	2.93	0.061	0.0653
1.5	4.19	3.29	0.062	0.0591
1.6	3.93	3.65	0.060	0.0516
1.8	3.49	4.36	0.061	0.0440
2.0	**3.14**	**5.05**	0.026	0.0162
			0.059	**0.0367**

For every wave period in Table 6.1, the measurements were taken from 8 to 12 wave cycles before the reflected waves coming back to the barge so that wave reflection does not affect measurement. Among the waves tested, regular waves of four periods, T=0.8 s, 0.93 s, 1.2 s, and 2.0 s, and two wave heights for the natural roll period (T_N=

0.93 s) were used to obtain the velocity profiles around the barge corners with the PIV system. Wave profiles are shown for one wave period in Fig. 6.3 for the fixed barge case and Fig. 6.4 for the rolling barge case.

The corresponding PIV phases are represented with wave elevations near the barge. The solid line is the wave elevation at a distance of 20 m from wave maker without the barge. The dashed line and dotted line were measured at the locations of 4 cm from the barge in the seaward side and leeward side, respectively. For the duration of measurement, all the regular waves were repeatable within a 2% error, which was calculated from the ratio the standard deviation of elevations of 8~10 successive waves to the maximum wave height. The wave profiles at both sides of the barge due to the wave interaction with the rolling barge were similar to those of the fixed barge.

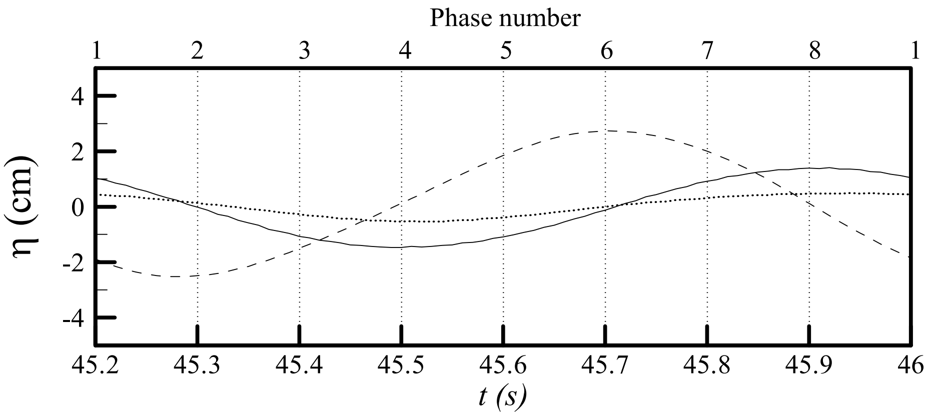

(a) *T*=0.8 s, H_I=0.029 m

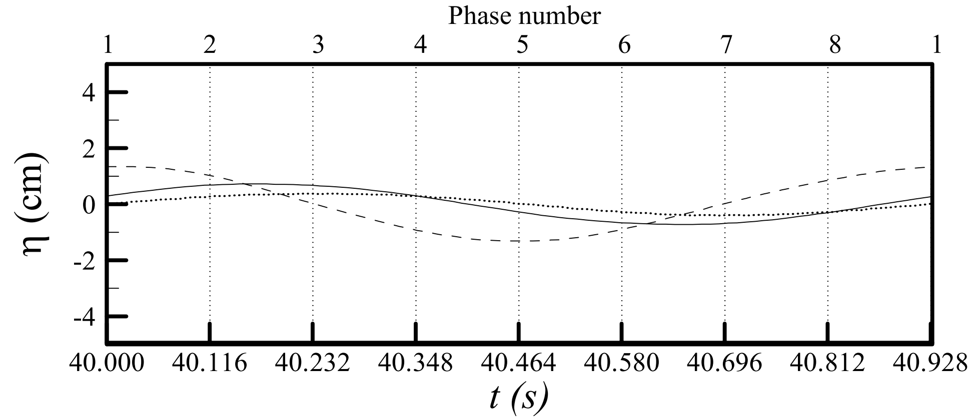

(b) *T*=0.93 s, H_I=0.016 m

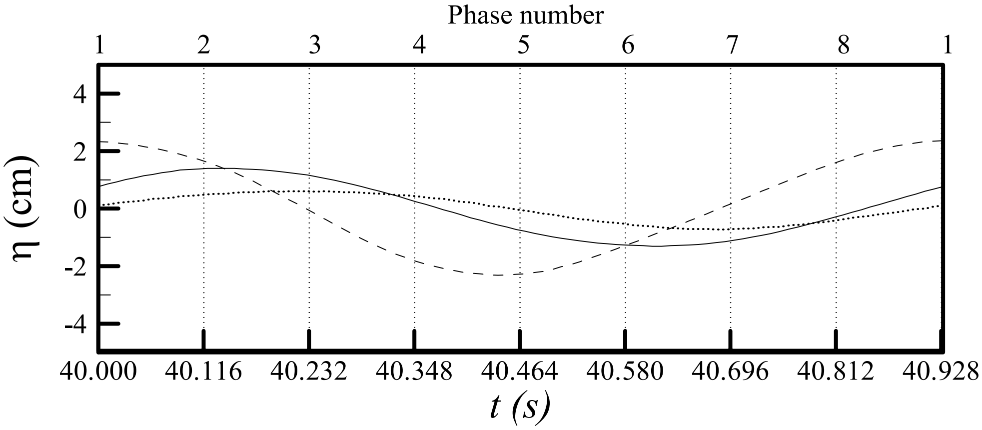

(c) *T*=0.93 s, H_I=0.027 m

Fig. 6.3 Wave profiles of the case of fixed barge (solid line: incident wave at a distance of 20 m from the wave maker without the barge; dashed line: wave at the front of barge; dotted line: wave behind barge).

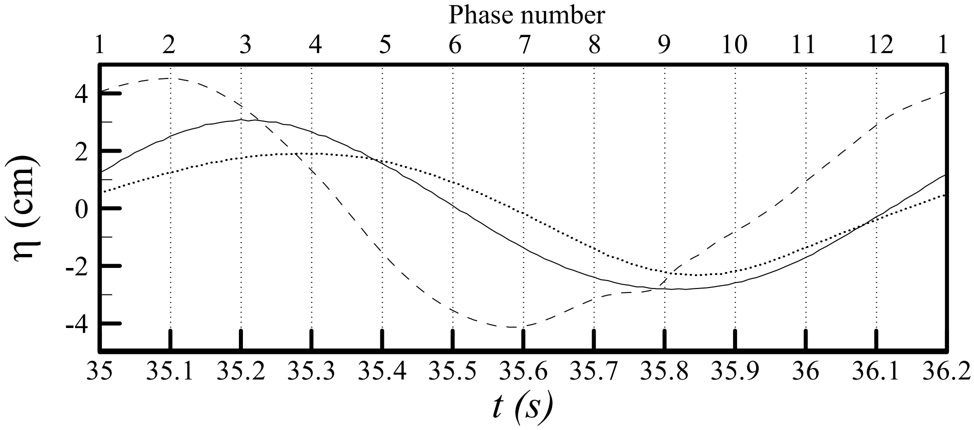

(d) T=1.2 s, H_I= 0.06 m

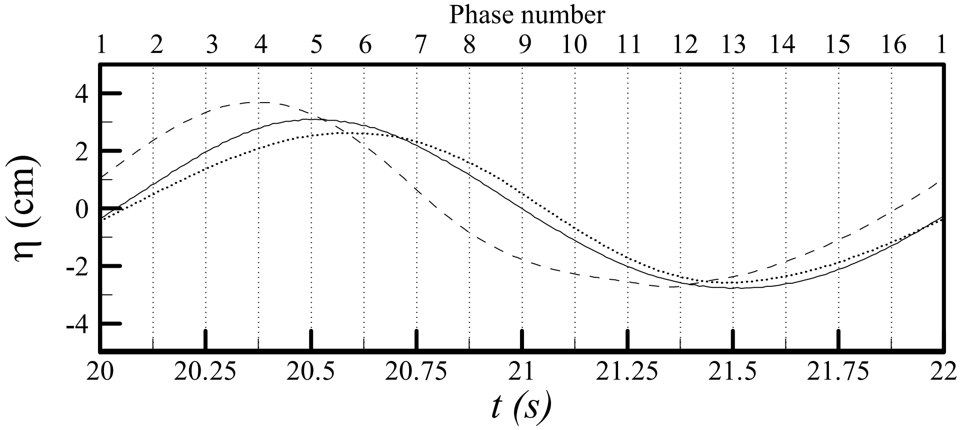

(e) T=2.0 s, H_I= 0.059 m

Fig. 6.3 Continued

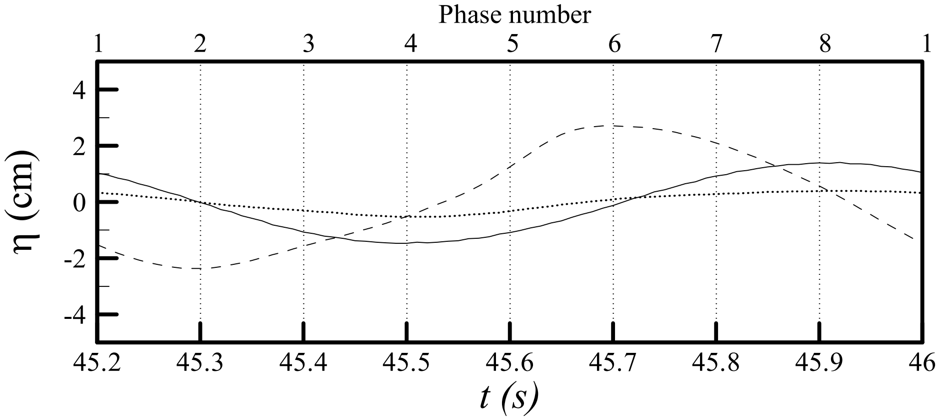

(a) T=0.8 s, H_I=0.029 m

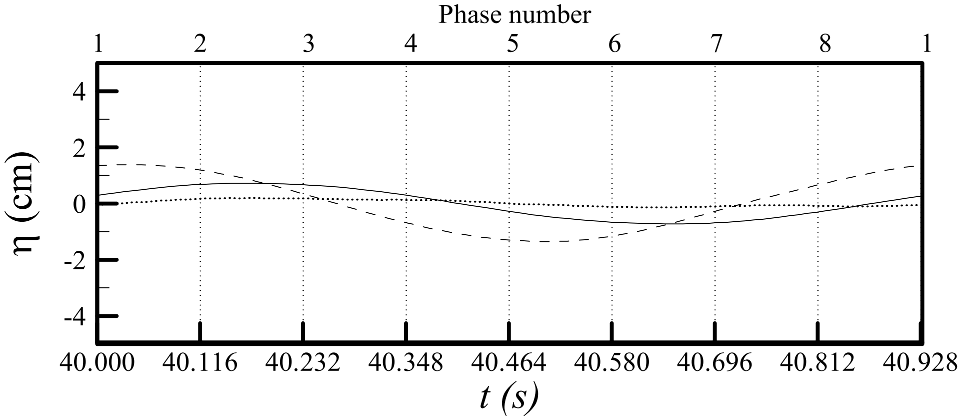

(b) T=0.93 s, H_I =0.016 m

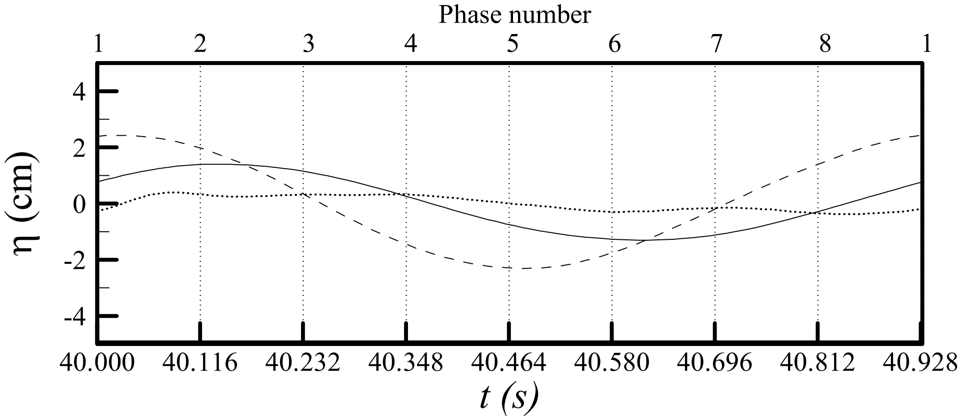

(c) T=0.93 s, H_I =0.027 m

Fig. 6.4 Wave profiles of the case of barge in roll motion (solid line: incident wave at a distance of 20 m from wave maker without the barge; dashed line: wave at the front of barge; dotted line: wave behind barge).

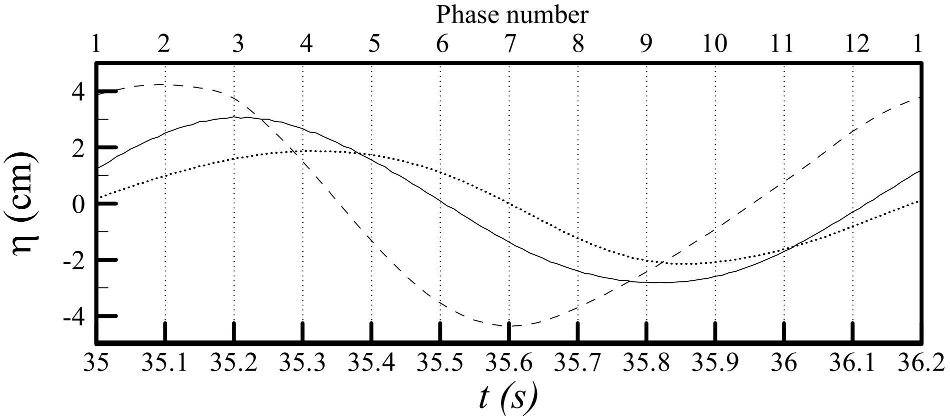

(d) T=1.2 s, H_I= 0.06 m

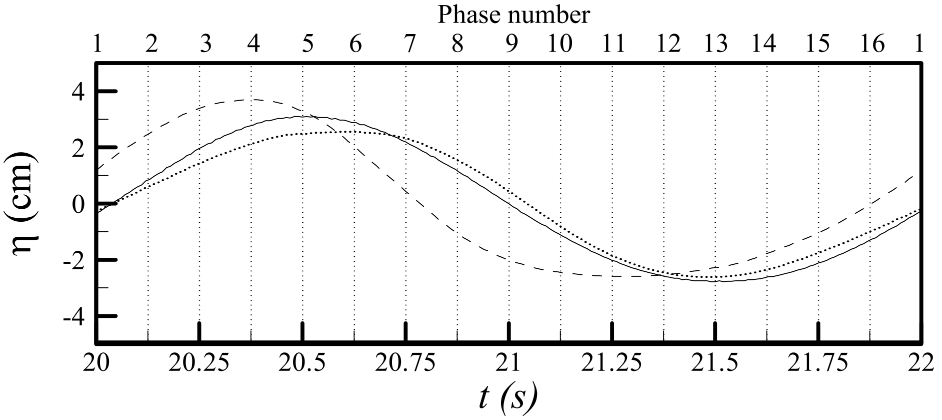

(e) T=2.0 s, H_I= 0.059 m

Fig. 6.4 Continued

6.2 Data acquisition and processing

PIV technique was used to measure velocity profiles in the vicinity of the rectangular structure. The double-frame/single-pulsed cross-correlation method was used for PIV velocity computation. Two fields of view (FOV) were used to obtain velocity fields at the two lower corners of the structure shown in Fig. 6.1. The size of the FOVs was fixed as 162×129 mm^2. FOV 1 and FOV 2 were intended to cover the region in which vorticity was separated at each barge corner. Interrogation windows of 32×32 pixels (4.0×4.0 mm^2) with a 50% overlap between the adjacent windows were used in the PIV velocity computation, i.e., the distance between the adjacent vectors is 2.0 mm.

The time separation (*dt*) between two laser pulses in an image pair was adjusted between 3 ms~5 ms to limit the instantaneous maximum particle displacement being less than one-third of the interrogation area. Because the CCD camera was limited to obtain image pairs at a rate of 4 Hz, PIV images were captured at an adjusted rate between 2~4 Hz according to a wave period. An example of a signal to trigger the PIV system is plotted with an incoming wave elevation in Fig. 6.5.

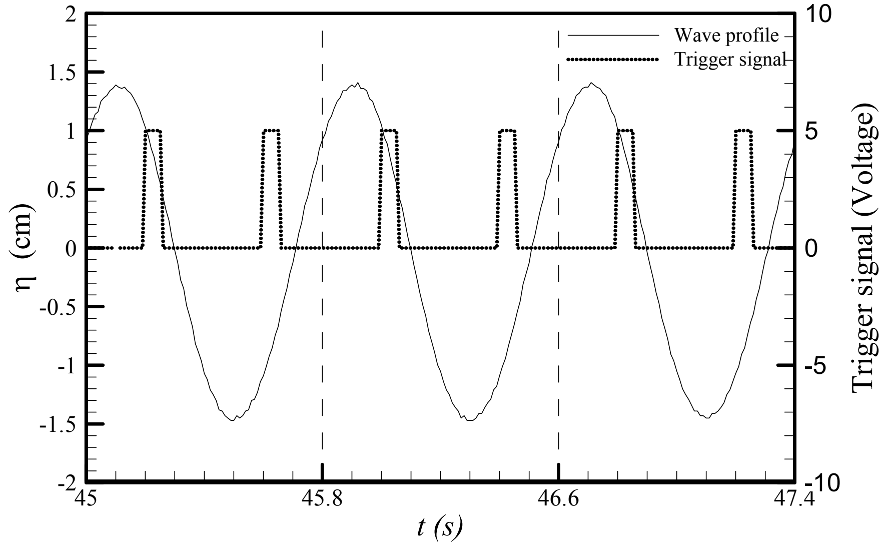

Fig. 6.5 Synchronization of wave elevation and signals to trigger PIV system (T=0.8 s).

Because the image acquisition rate of the CCD camera was limited in 4 pairs of images per second, a series of velocity profiles for a wave period was obtained by the 3~4 repeated test runs. Each velocity profile which was separately acquired by different experimental trials was arranged in regular sequence within wave cycles. Then, time differences between successive velocity profiles in a sequence of each wave period are listed in Table 6.2. As the periodic wave and barge motion was repeated for every wave period before the reflected waves coming back to the barge, velocity profiles were smoothed by phase averaging from 8~12 instantaneous velocity measurements at the same phase of each regular wave.

Table 6.2

Acquisition number of velocity profiles within a wave period

T (s)	Number of measured phases within a wave period	Time difference between successive velocity profiles (s)
0.8	8	0.100
0.93	8	0.116
1.2	12	0.100
2.0	16	0.125

Two double-wired resistant-type wave gauges were used to measure the free surface elevation with a computer housing a DAQ board. The gauges were located at 4 cm in front and behind the rectangular structure, respectively, to measure the wave elevation at the PIV fields of view. A rotary position sensor was utilized to measure the roll motion of a barge by the wave. Its full range was ±60°, and the combined error, the sum of linearity error and nonrepeatability error, was less than 0.2 % of the full scale output. Pressure at two locations near each barge corner was measured with a piezoresistive pressure transducer, which has the combined error less than 1% of the full scale output. Every data from wave gages, rotary position sensor, and pressure gages were taken at a sampling rate of 100 Hz.

6.3 Dynamic characteristics of a rectangular barge in roll motion

The equation of motion for rolling is

$$I' \frac{d^2\phi}{dt^2} + b\frac{d\phi}{dt} + c\phi = M_0 \cos w_e t \tag{6.1}$$

The virtual mass moment of inertia for rolling (I') is the sum of the moment of inertia of the actual mass of the barge (I) and the added mass moment of inertia (δI). The damping moment coefficient (b) is most prominent due to wave making damping, eddymaking damping, and friction damping. The restoring moment of a ship for roll motion is the transverse moment at any particular angle of inclination expressed as

$c\phi = \Delta\overline{GZ}$ where Δ is a displacement of the barge and $\overline{GZ}$ is the arm of the righting moment as shown in Fig. 6.2. For small angles of inclination, the restoring moment coefficient (c) can be expressed by $\Delta\overline{GM}$. The exciting moment $M_0 \cos\omega_e t$ is thought of as fluctuating with the wave encountering frequency ω_e.

A free decay test is a common engineering practice to obtain the damping coefficient and the natural frequency. The free decay test was conducted in calm water and successive decaying amplitudes of roll motion are plotted against a base of time in Fig. 6.6. The natural frequency (ω_N) was computed by the spectrum analysis in Fig. 6.7, which was 6.78 rad/s, and the natural period (T_N) is 0.93 s for the roll motion.

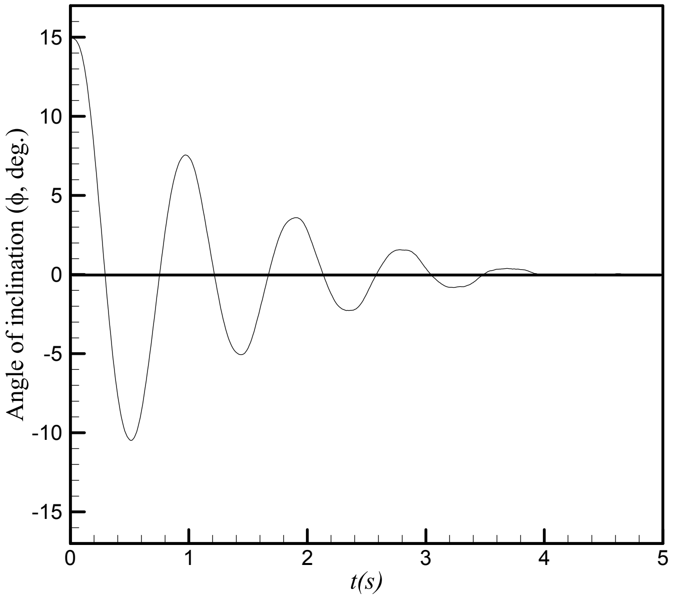

Fig. 6.6 Roll free decay test in calm water.

The barge was initially inclined with an angle of 15° and the roll motion decayed after each cycle by the damping effect. For rolling in calm water, the equation of motion is

$$I'\frac{d^2\phi}{dt^2} + b\frac{d\phi}{dt} + \Delta\overline{GM}\,\phi = 0 \tag{6.2}$$

or

$$\frac{d^2\phi}{dt^2} + 2\varsigma\,\omega_N \frac{d\phi}{dt} + \omega_N^2\phi = 0 \tag{6.3}$$

where I' is the virtual mass moment of inertia $(I + \Delta I)$, b is the damping moment coefficient, and ζ is the damping factor with $2\varsigma\,\omega_N = \dfrac{b}{I'}$ and $\omega_N^2 = \Delta\overline{GM}\big/I'$.

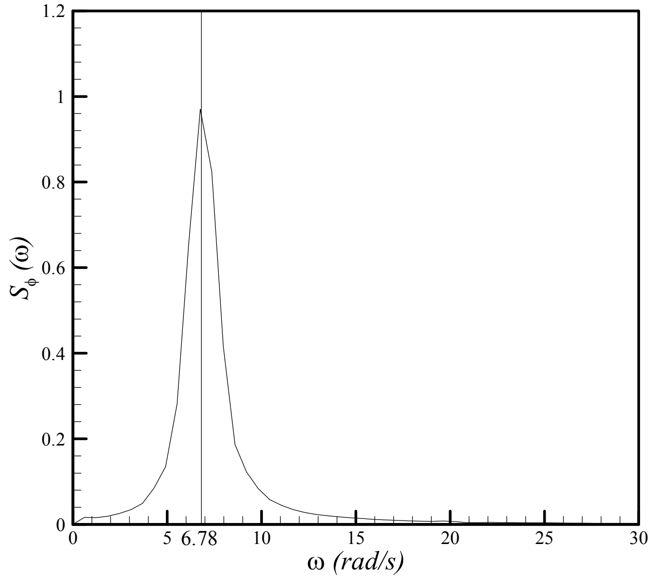

Fig. 6.7 Spectrum of roll motion in free decay test.

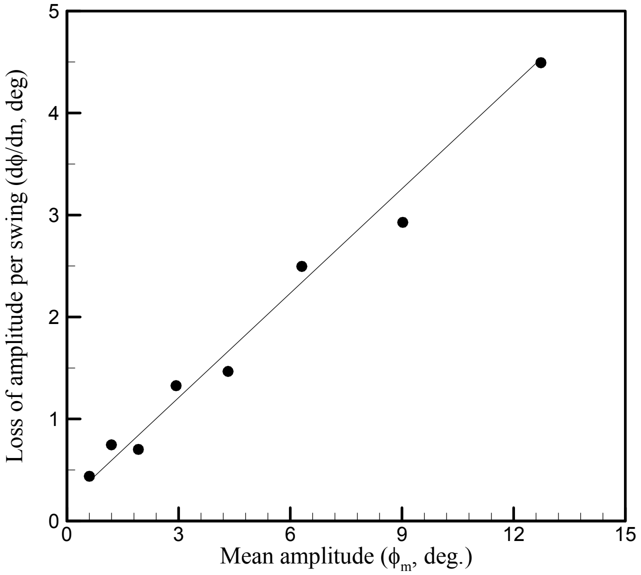

Fig. 6.8 Curve of extinction.

In Fig. 6.8, the decrease of inclination for a single roll is shown. The figure plotted against the interpolated inclinations is called the mean angle of roll (ϕ_m). The damping coefficient, b=0.519, can be calculated from this curve (Bhattacharyya, 1978). Therefore, the damping ratio (ζ) is 0.106 and the virtual mass moment of inertia (I') is 0.36 kg·m^2. To obtain the added mass moment of inertia (ΔI) for the rectangular barge, the moment of inertia of the actual mass of the barge ($I = 0.236\,\mathrm{kg \cdot m^2}$) was computed by the natural frequency ($\omega_{N_{air}} = 1.25\mathrm{rad/s}$) from the free decay test in air. Subsequently, the added mass moment of inertia for rolling is 0.124 kg·m^2.

The magnification factors ($\phi/k\zeta_A$) from experiments are compared with results of a linear potential theory (the constant panel method) including only wave making damping shown in Fig. 6.9 as a function of ω/ω_N. Experiments were conducted in the similar condition of the maximum wave slope ($k\zeta_A$) between 5.23 rad/s and 12.56 rad/s wave cases as listed in Table 6.1. Because high amplitude waves with wave frequencies lower than ω = 4.83 rad/s are hard to produce in the wave tank, the wave heights were set at 6 cm for such cases. To test the nonlinearity due to the variation of wave height, the wave of ω =12.56 rad/s and 5.23 rad/s were performed with three wave heights and the waves of ω =6.78 rad/s with four wave heights. The magnification factors of ω =12.56 rad/s and 5.23 rad/s were similar at the different wave heights. However, the magnification factors of the natural period, T=0.93 s (ω=6.78 rad/s), varied with the wave height. It is observed from Fig. 6.9 that the magnification factor decreases with the increasing wave height at the natural frequency. Downie *et al.* (1988) showed that the roll response at the natural frequency is a function of the wave height. Because the linear potential theory includes only the wave making damping but not the viscous damping (eddy making damping), the roll motion calculated by the theory is significantly exaggerated at the natural frequency. The magnification factors from theory and experiment agree well at the higher frequency waves and underestimate at the lower frequency waves (Salvesen et al., 1970 and Downie *et al.*, 1988).

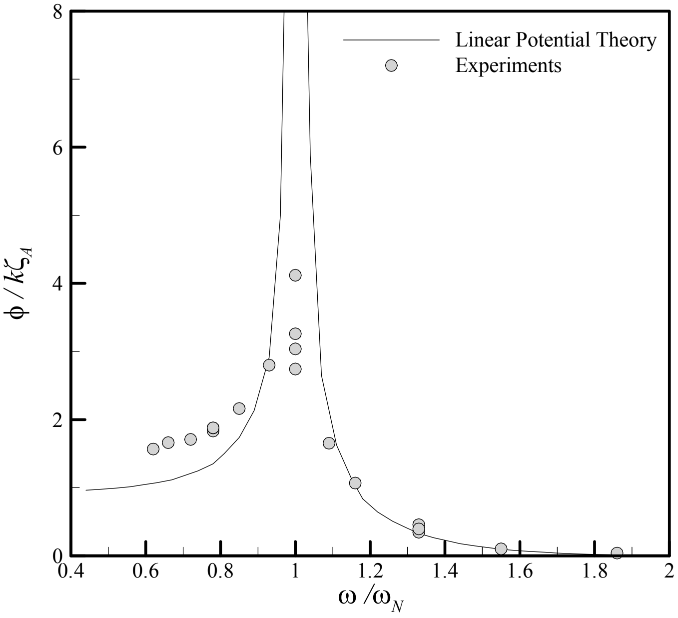

Fig. 6.9 Magnification factors for the roll motion in beam sea.

6.4 Response of roll motion of the rectangular barge

The inclined angle of the barge induced by the regular wave is plotted with the phases of PIV images over one period in Fig. 6.10. For the measurement duration, the roll motion was repeatable within the 2% error. In Fig. 6.11, the amplitude spectrums of the incident waves and the roll motion are presented. All the regular waves have only their own frequency component. The rectangular barge had the predominant motion at the same frequency with each incident wave (ω= 7.85 rad/s, 6.78 rad/s, and 5.24 rad/s). At the incident wave frequency of 3.14 rad/s, the roll motion of double frequency was present with similar magnitude with the first harmonic motion shown in Fig. 6.11. This double frequency roll motion may be caused by the buoyancy restoring moment ($\rho g \nabla \overline{GZ}$) which is dependent upon the inclined angle of the barge and the relative position of the barge in the waves. Because the barge was restricted in the heave motion, its displacement was varied with wave elevations at both sides of the barge and the metacentric height ($\overline{\mathrm{GM}}$) was changed due to the variation of the displacement and the moment of inertia for the waterplane area. These variations of the displacement and the metacentric height were included to calculate the buoyancy restoring moment. The time histories of buoyancy restoring moment (M_B) are given with the roll motion in Fig. 6.10 and its spectrum in Fig. 6.11. For all the waves except ω=3.14 rad/s waves, the first harmonic restoring moments are most dominant. However, the case of wave frequency ω=3.14 rad/s has the second harmonic restoring moment of similar magnitude with the first harmonic moment. With a lower wave height of H=0.026 m for the wave frequency 3.14 rad/s, the roll motion of double frequency was reduced and the second harmonic restoring moment was also decreased. From these results, the second harmonic roll motion of double frequency at the wave frequency 3.14 rad/s may be caused by the variation of the buoyancy restoring moment. As wave height increased, the buoyancy restoring moment was varied significantly by the large change of displacement of the barge due to the restriction in heave motion.

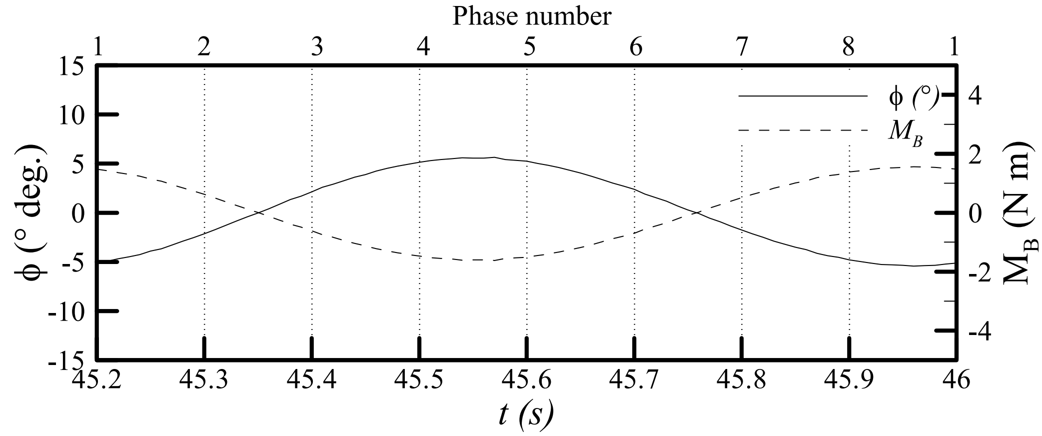

(a) T=0.8 s, H_I = 0.029m

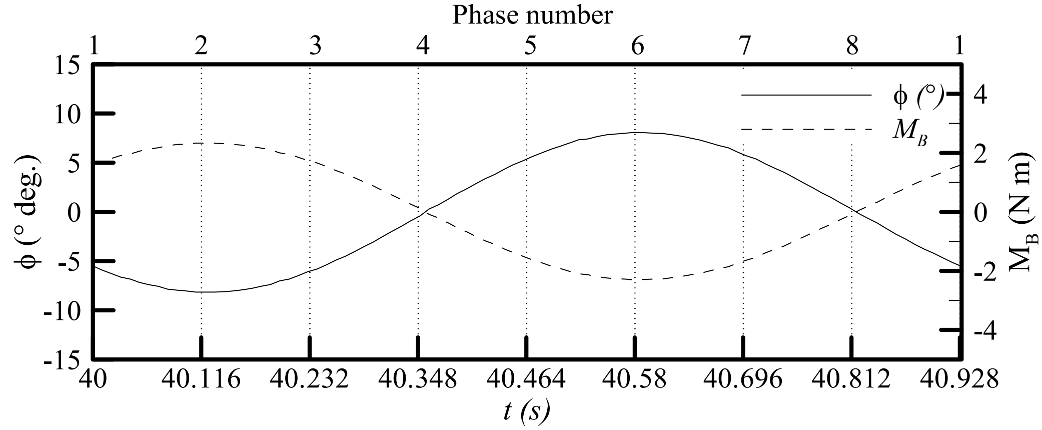

(b) T=0.93 s, H_I = 0.016m

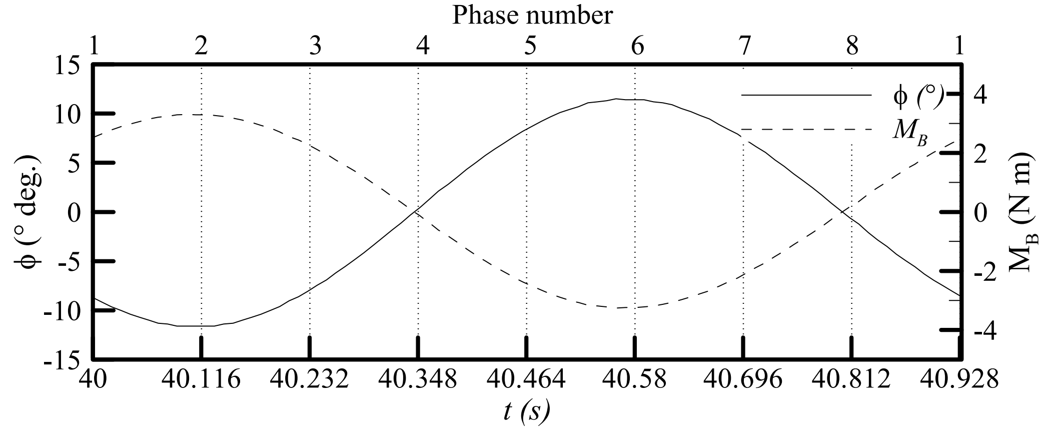

(c) T= 0.93 s, H_I = 0.027 m

Fig. 6.10 Roll motion, ϕ(°), and restoring moment, M_B.

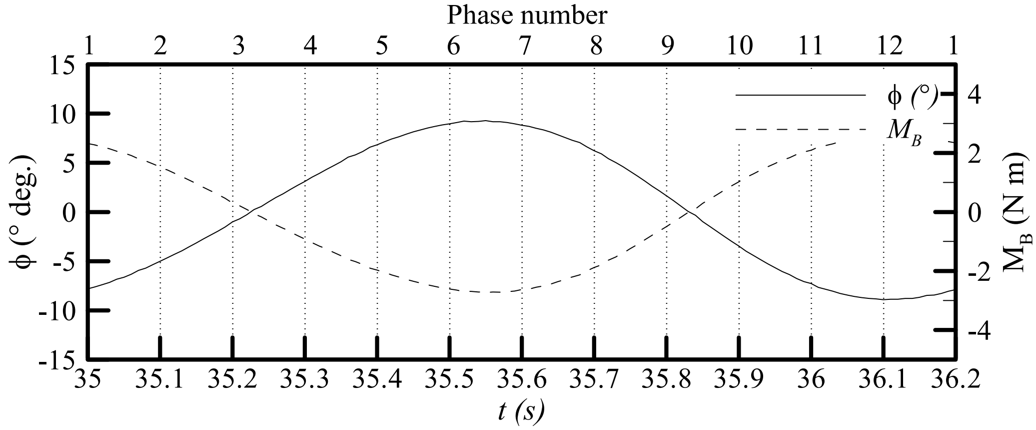

(d) T=1.2 s, H_I = 0.06 m

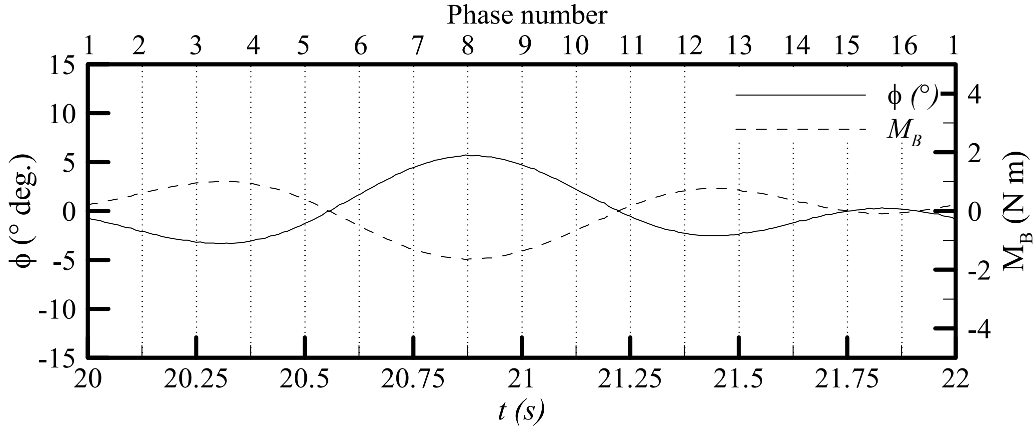

(e) T=2.0 s, H_I =0.059 m

Fig. 6.10 Continued

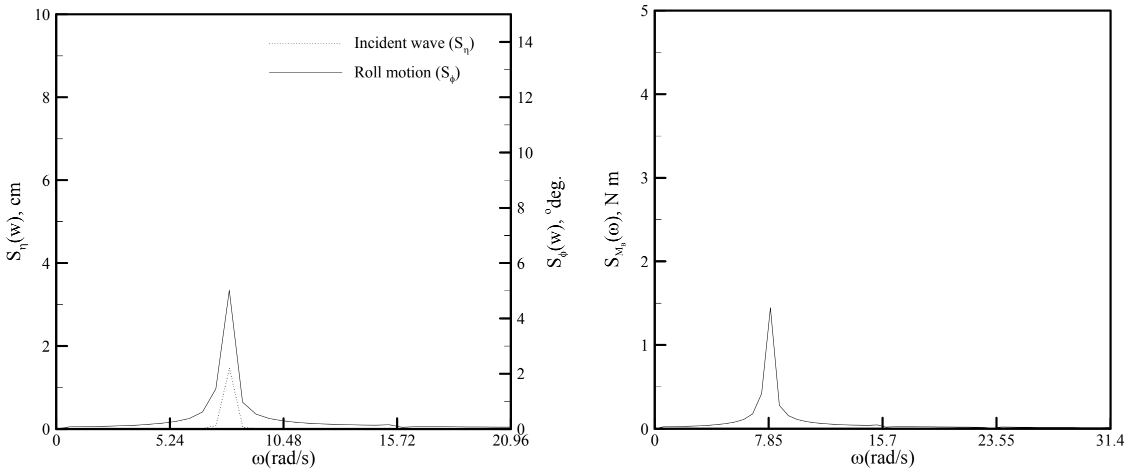

(a) T=0.8 s, H_I = 0.029 m

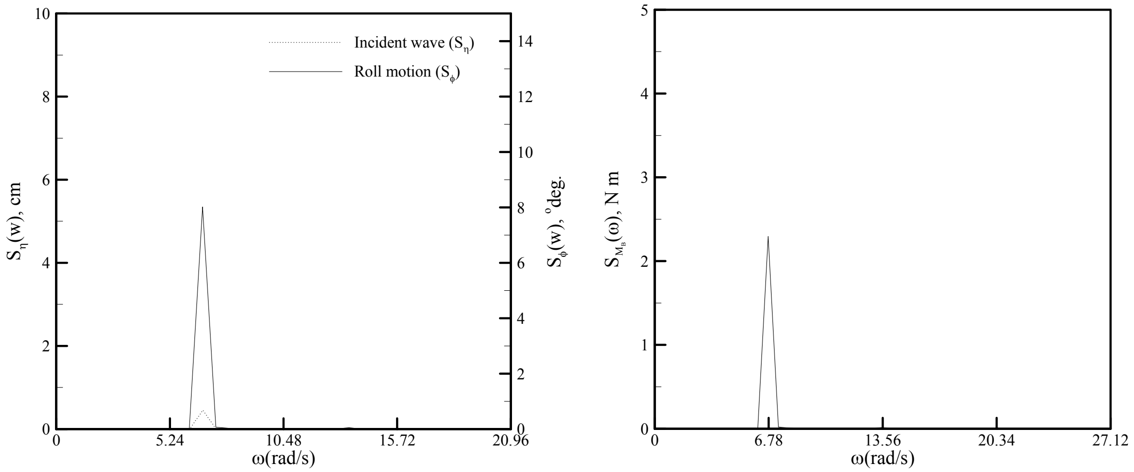

(b) T=0.93 s, H_I =0.016 m

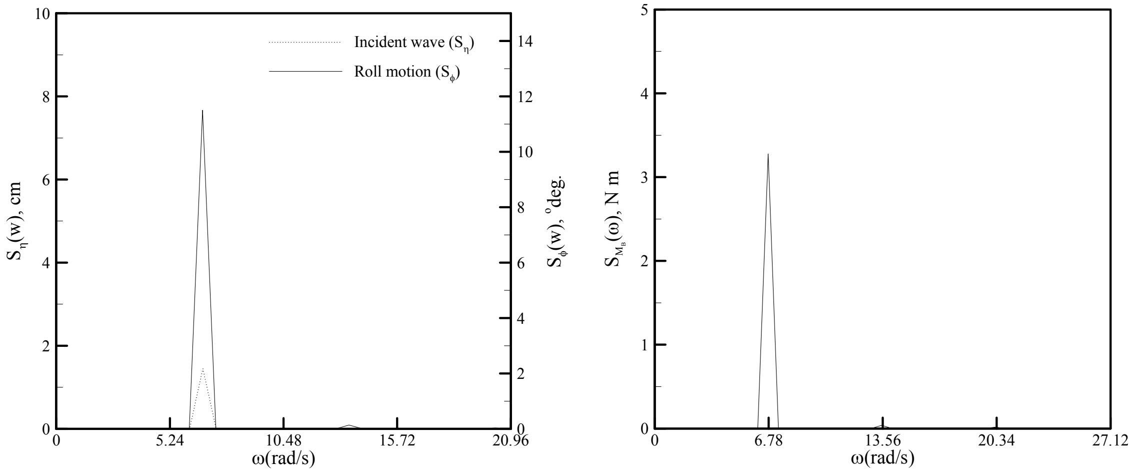

(c) T=0.93 s, H_I =0.027 m

Fig. 6.11 Spectrum of roll motion and restoring moment.

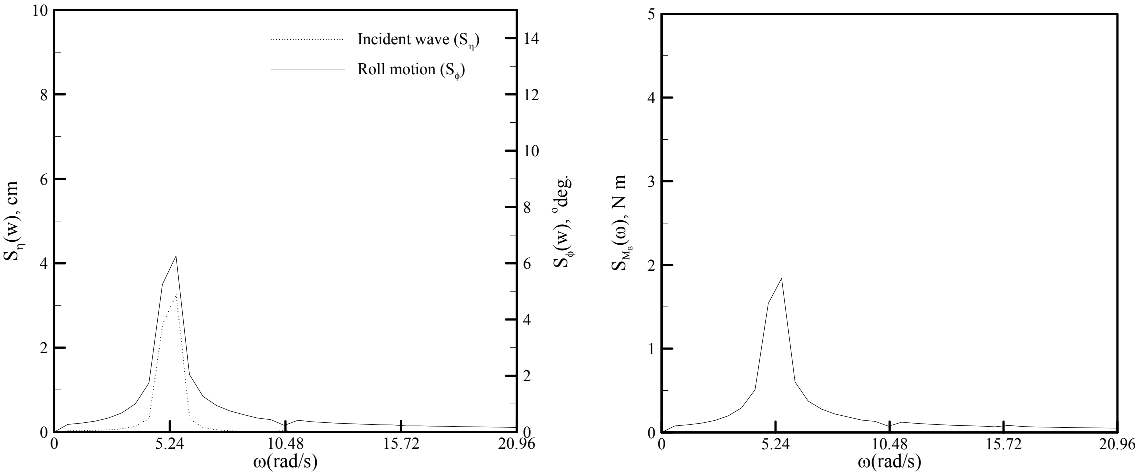

(d) *T*=1.2 s, H_I =0.060 m

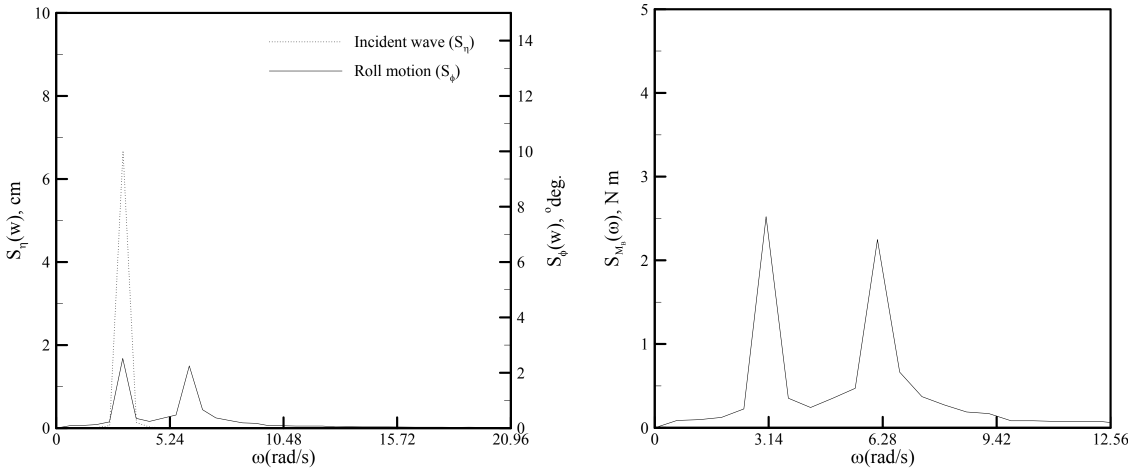

(e) *T*=2.0 s, H_I =0.059 m

Fig. 6.11 Continued

6.5 Transmission of wave energy

Floating structures in an open sea have been designed as breakwaters to attenuate the incident waves. Floating breakwaters have ensured the acceptable wave attenuation at relatively low costs and can be categorized into the flexible floating structure and rigid floating structure. Because this experiment was conducted for the fixed and one degree of freedom (roll motion) condition, it can be used for the comparison between the fixed and rolling structures. The transmission coefficient, $K_T=H_T/H_I$, which is the ratio of transmitted wave height to incident wave height, measures the breakwater performance in this chapter. The pressure fields at the structure corners and the velocity profiles will be described later in the chapter. Fig. 6.12 shows the transmission coefficient versus the ratio of the width of the structure to wave length (B/λ).

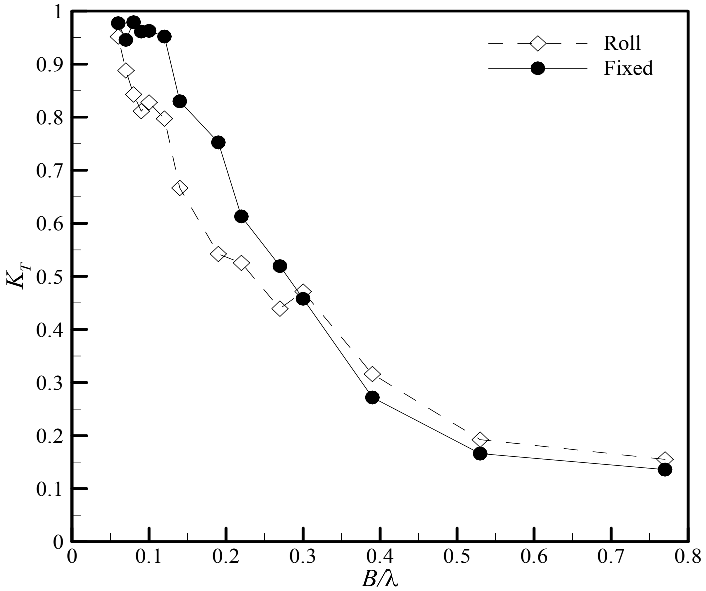

Fig. 6.12 Transmission coefficient (K_T).

It is observed from this figure that the transmission coefficient decreases with increasing B/λ. Namely, the floating breakwater can effectively attenuate the shorter period wave than the longer period wave and the width of the breakwater plays a significant role in its performance. Although the floating breakwater allowed in the roll motion transmitted more wave energy than the fixed floating breakwater for B/λ ≥ 0.3, it is more effective on wave reduction when B/λ < 0.3. This means that waves generated by the structure motion augmented the transmitted waves in B/λ < 0.3. In contrast, waves generated by the relatively long period motion canceled the waves that passed the structure. In this case, the roll motion of floating structure induced by the incident wave enhanced the attenuation of relatively long period waves. Regular waves were tested in similar wave steepness (0.026~0.03) for B/λ ≥ 0.14. For conditions lower than B/λ = 0.14, the wave height was fixed at 6 cm. Therefore, the wave steepness for the case of B/λ < 0.14 was reduced to 0.023 ~ 0.013. Because the transmission coefficient increases with decreasing wave steepness (Arunachalam and Raman, 1982), it may be smaller for the wave of B/λ < 0.14 if it was kept in the same wave steepness.

6.6 Pressures at the corners of rectangular barge

Fixed or floating structures in the wave condition have dynamically responded to incident wave with the significant effect in beam seas. The structure experiences the complicated interactions with the incident, reflected, diffracted, and transmitted waves and viscous problems such as the vortex shedding. Those phenomena arising from the coupled interaction between structures and waves have resulted in the noteworthy pressure variation which affected the behavior of structure. To investigate those influences upon the roll motion, dynamic pressures at both corners were measured and compared between the fixed and the rolling rectangular barge. Four pressure gages were installed on the side walls and bottoms of both corners (see Fig. 6.1). *P1* and *P2* are pressures on the side wall and the bottom of the seaward side, and *P3* and *P4* pressures on the bottom and the side wall of the leeward side at 1.5 cm located from the corner, respectively. The pressure gages (PG2 and PG3) on the barge bottom were located at a horizontal distance of 13.5 cm and PG1 and PG4 at a vertical distance of 3.5 cm from the center of rotation. If the pressure on the bottom for the corner was the same magnitude with the side wall, its moment to force the barge was about 4 times larger than that of the side wall of the corner.

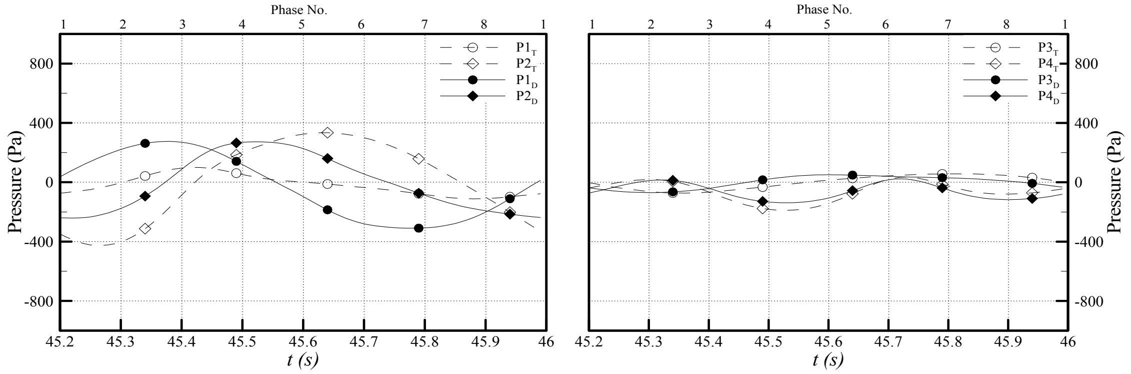

(a) T= 0.8 s, H_I= 0.029m

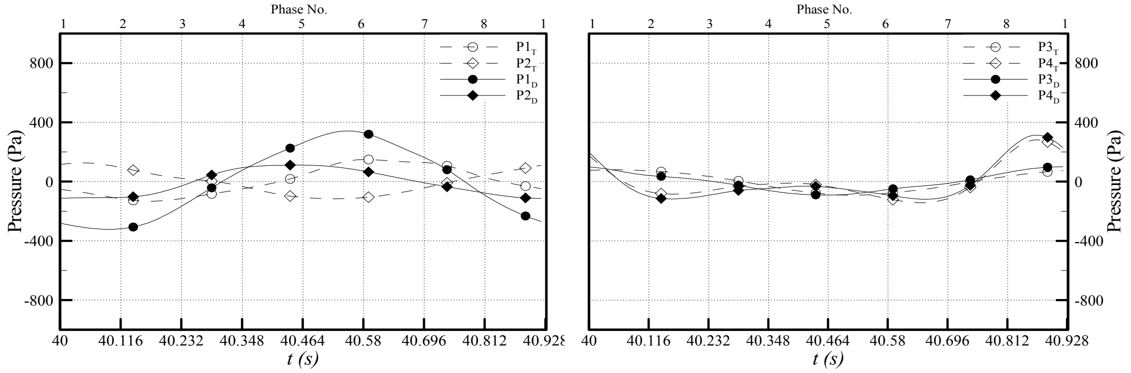

(b) T= 0.93 s, H_I=0.027 m

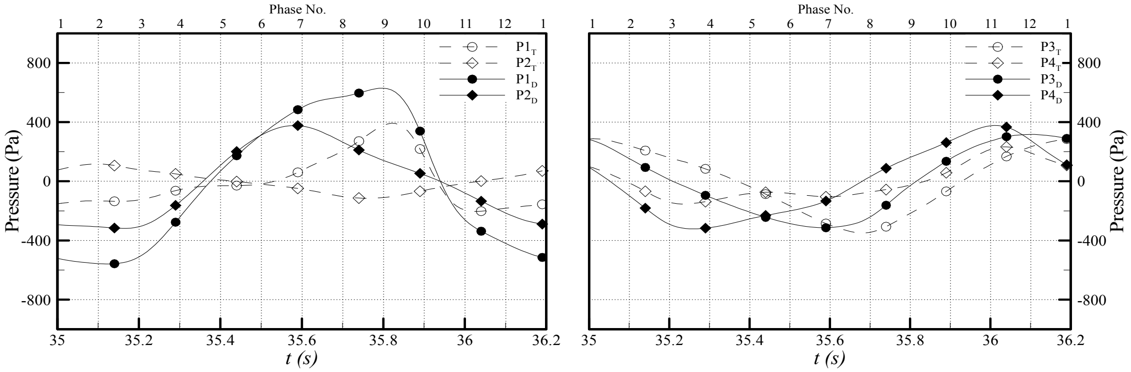

(c) T=1.2 sec, H_I=0.060 m

Fig. 6.13 Time series of pressure near barge corners in the fixed condition. Right column: seaward side, left column: leeward side.

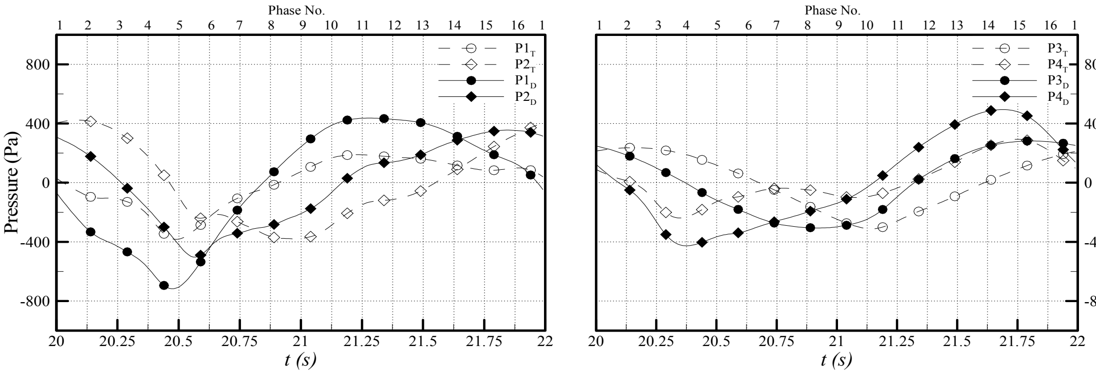

(d) T=2.0 sec, H_I=0.059 m

Fig. 6.13 Continued

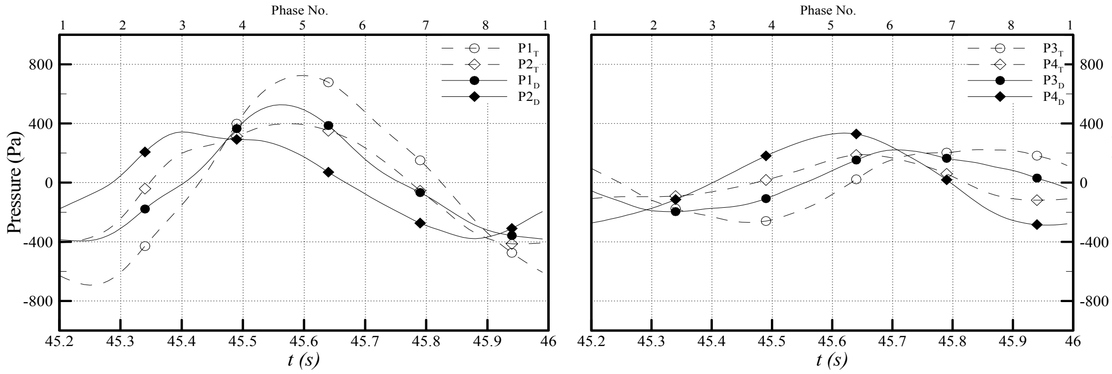

(a) T=0.8 s, H_I=0.029 m

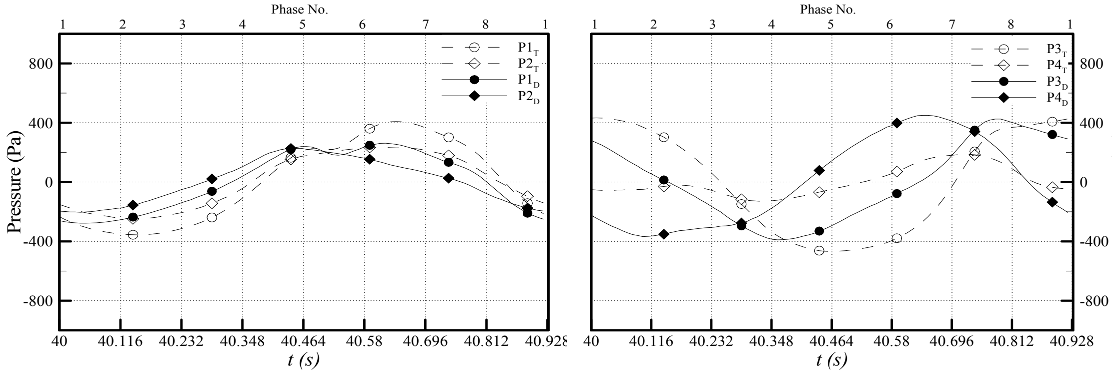

(b) T=0.93 s, H_I=0.027 m

Fig. 6.14 Time series of pressure near barge corners in roll motion. Right column: seaward side, left column: leeward side.

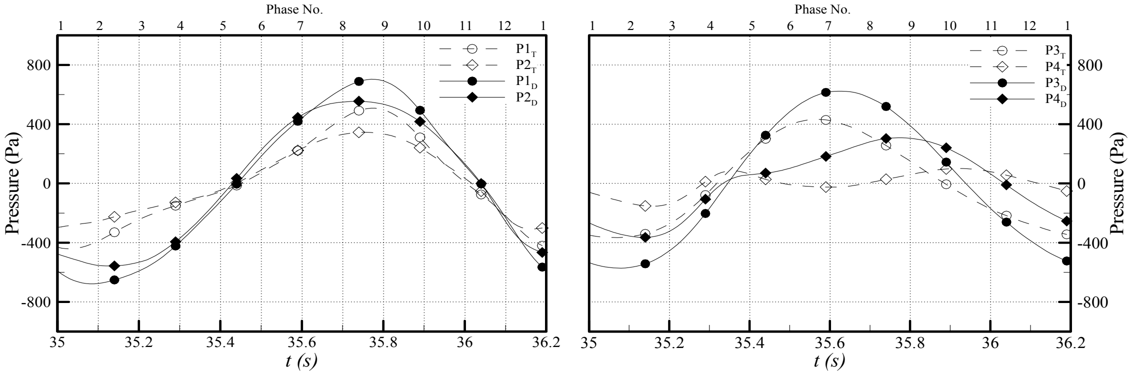

(c) T=1.2 s, H_I=0.060 m

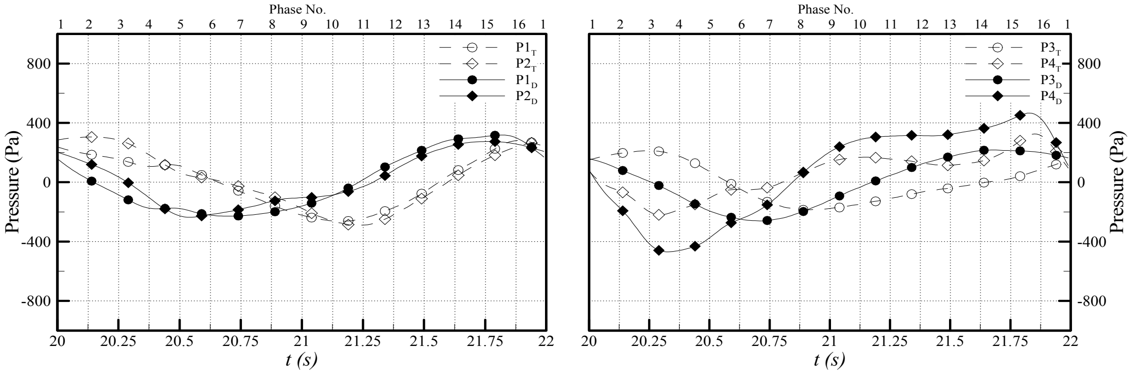

(d) T=2.0 sec, H_I=0.059 m

Fig. 6.14 Continued

The measured total dynamic pressure (P_T) includes the induced dynamic pressure (P_D) due to the fluid kinematics as well as the effect of body motion and the water level dynamic pressure (P_W) due to the free surface fluctuation. The total dynamic pressure (P_T:$P1_T$~$P4_T$) and the induced dynamic pressure (P_D:$P1_D$~$P4_D$) are plotted in Fig. 6.13 and Fig. 6.14. The time series of the total dynamic pressure (P_T) and the induced dynamic pressure (P_D) of the fixed barge and the rolling barge were the phase averaged values for 8~10 periods from the starting time of *x*-axis in each figure. The variation of dynamic pressures will be roughly discussed for the four wave periods in this chapter, because it is very hard to explain it with only pressure data. It will be investigated over with velocity profiles, wave surface, and body motion from PIV results.

For the seaward side of the fixed barge shown in Fig. 6.13, the total dynamic pressures, $P1_T$ on the side wall and $P2_T$ on the bottom, are roughly out of phase and in phase with the wave level elevation at the seaward side, respectively. If the water dynamic pressure (P_W) is subtracted from the total dynamic pressure, the induced dynamic pressures (P_D) on the side wall are larger or smaller than the total dynamic pressure, which means that the induced dynamic pressure may reduce or increase the total dynamic pressure. The induced dynamic pressures ($P1_D$ and $P2_D$) were reduced to the minimum negative pressure when the free surface came up at that side, and vice versa. The amplitudes of dynamic pressures (P_T and P_D) on the leeward side clearly depend on the wave transmission coefficient (K_T). As the more wave energy can be transmitted through the barge with longer wave period (see Fig. 6.12), the dynamic pressures at the leeward side were raised with the higher transmission coefficient (K_T).

For the case of the rectangular barge in roll motion, the dynamic pressures at both corners were measured at the same condition with the fixed barge cases except the one degree of freedom for the roll motion. In consequence of the roll motion of the rectangular barge, it shows the different pattern of dynamic pressure variation for the fixed barge case presented in Fig. 6.14. Wherever the vortex was separated at the side wall or the bottom, the total and induced dynamic pressures (P_T and P_D) of the seaward side had the similar phase and amplitude on the side wall and bottom of the corner. Namely, it seems that the dynamic pressure on the barge was affected by other reasons as well as the vortex shedding.

For the leeward side of the relatively short period waves (T=0.8 s and 0.93 s), induced dynamic pressures are significantly increased by the roll motion in comparison with the fixed barge. It is, also, important to note that the induced dynamic pressures (P_{2D} and P_{3D}) on the bottom of both sides were varied out of phase to each other. For waves, T=1.2 s and 2.0 s, however, the induced dynamic pressures at the both sides were in-phase and balanced with similar magnitudes. When the barge was inclining to the maximum roll motion in the positive direction (phase 5 shown in Fig. 6.10) at the wave of the roll natural period (T=0.93 s), the maximum positive dynamic pressure ($P2_D$)

pushed up the bottom of the seaward side and the minimum negative dynamic pressure ($P3_D$) pulled back the bottom of the leeward side. It is obvious that these dynamic pressures in opposite directions may play a role in the reduction of the roll motion, which has been known as the viscous damping due to the vortex shedding.

In the next chapter, all the dynamic pressures are going to be examined again in detail with PIV results including velocity profiles, the vorticity, the wave elevation, and the roll motion.

6.7 Dynamic responses in roll motion with velocity and vorticity

PIV technique was employed to take the velocity profiles of incident waves without structure and wave interactions with the rectangular barge in the fixed condition and in roll motion. The mean velocity profiles and vorticity contours were provided with the phase averaging from 8 or 10 instantaneous velocity measurements of 8 phases for T= 0.8 s and 0.93 s, 12 phases for T= 1.2 s, and 16 phases for T= 2.0 s for one wave period. All the results of PIV were synchronized by the computer housing DAQ board with wave elevations and the roll motion of the barge. The phases of velocity maps correspond to the free surface elevation in Figs. 6.3 and 6.4 and the inclined angle, respectively in Fig. 6.11. Because velocity profiles of the incident wave were synchronized with those of the wave interaction at each phase, it can help to investigate the flow deformation due to the diffraction effect in the case of fixed barge and due to the roll motion. Although the dynamic pressure measured at the barge corner was roughly discussed in the previous chapter, it is going to be examined in detail with the mean velocity and vorticity pattern. Note that only every other velocity vector in each row and column was plotted in the velocity figures, i.e., only one-quarter of the total measured velocity vectors are displayed in each figure. In Fig. 6.15, the first row is such that the water particle velocity of incident waves in the same FOV of the seaward side is drawn with a boundary of the barge to make it easy to compare with the velocity profiles of the wave interaction with the barge. The second row and the third row show the wave interaction with the fixed barge and the barge in roll motion, respectively.

6.7.1 Roll natural period wave (*T*=0.93 s)

The roll viscous damping (eddy making damping) effect to reduce the roll motion is caused by the flow separation due to the roll motion, which is most significant with the roll natural period wave. The variation of the flow pattern and the dynamic pressure affecting the roll viscous damping can be illustrated by the comparison with the fixed barge. The wave elevation at the seaward side of the case of roll motion was similar to that of the fixed barge (shown in Fig. 6.3 and Fig. 6.4). At phase 1 of the fixed barge, the positive vortex started to separate and the negative vortex was decaying at the wave crest of the seaward side. With the diffraction effect, the water particle near the free surface and away from the barge (left lower corner of figure) was close to zero velocity while the water particle of the incident wave was directed to the barge at a 45° degree. Although its velocity was small at the leeward side, the positive vortex began to be separated. As the result of roll motion, the water particles were faster than those of the fixed barge and the positive vortices were developed. The barge motion brought up the fluid under the barge of the seaward side. In contrast, the barge bottom on the leeward side pushed the water particle which turned around the corner and evolved the vortex at the side of barge. While the barge was inclining to the maximum roll in the negative direction, the induced dynamic pressures, which were P_{2D} to be negative and P_{3D} to be positive shown in Fig. 6.14, affected to reduce the roll motion. During the phases 2~4 of the fixed barge, the positive vortex was developing with the descending free surface at the seaward side. While the vortex was evolved under the barge corner, the induced dynamic pressure (P_{1D} and P_{2D}) increased to the maximum positive pressure on the side wall and bottom. The induced dynamic pressure (P_{1D} and P_{2D}) for the roll motion case, also, was on the increase as the positive vortex was decaying with the counter-clockwise roll motion of barge. It seems that the reason for the decaying of the positive vortex under the barge was the faster velocity of the barge corner than the motion of the free surface. Meanwhile, the negative vortex started and developed under the barge corner of the leeward side by the counter-clockwise roll motion and made the induced dynamic pressure (P_{3D}) decreased to the minimum negative pressure. It is shown that the difference of dynamic pressures between both sides in phases 2~4 can retard the roll motion. At phase 5, the clockwise (negative) vortex began to be separated by the counter-clockwise roll motion at the seaward side whereas the positive vortex was still evolved by the downward flow under the corner of the fixed barge. Even though the water particle of the incident wave ran away from the barge at the angle of about -225° degree, the diffraction effect made the upstream flow normal to the bottom which caused the induced dynamic pressure (P_{2D}) to be enhanced. By the counter- clockwise roll motion, however, the barge bottom pushed the water particle downward and the negative vortex was clearly developed at the seaward side of barge. The negative vortex of the leeward side, also, came into the larger vortex shape under the bottom due to the barge motion. As of phase 6, the water particle was diffracted to the upward flow from the trough of the incident wave. The negative vortex was fully developed until phase 8 at the side wall of the fixed barge and dissipated from phase 1. Then, the negative vortices of the barge in roll motion shrank up to phase 7, and the positive vortex was separated at both corners. With the counter-clockwise (positive) vortices due to the clockwise roll motion, the induced dynamic pressures was put on the bottom of both sides in the direction opposite to the roll motion, which is known as the damping effect.

Several features of flow and dynamic pressure patterns caused by the wave interaction with the rectangular barge at the natural period wave can be described. With the comparison between cases of fixed and free in roll motion, the vortex shedding at both corners was generated by the roll motion of the barge. The induced dynamic pressure (P_D) on the bottom near the corner, also, varied against the motion.

For the fixed case, the vortex was generated by the wave motion of wave. With the roll motion case, the vortex in the case of the fixed barge disappeared by the velocity of barge corner faster than that of the free surface.

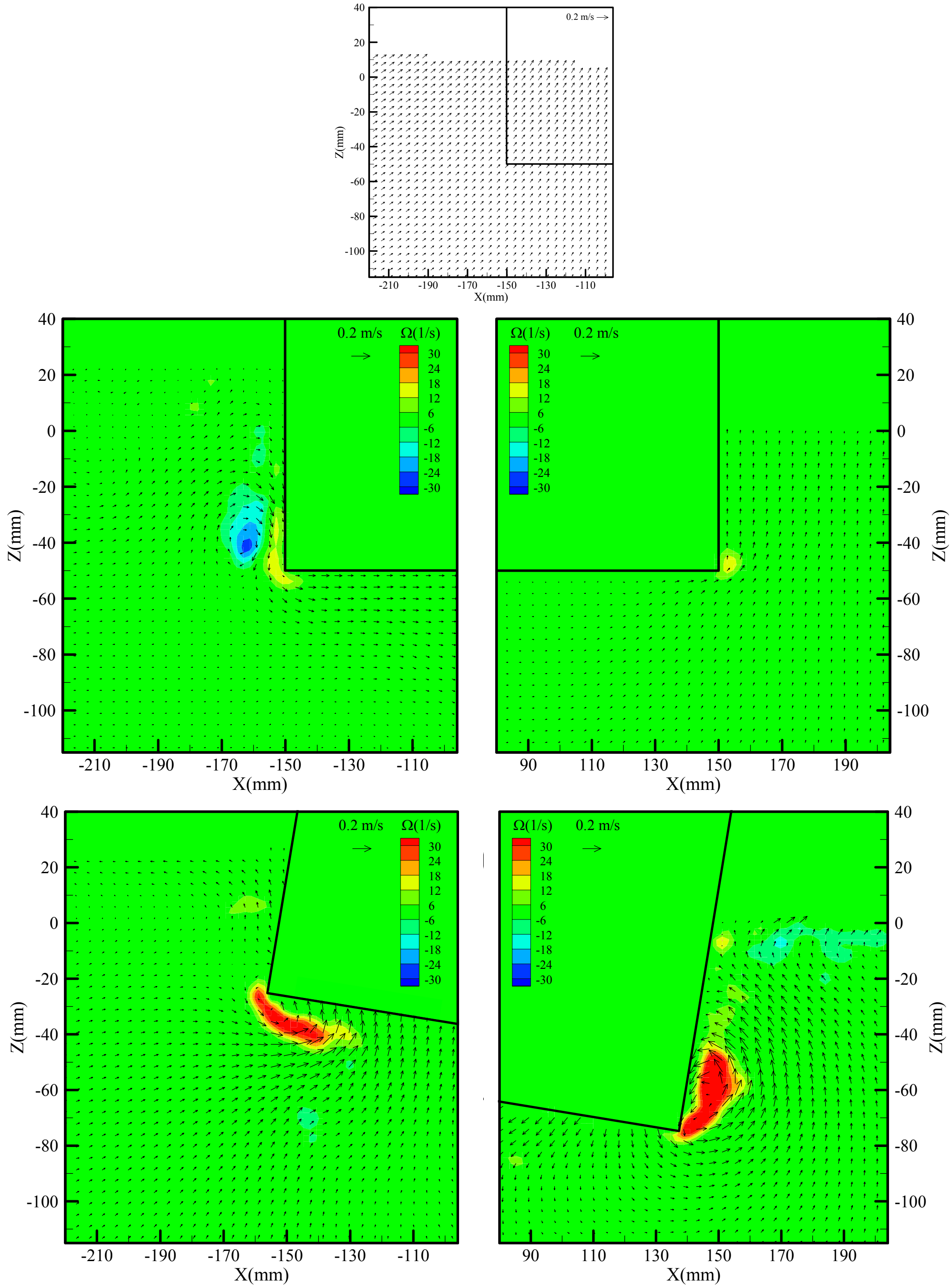

(a) Phase 1

Fig. 6.15 Mean velocity and vorticity of the incident wave (T=0.93 s and H=0.027m) without the barge (the first row), the fixed barge (the second row), and the barge in roll motion (the third row). Left column: seaward side; right column: leeward side.

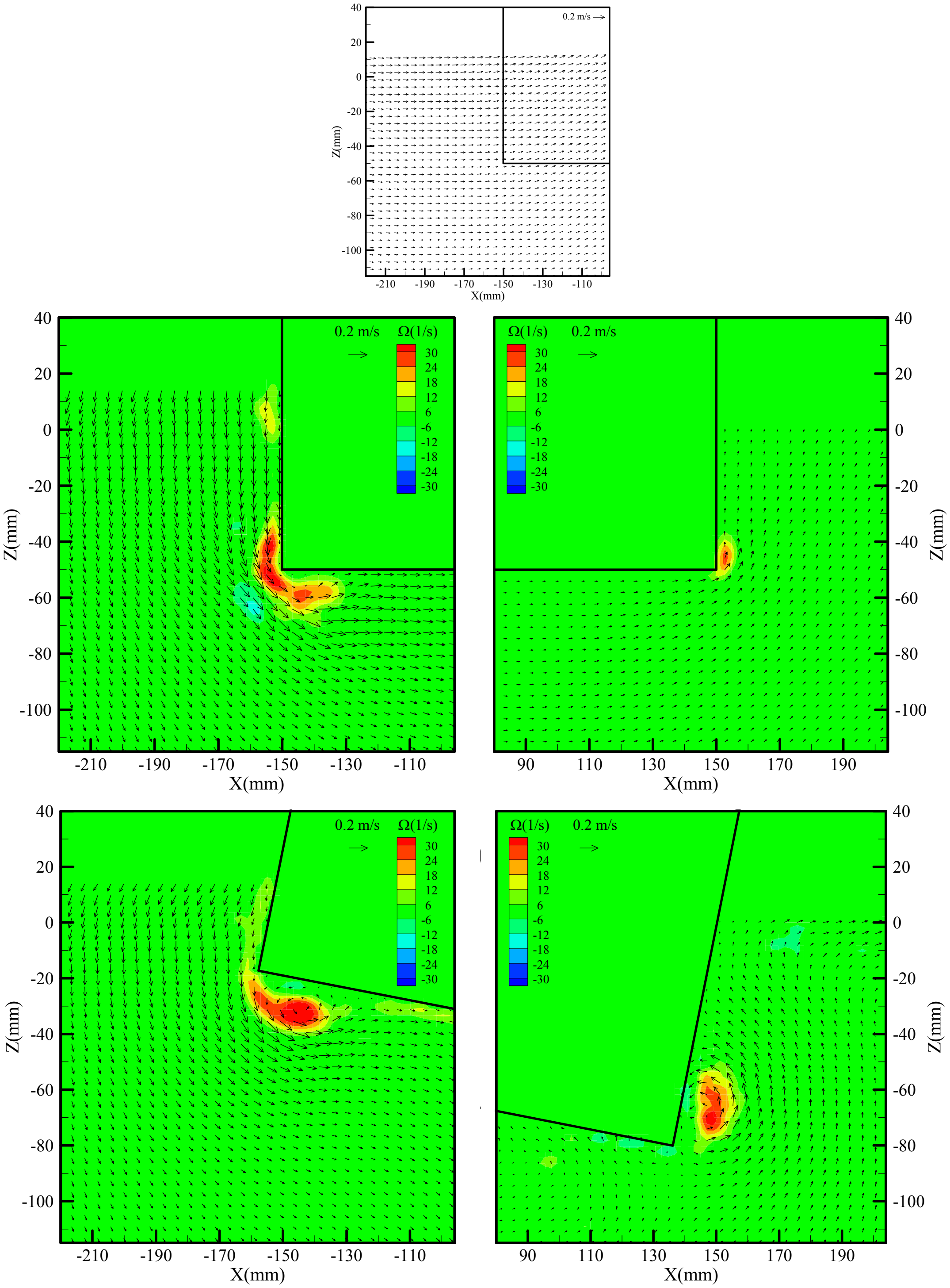

(b) Phase 2

Fig. 6.15 Continued

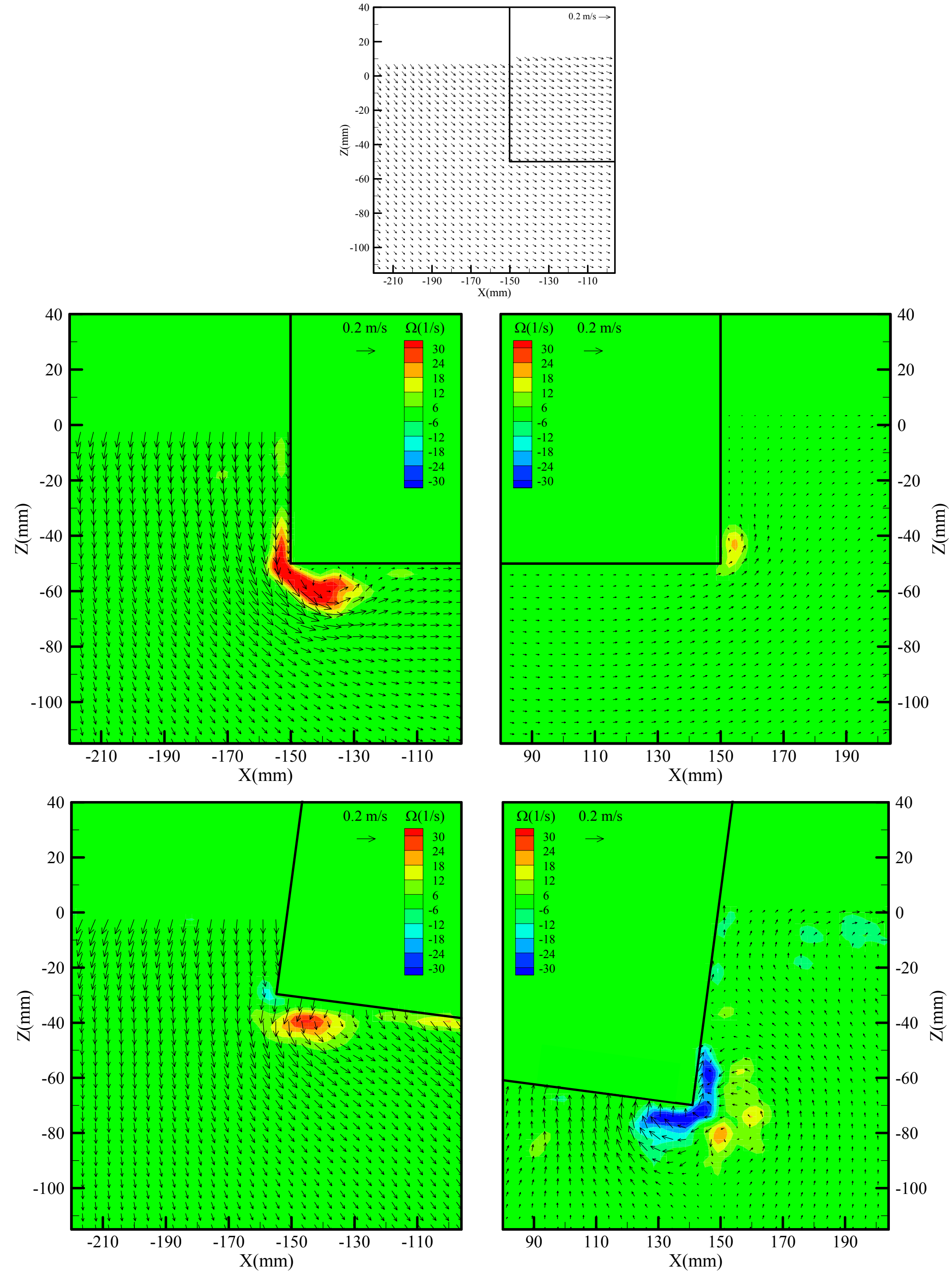

(c) Phase 3

Fig. 6.15 Continued

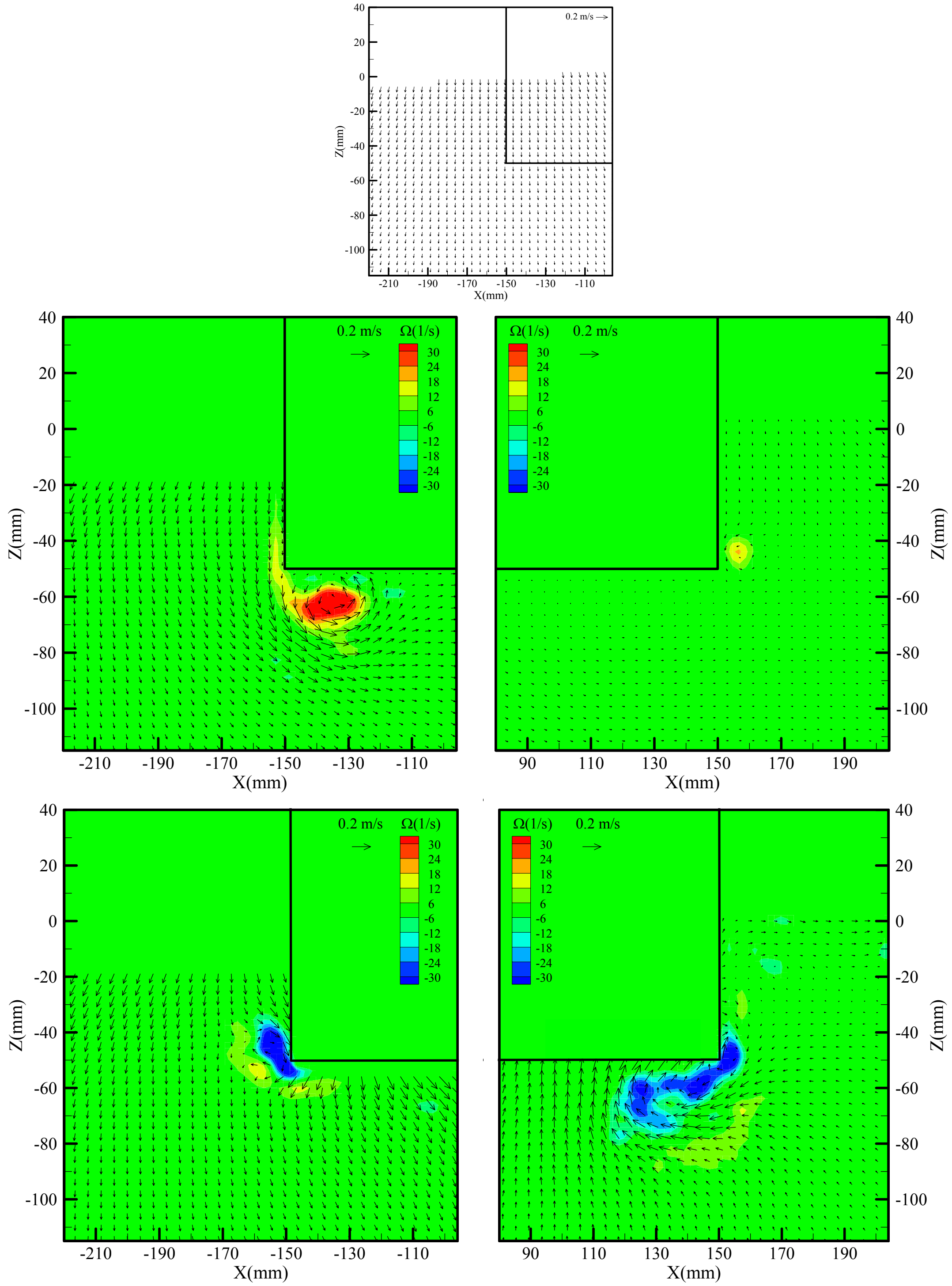

(d) Phase 4

Fig. 6.15 Continued

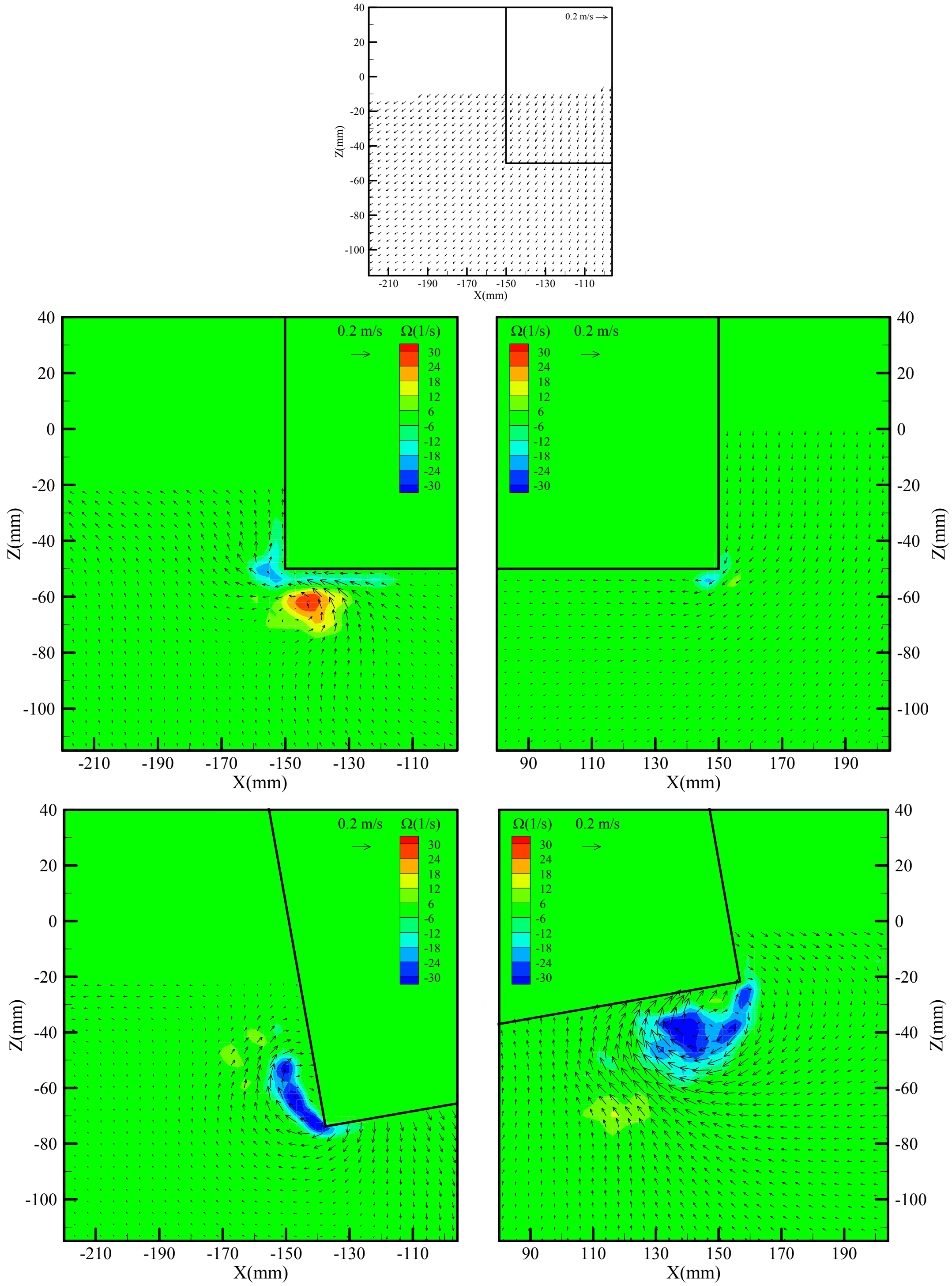

(e) Phase 5

Fig. 6.15 Continued

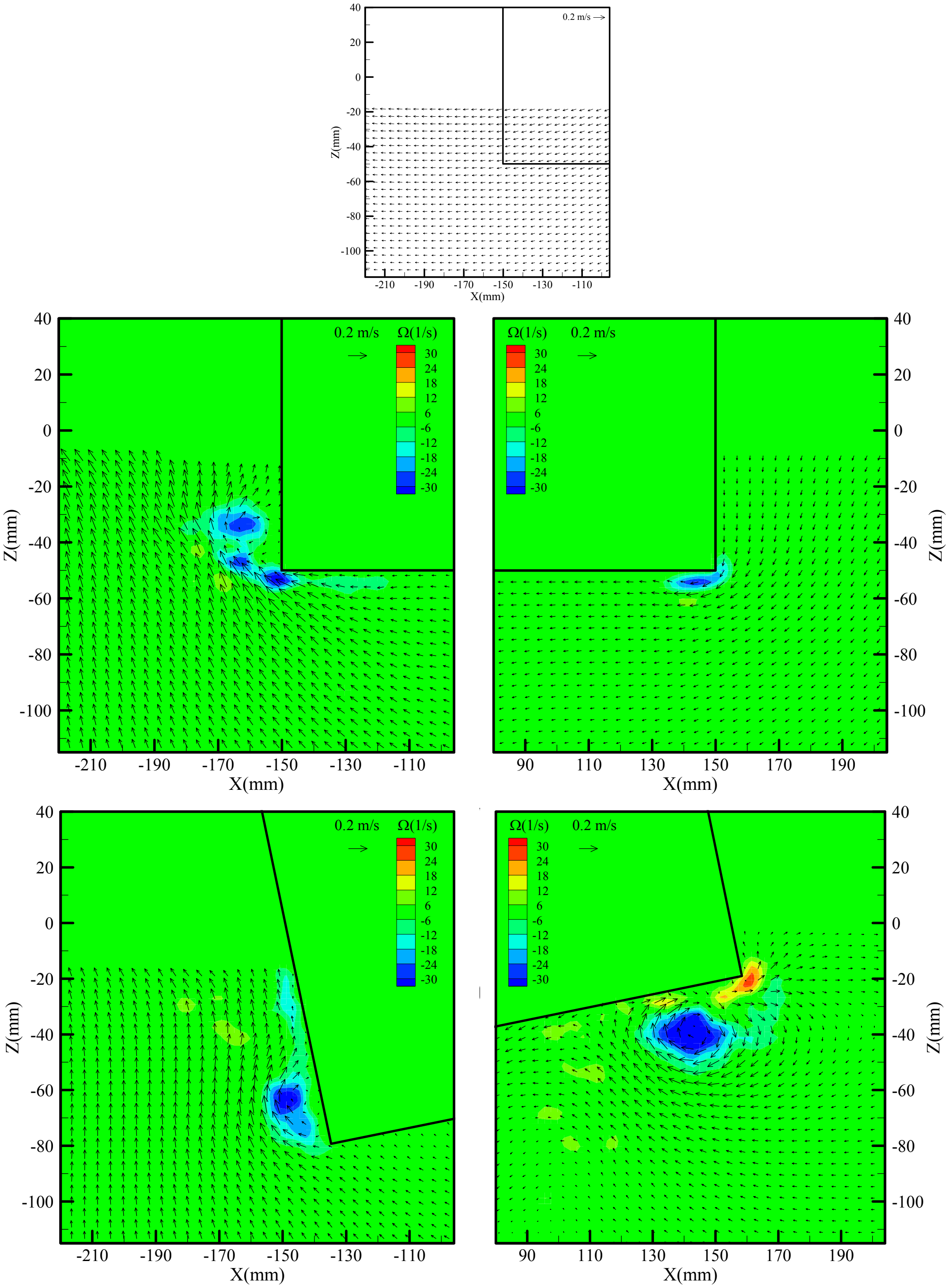

(f) Phase 6

Fig. 6.15 Continued

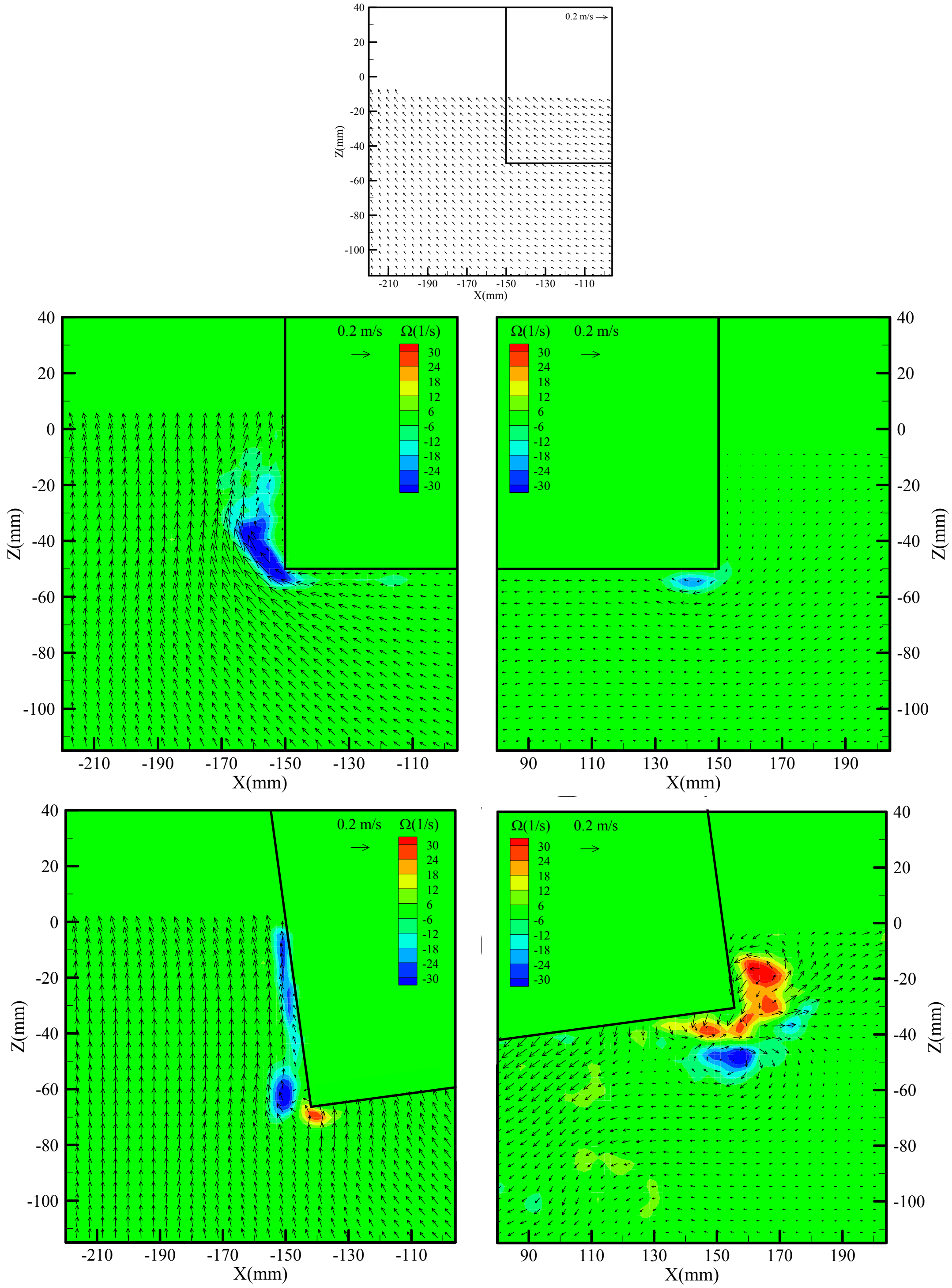

(g) Phase 7

Fig. 6.15 Continued

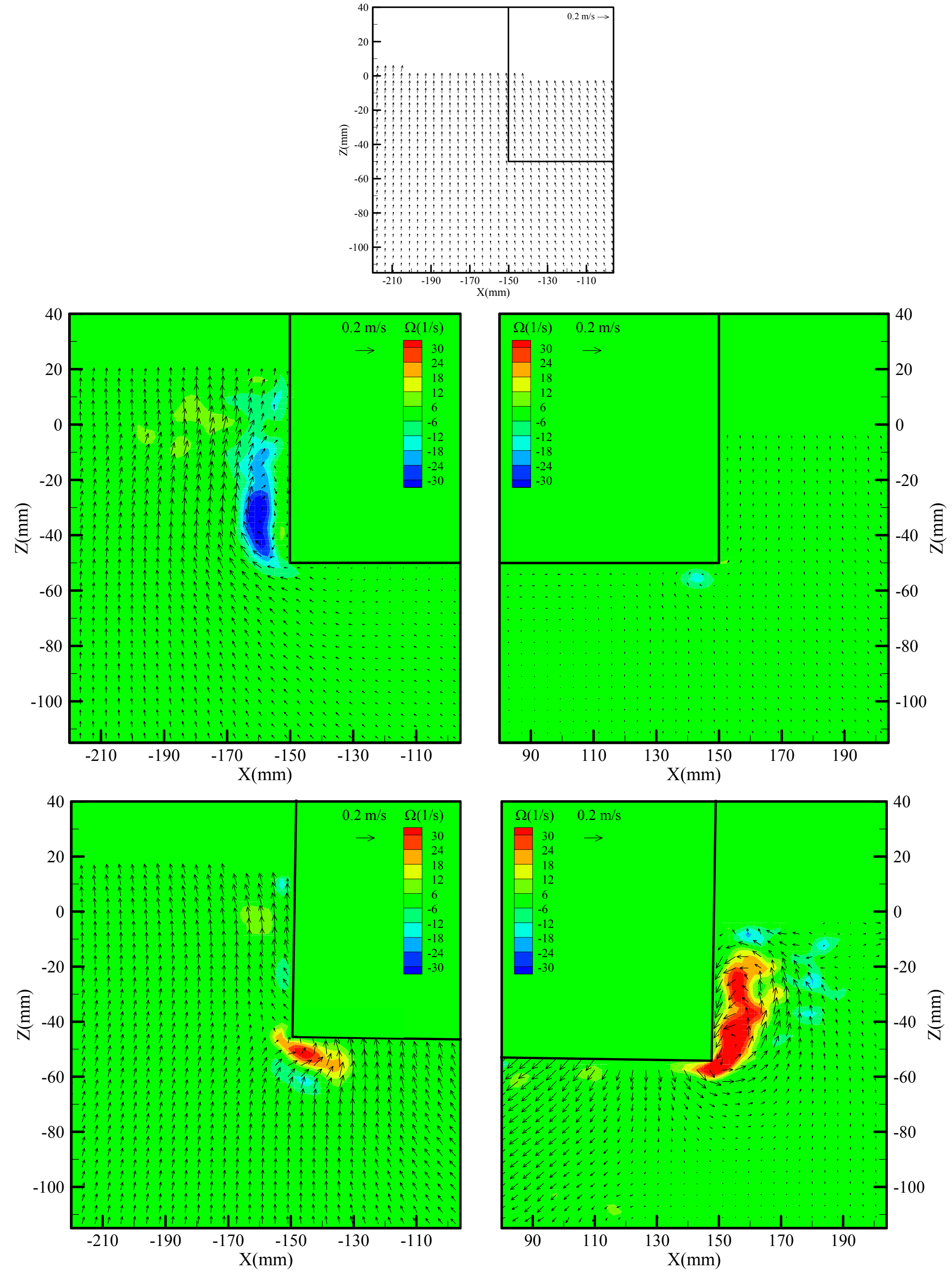

(h) Phase 8

Fig. 6.15 Continued

At the leeward side of the fixed barge, a little vortex was separated by the relatively small transmitted wave. However, the large vortex was generated by the roll motion at the leeward side. For the seaward side, it represented the vortex separated in the opposite direction of the fixed barge. These vortices of both sides are known as the roll viscous damping (eddy making damping) to reduce the roll motion at the wave of the roll natural period of the barge.

6.7.2 Longer period (T=1.2 s and 2.0 s) wave than roll natural period

The flow pattern with the roll motion interacted with the wave period (T=1.2 s) longer than the roll natural period was similar with that of the fixed case, which are represented in Fig. 6.16. The free surface of the seaward side had the highest level at phase 2, and the incident wave was the crest at phase 3. At phase 1, the barge started to be inclined into the counter-clockwise direction and the negative vortex was most developed. The remnant positive vortex remained under the free surface of the seaward side after separation from the corner. This vortex pattern was similar to the case of the fixed barge but opposite to that of the roll natural frequency wave. With the longer wave than the roll natural period, the vortex was, mainly, generated by the water motion instead of the barge motion. The vortices in the case of the fixed barge were developed ahead of that in the case of the roll motion. At the leeward side, the positive vortex was separated by the up-flow. However, the size and magnitude of the vortex was smaller than that of the fixed barge since the barge rolled in the same direction with the water motion. From phase 3 to phase 7, the free surface descended to the minimum of water lever faster than the rotation of the barge corner in the counter-clockwise direction. Then, the positive vortex was most developed under the barge at the seaward side by the water level down. At phase 5, the separation of the negative vortex was initiated at the corner of leeward side by the combination of the roll motion and water pattern and was increased by descending the water level, but the corner velocity decreased close to the maximum counter-clockwise roll angle during phases 6 and 7.

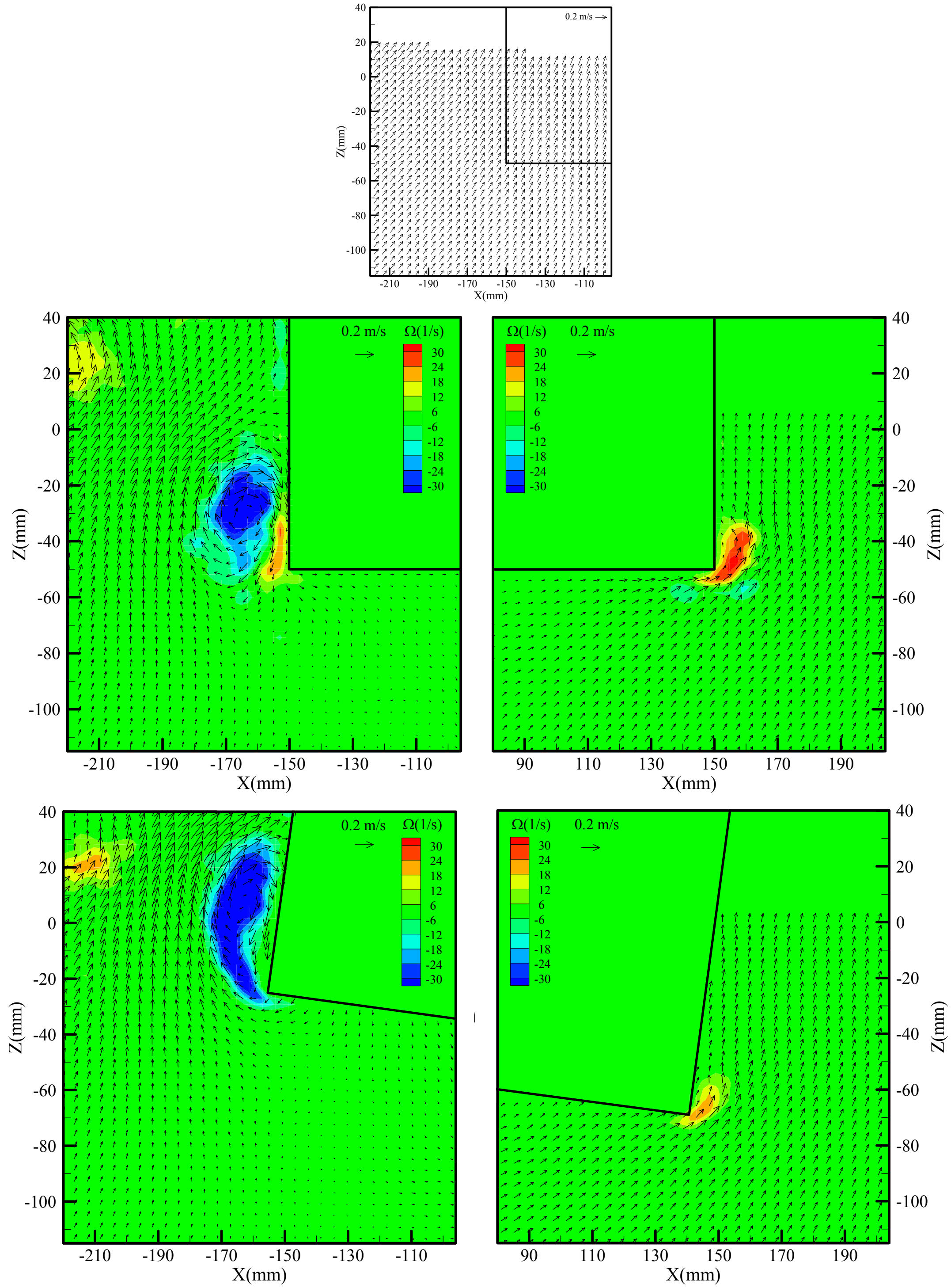

(a) Phase 1

Fig. 6.16 Mean velocity and vorticity (*T*=1.2 s) of the incident wave without the barge (the first row), the fixed barge (the second row), and the barge in roll motion (the third row). Left column: seaward side; right column: leeward side.

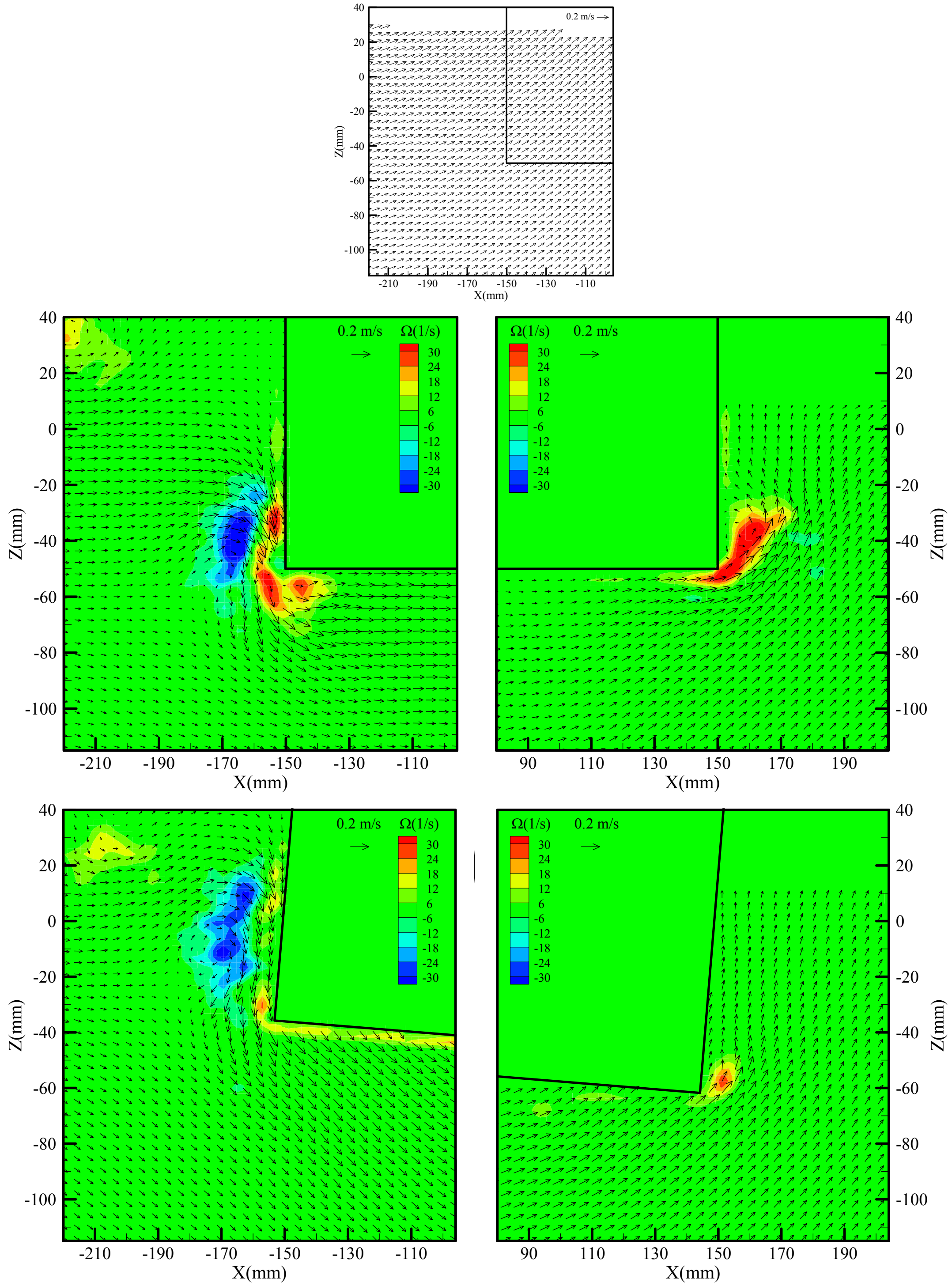

(b) Phase 2

Fig. 6.16 Continued

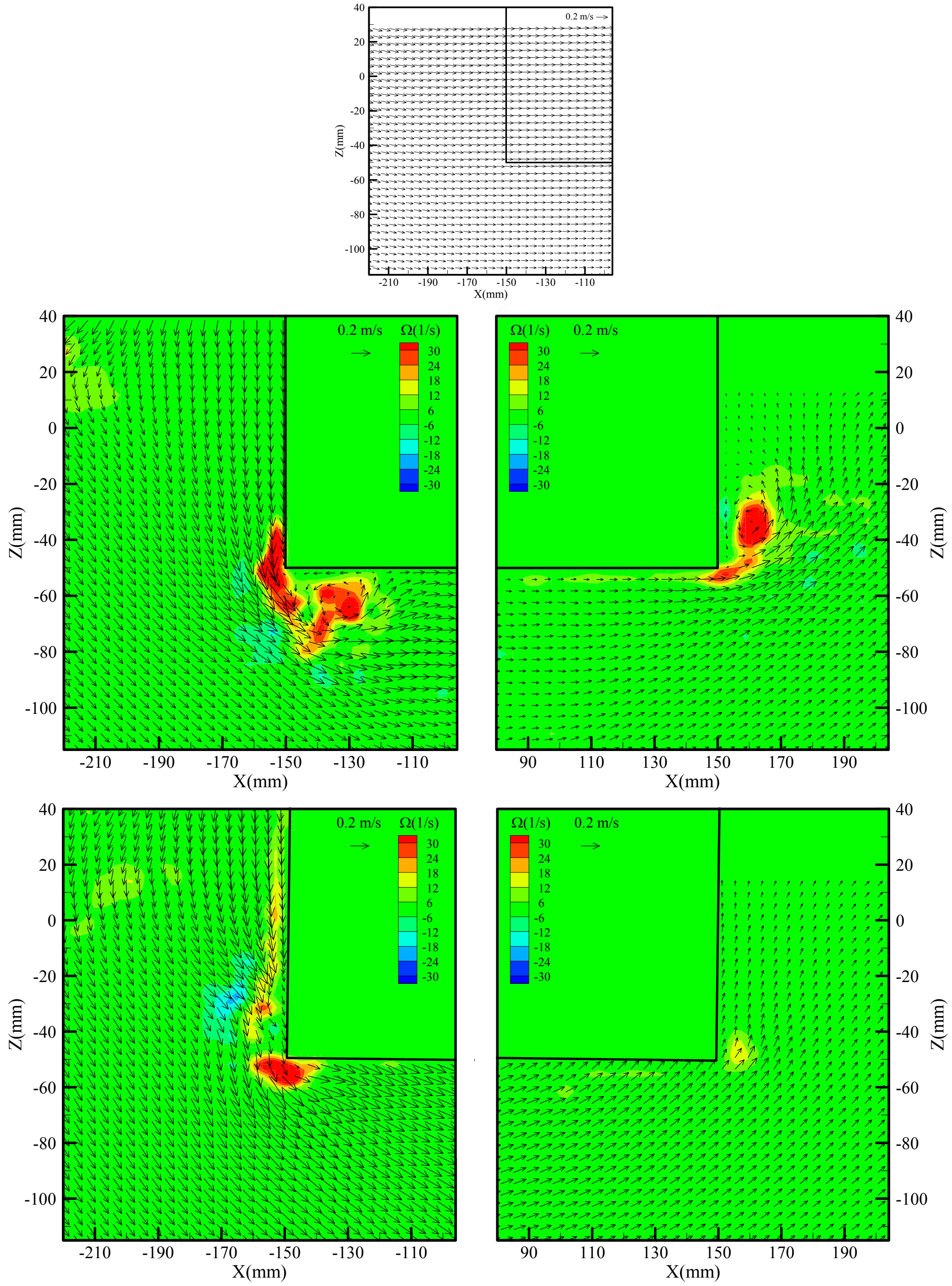

(c) Phase 3

Fig. 6.16 Continued

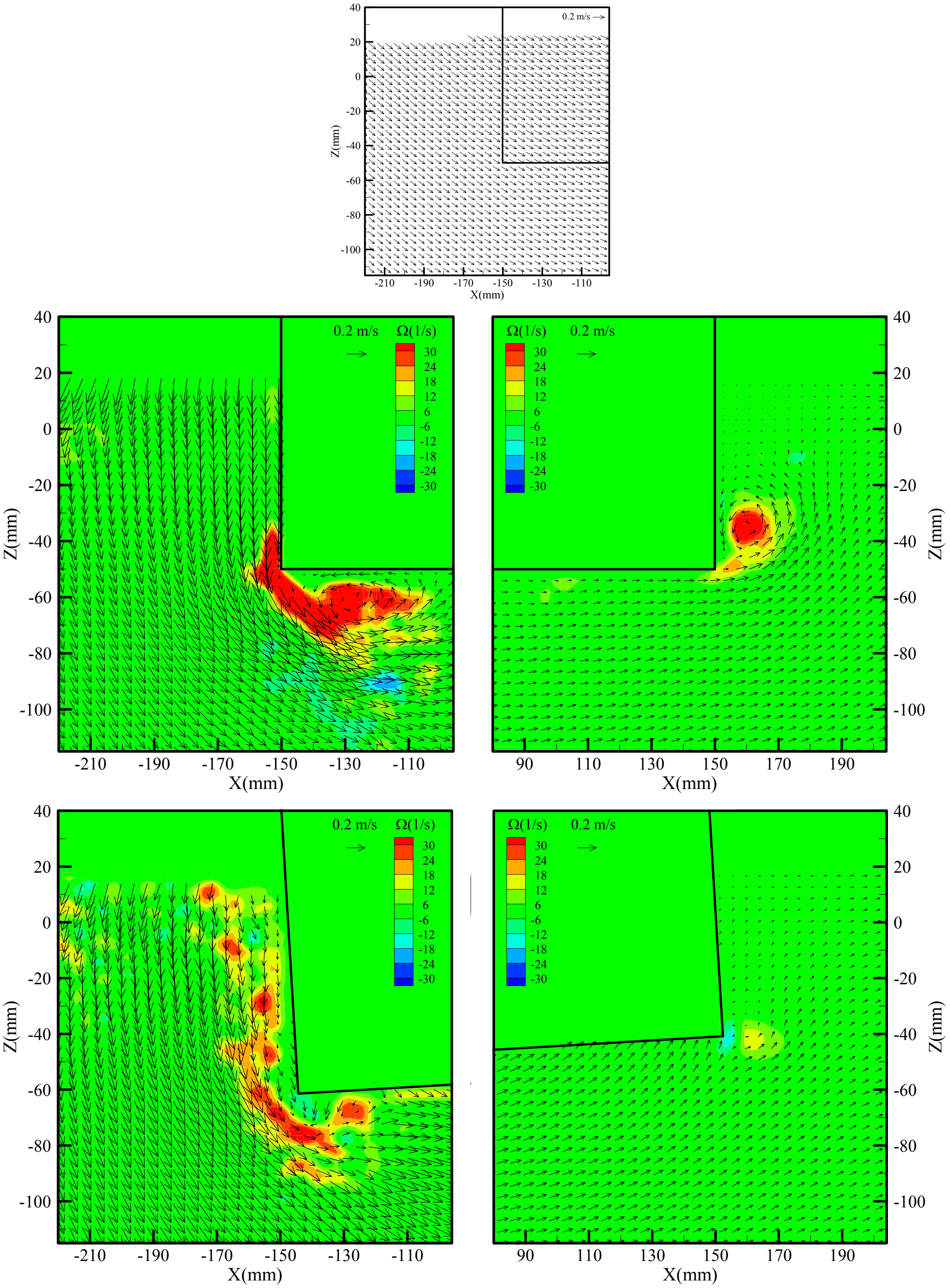

(d) Phase 4

Fig. 6.16 Continued

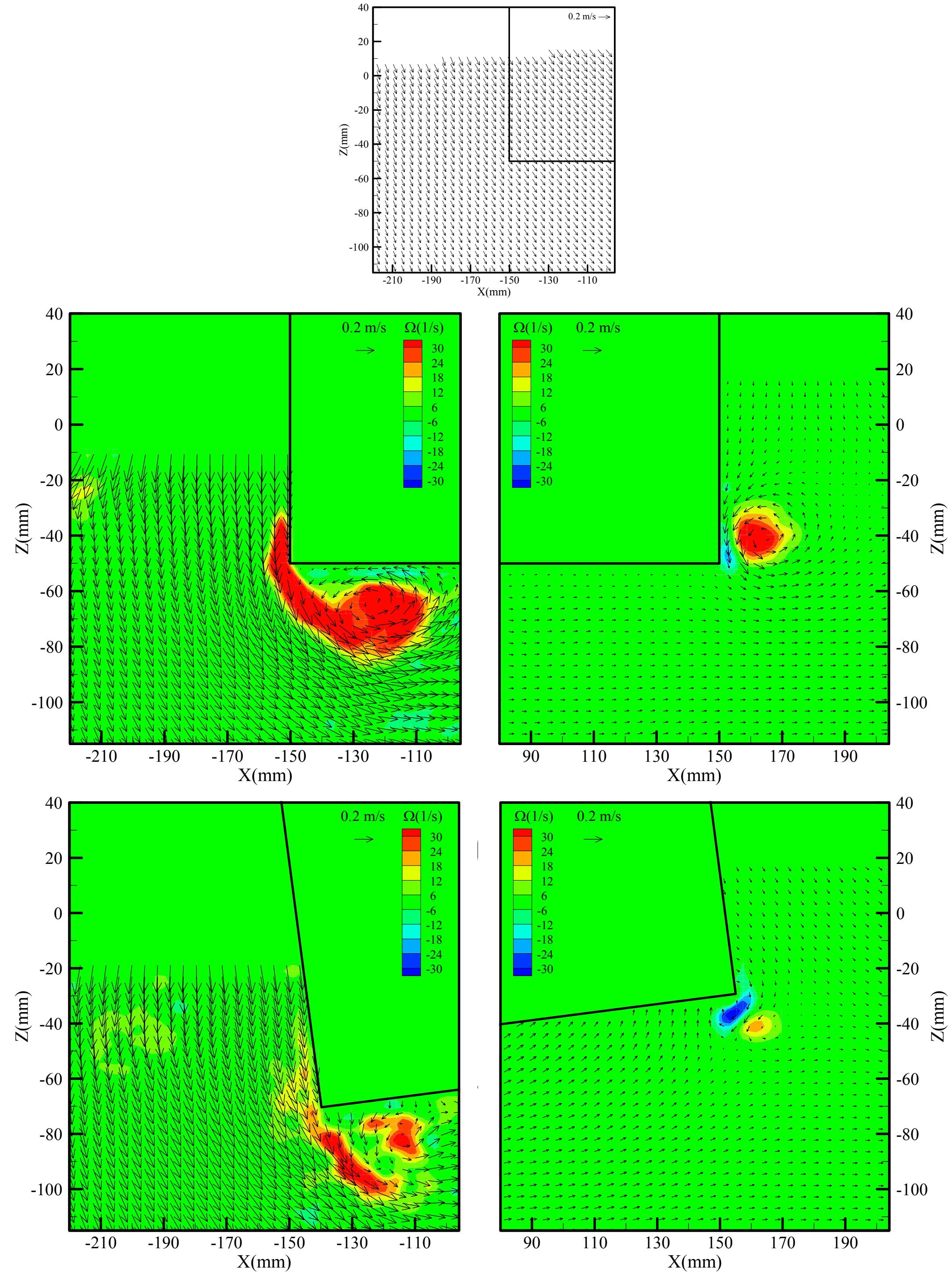

(e) Phase 5

Fig. 6.16 Continued

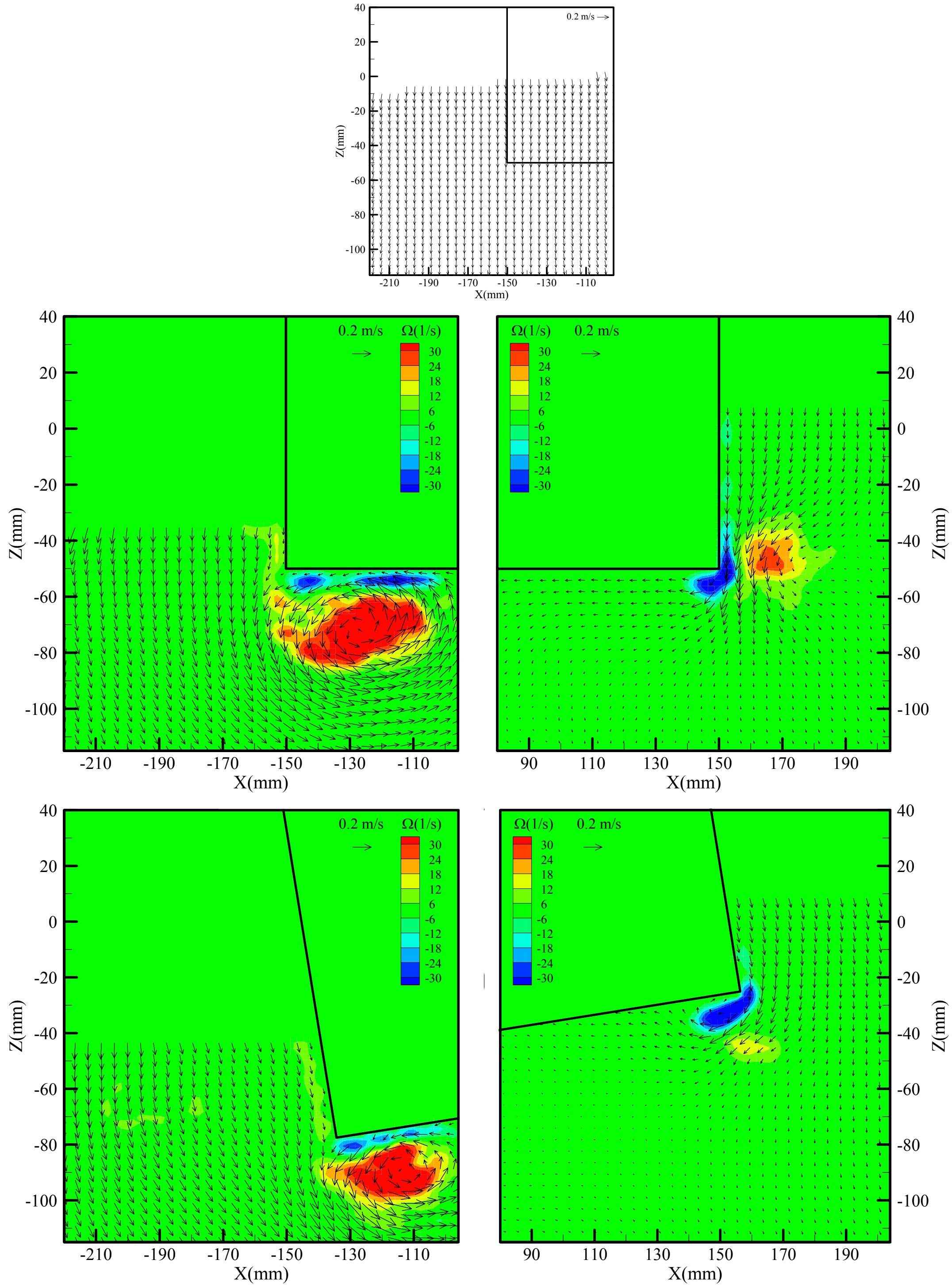

(f) Phase 6

Fig. 6.16 Continued

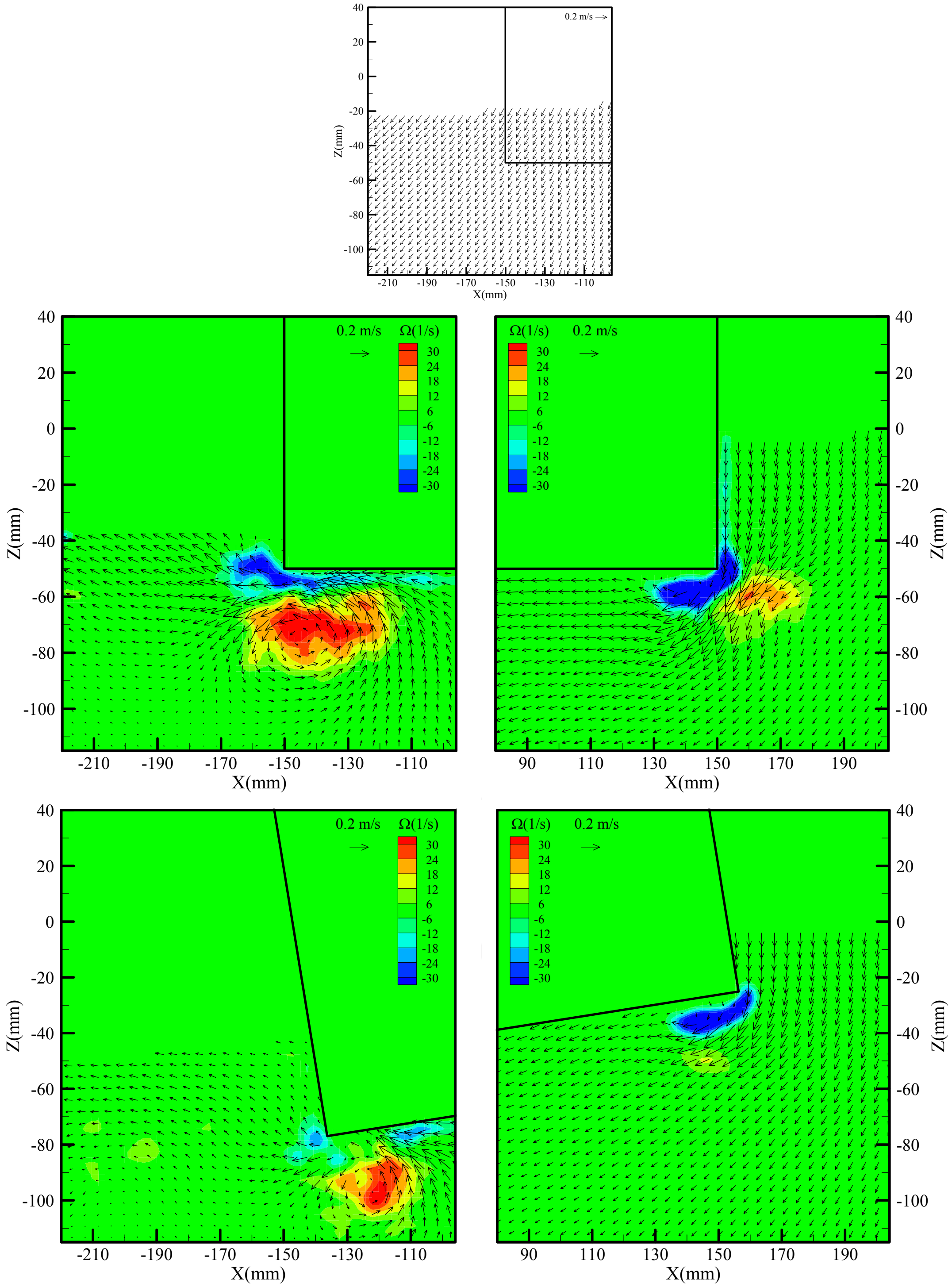

(g) Phase 7

Fig. 6.16 Continued

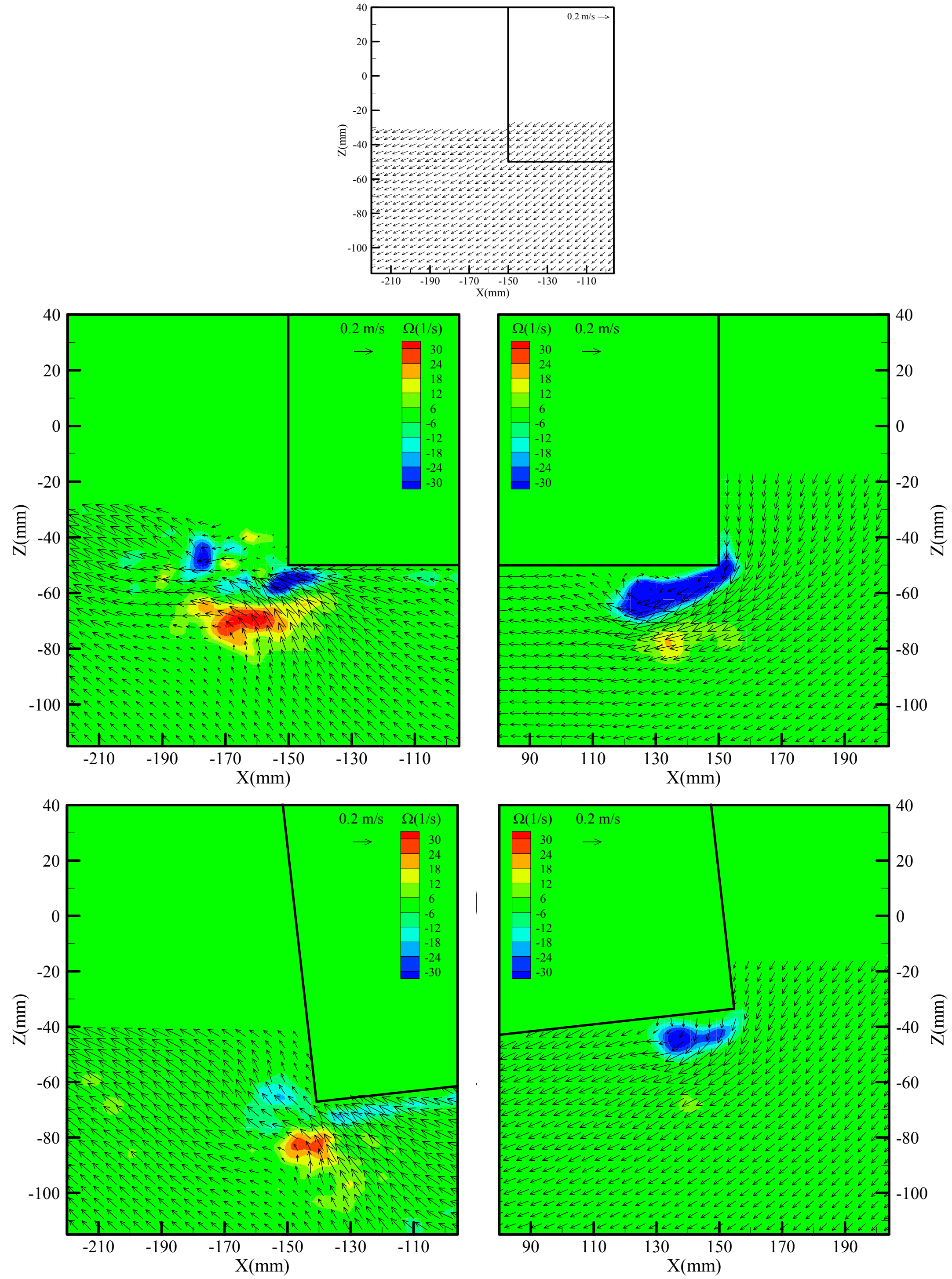

(h) Phase 8

Fig. 6.16 Continued

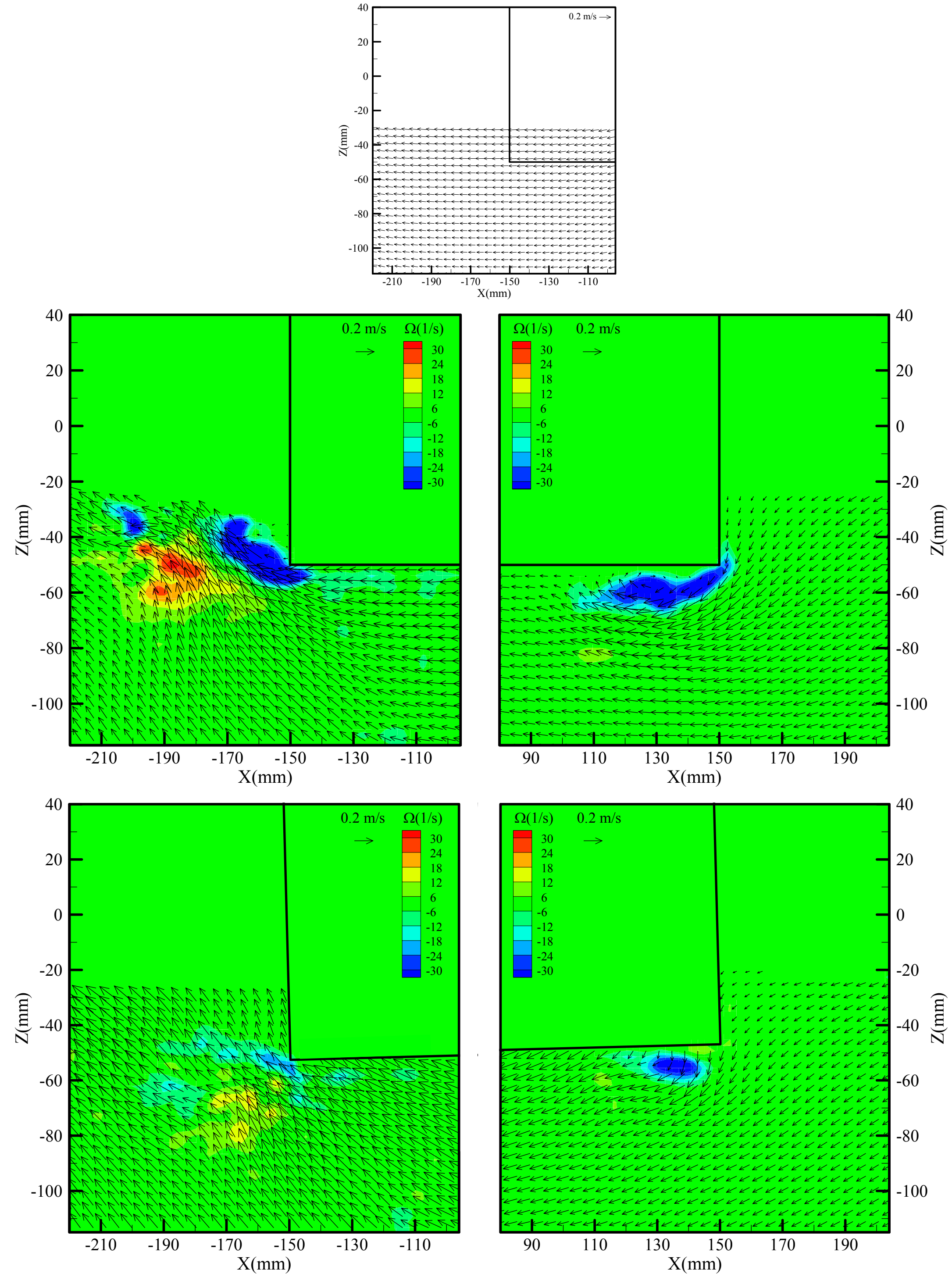

(i) Phase 9

Fig. 6.16 Continued

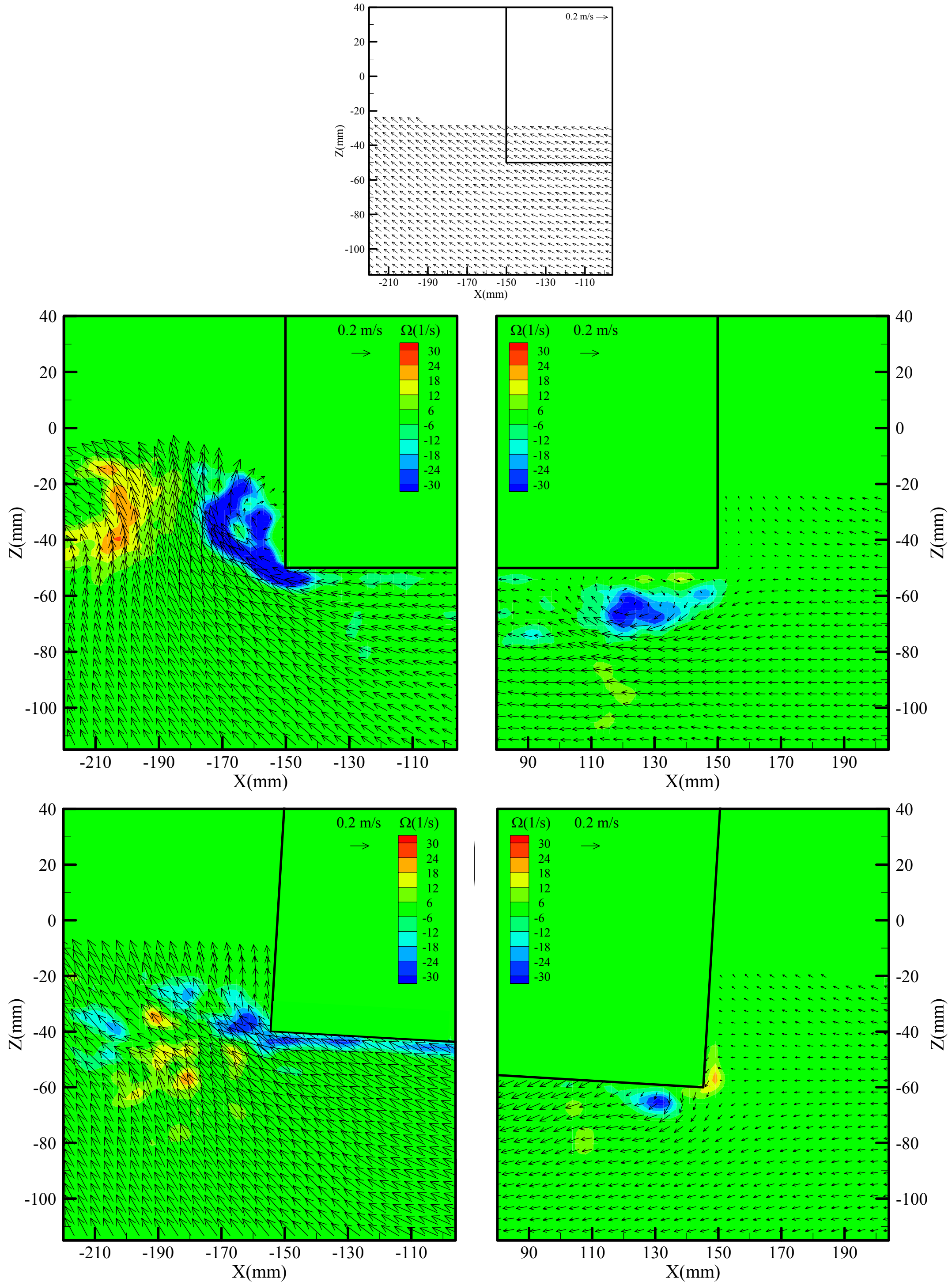

(j) Phase 10

Fig. 6.16 Continued

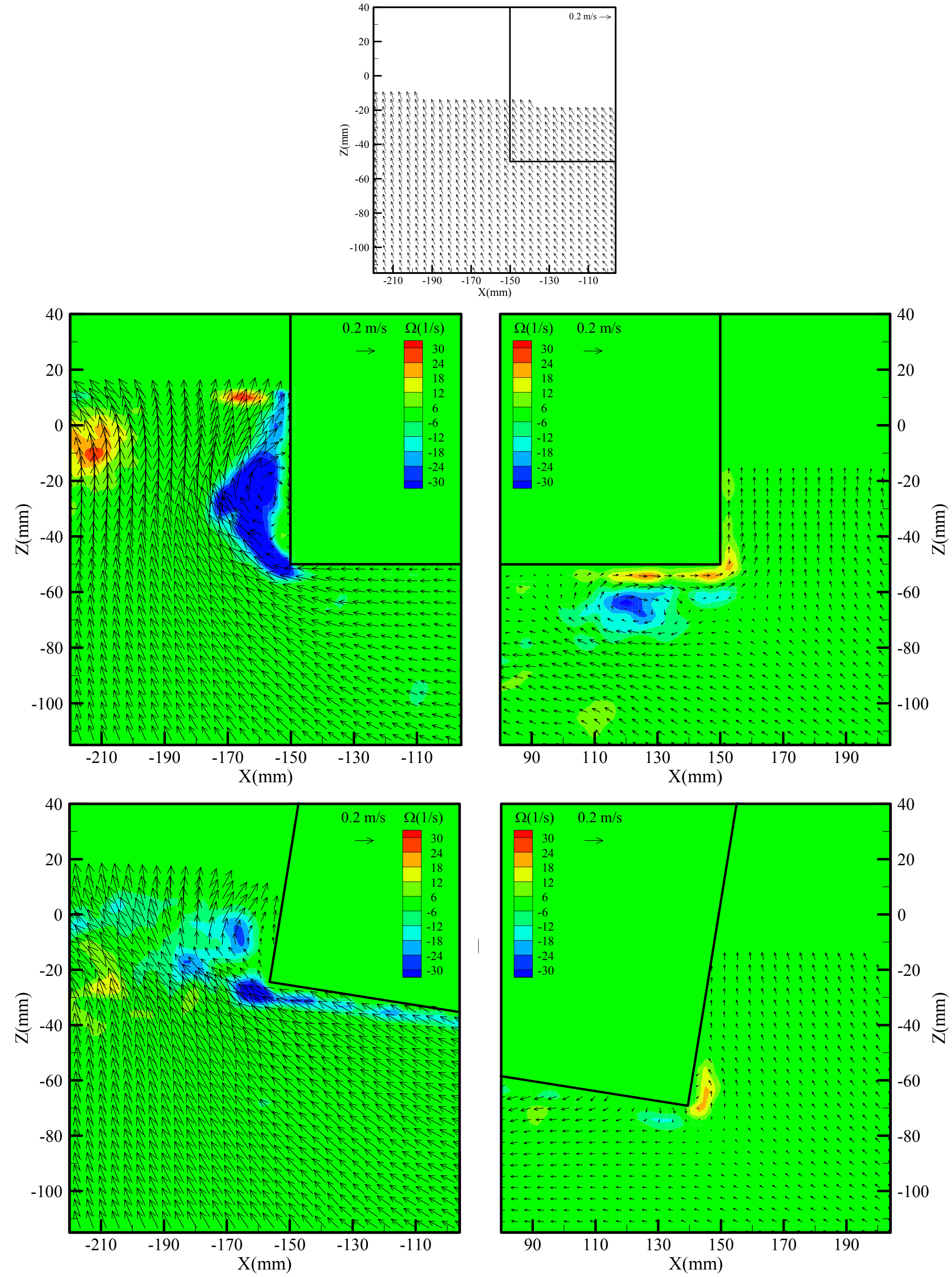

(k) Phase 11

Fig. 6.16 Continued

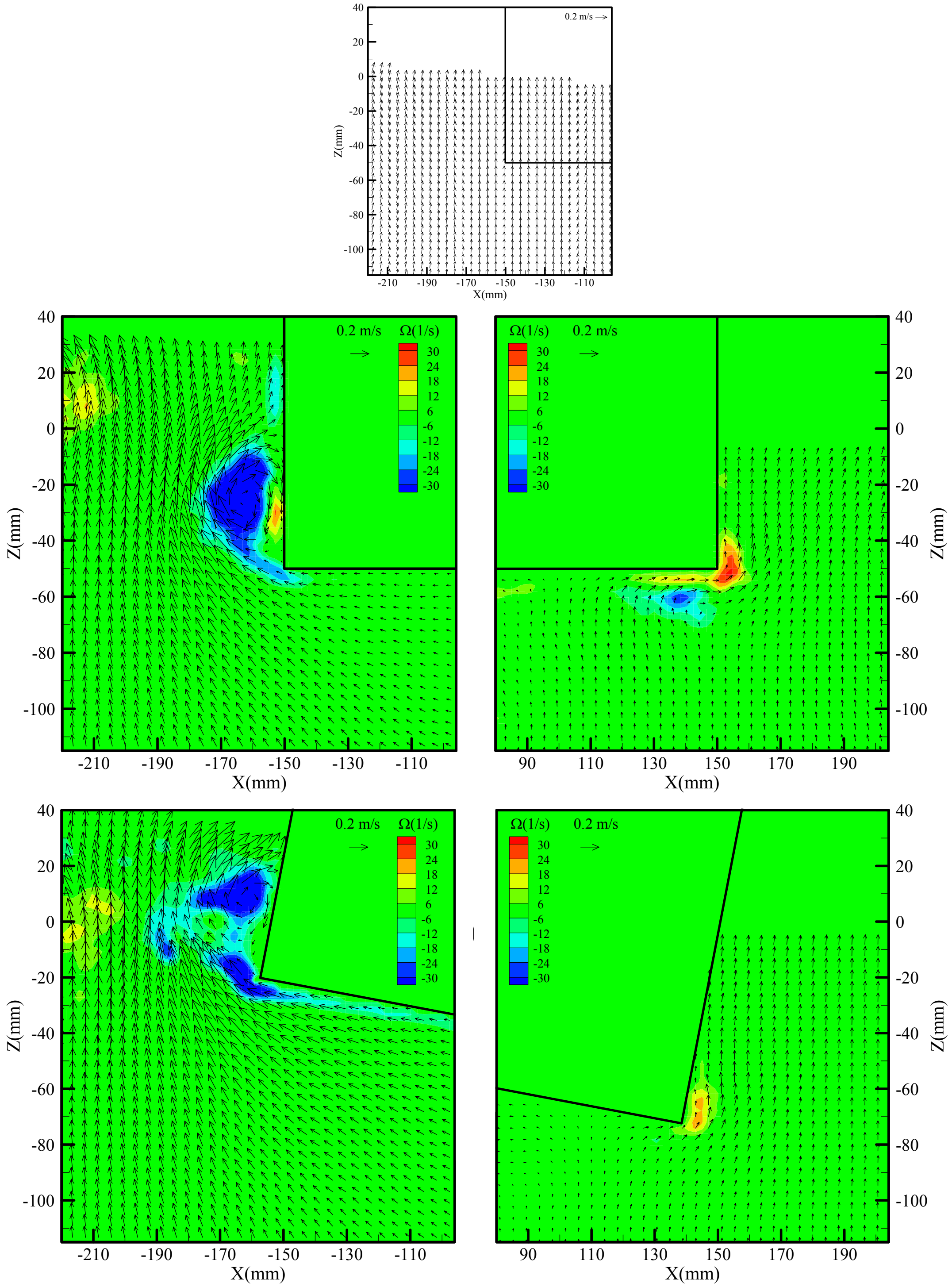

(l) Phase 12

Fig. 6.16 Continued

While the negative vortex increased at the leeward side corner of the fixed barge, the negative vorticity of the leeward side with roll motion was shrunken. Because the roll motion turned to the clockwise direction from the maximum inclined positive angle, the relative velocity between the water and barge corner was decreased and the vorticity due to the water motion was reduced by the motion. With the free surface rising (phase 8), the positive vortex was dissipating away from the barge corner and the negative vortex began to be separated. The induced dynamic pressures ($P2_D$ and $P3_D$) on the bottom were varied in very similar phase and magnitude by the roll motion, while they were out of phase in the case of the fixed barge. Therefore, the induced dynamic pressures were balanced on the bottom at both corners with the roll motion. This variation of induced dynamic pressure contrasted with the case of roll natural period can stand for little damping effect due to the flow kinematics and viscosity at the longer period wave than the roll natural period. The relative water particle velocity to the barge corners in case of roll motion was slower than that of the fixed barge since the barge rolled in the same direction with flow. At both sides, consequently, the size and level of the vortex with the roll motion was smaller and lower than those of the fixed barge.

Wave period (T=2.0 s) further from the roll natural period was also tested (shown in Fig. 6.17) to see the flow pattern at the longer wave period. As mentioned in the chapter 6.4, the barge had the double frequency roll motion of the double frequency at T=2.0 s wave since the restoring moment of double frequency came from the condition fixed in heave and sway motion. For the reason that the transmission coefficient (K_T=0.96) was relatively high, the incident wave was more transmitted through the barge than that of shorter waves, and the change of water level had a more significant effect on the flow pattern and induced dynamic pressure at the leeward side. The flow pattern was less affected by the roll motion than shorter waves and more similar to that of the case fixed barge. At phases 1 and 2 of the fixed barge, the vertically upward flow of incident wave was divided into two horizontal flows heading to both corners which helped to generate vortices after the separation at corners. The barge was the nearly mean position in the clockwise roll motion in phase 1. For phases 1~4, as the corner of the seaward side was rotated up with the same direction with the free surface, the corner of the leeward side was inclined in the opposite direction with the water level up. Nevertheless, the shape of vortices was similar to those of the fixed barge since the amplitude of the roll motion was relatively small against the change of water level. The positive vortex was separated at the corner of the seaward side from phase 3 and the barge started to be inclined in the counterclockwise direction. The magnitude and size of the positive vorticity under the barge were smaller than those of the fixed barge until phase 9 due to the decrease of the relative velocity of the barge. With the counter-clockwise roll motion, the negative vortex at the leeward side was separated ahead the fixed condition at phase 7. However, its negative vortex was much smaller than the fixed barge until phase 12. While the negative vorticity was decaying under the leeward side of the fixed barge, the negative vorticity lasted up to phase 16 due to the roll motion. Although the vortex was generated by the combination of the water flow and the roll motion in the longer period wave than the roll natural period, the water flow of wave was the more dominant effect on the generation of vortex at both sides. The induced dynamic pressures at barge corners were not changed as much as other period waves. Their amplitude was decreased at the seaward side and similar at the leeward side. The variation of the induced dynamic pressure at the seaward side in roll motion became in phase and similar amplitude like the T=0.93 s and 1.2 s waves. However, the induced dynamic pressures of the leeward side in roll motion kept in similar pattern with those of the fixed barge while their magnitude and phase were changed with the roll motion. Also, the induced dynamic pressures in roll motion were comparable between both sides. This relation of the induced dynamic pressure between both sides was also illustrated at the T=1.2 s. For the roll natural period (T_N=0.93) wave, in contrast, the induced dynamic pressures of both sides were varied out of phase. Namely, the differences in the magnitude and phase of induced dynamic pressure had an effect on the roll motion. It is noteworthy that the induced dynamic pressure, which was out of phase between $P2_D$ and $P3_D$, pulled back the bottom of both corners. These trends of induced dynamic pressure look like the viscous damping effect due to the flow separation.

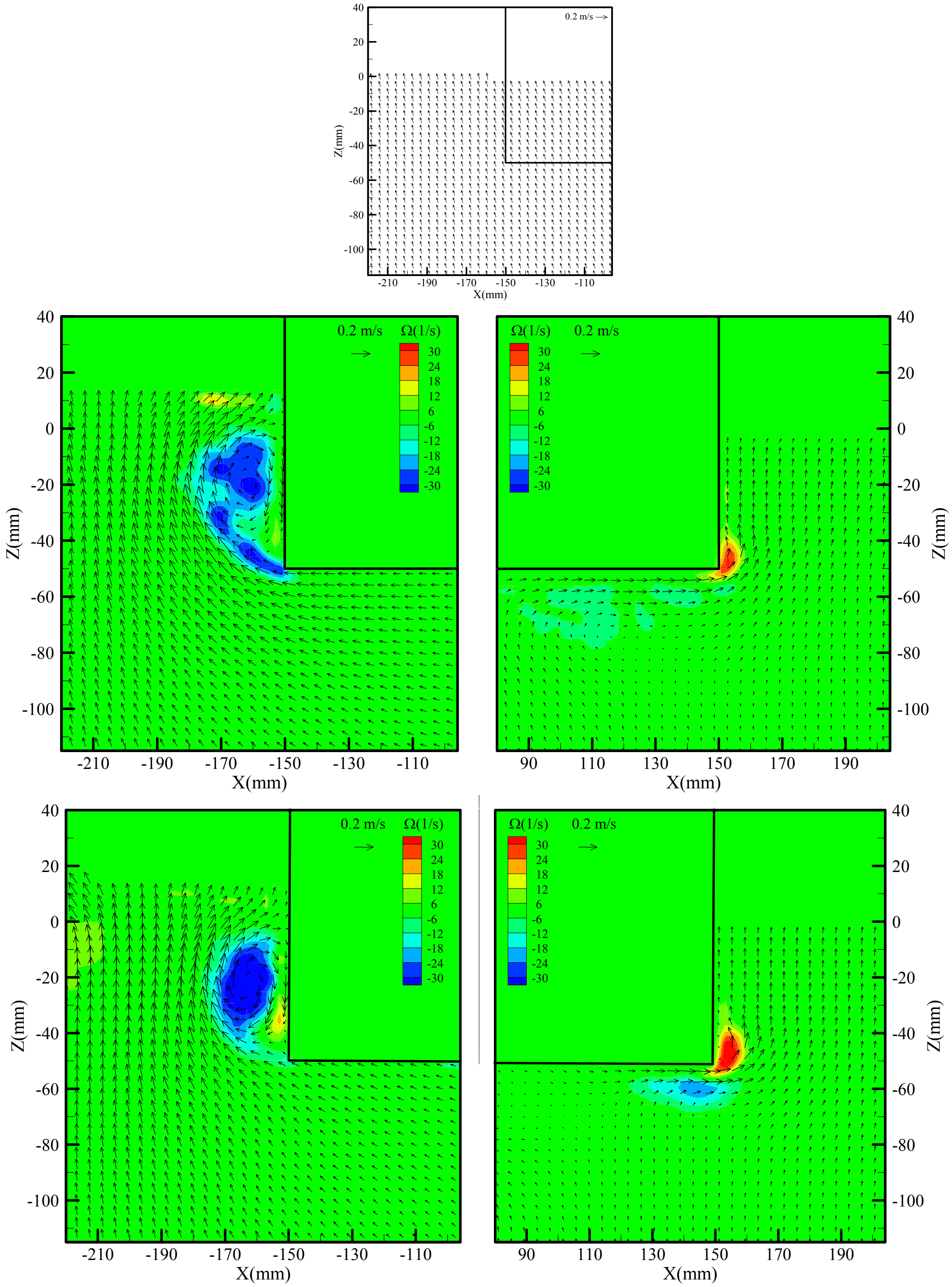

(a) Phase 1

Fig. 6.17 Mean velocity and vorticity (T=2.0 s) of the incident wave without the barge (the first row), the fixed barge (the second row), and the barge in roll motion (the third row). Left column: seaward side; right column: leeward side.

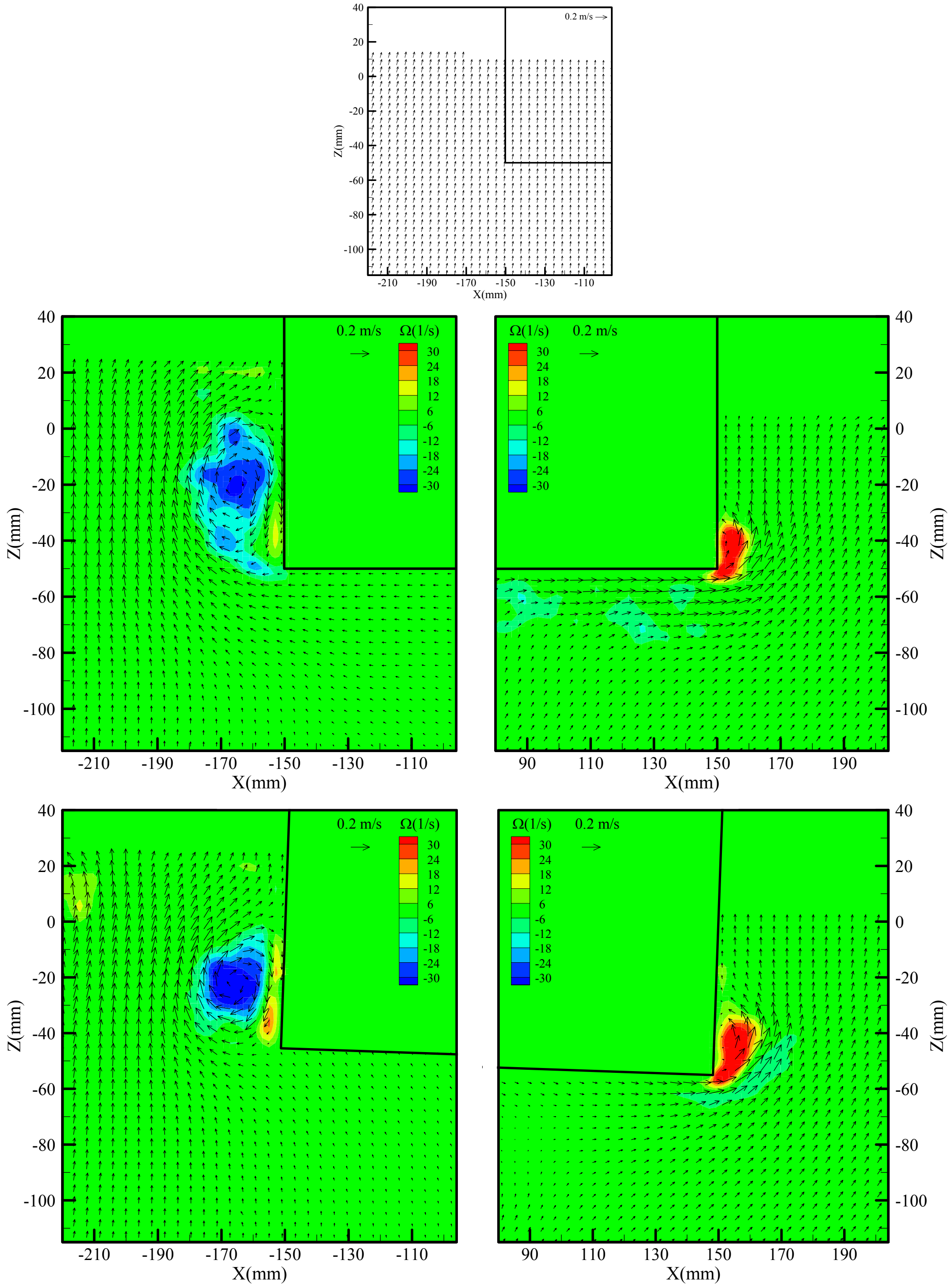

(b) Phase 2

Fig. 6.17 Continued

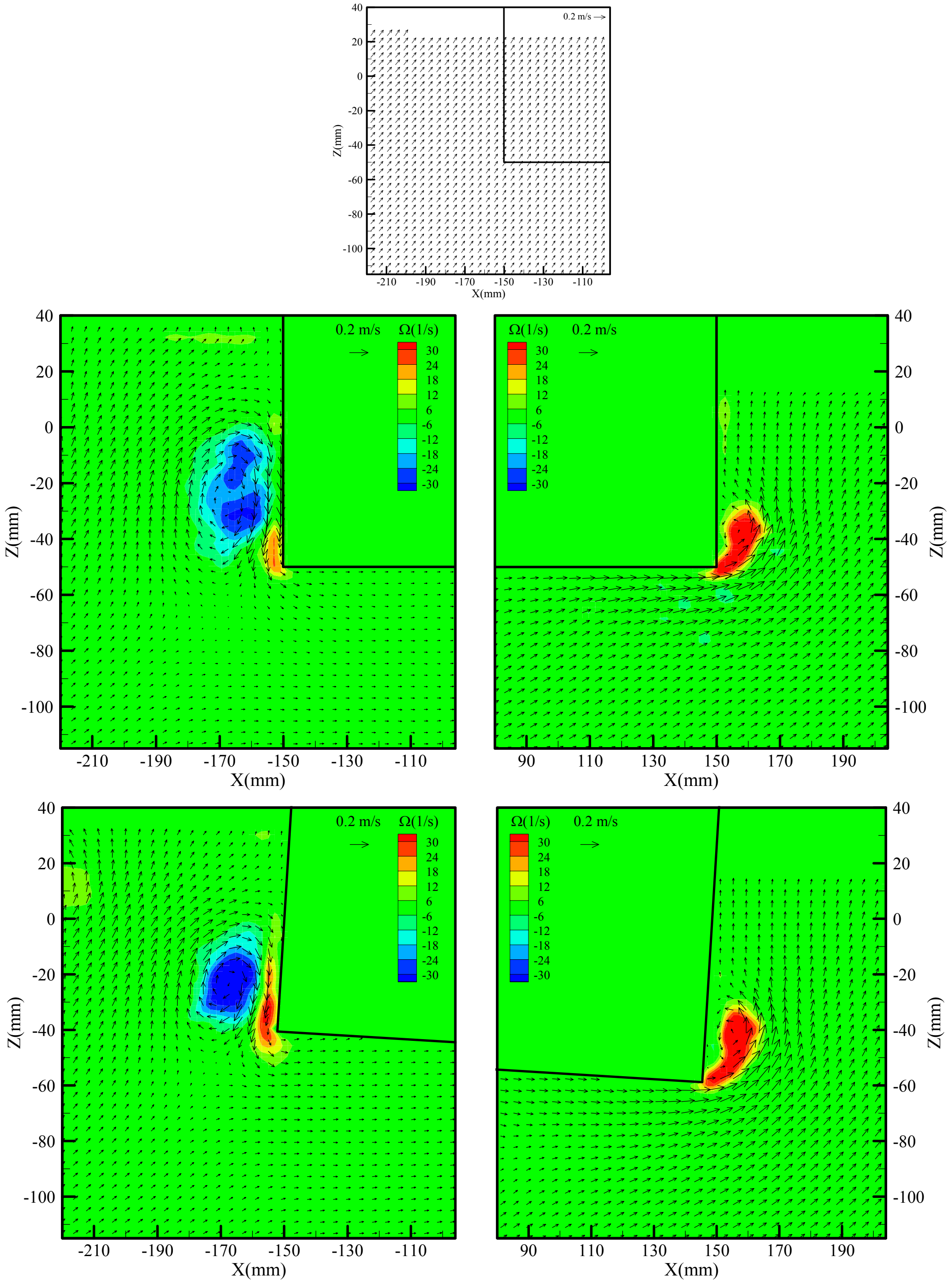

(c) Phase 3

Fig. 6.17 Continued

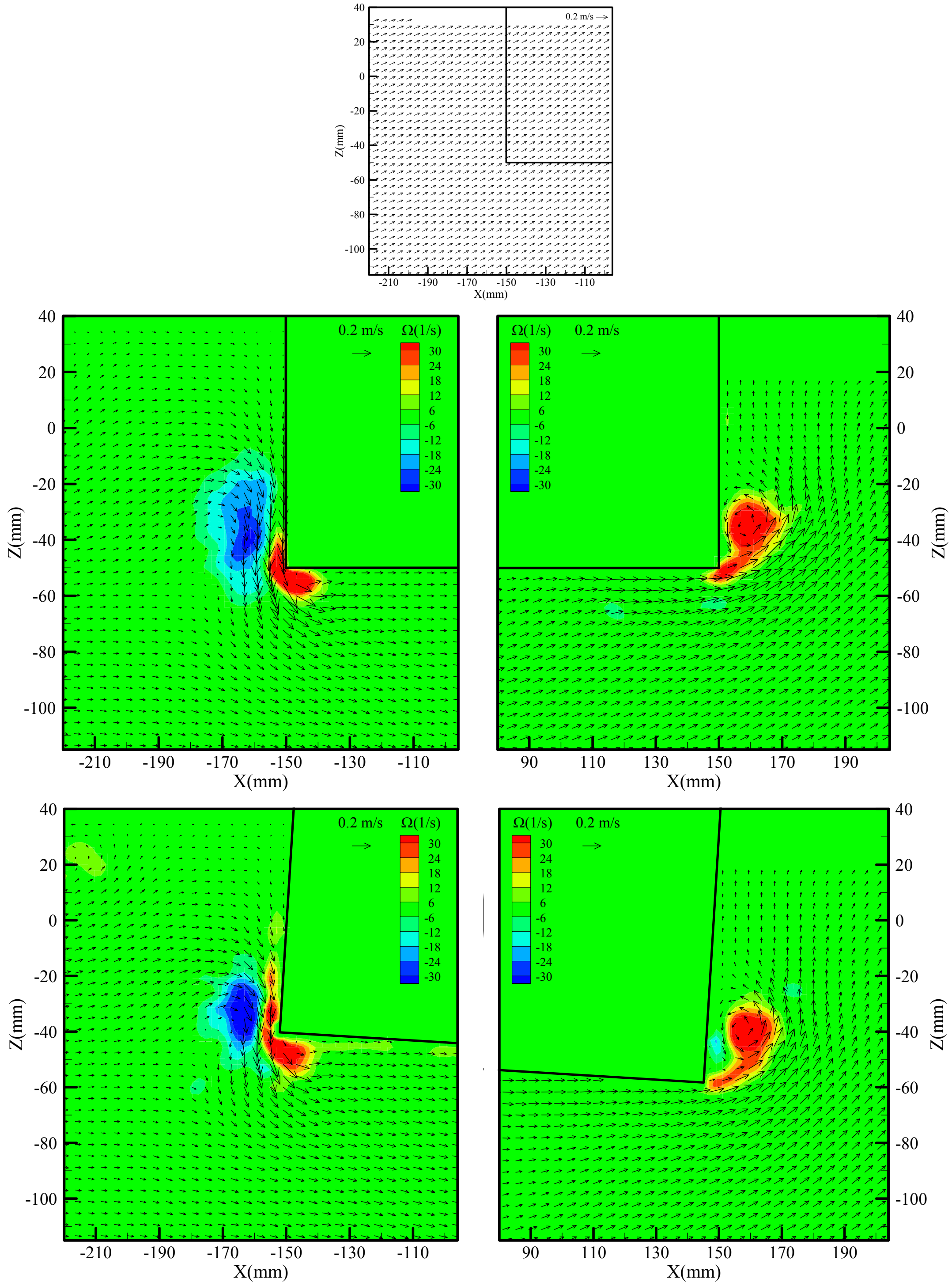

(d) Phase 4

Fig. 6.17 Continued

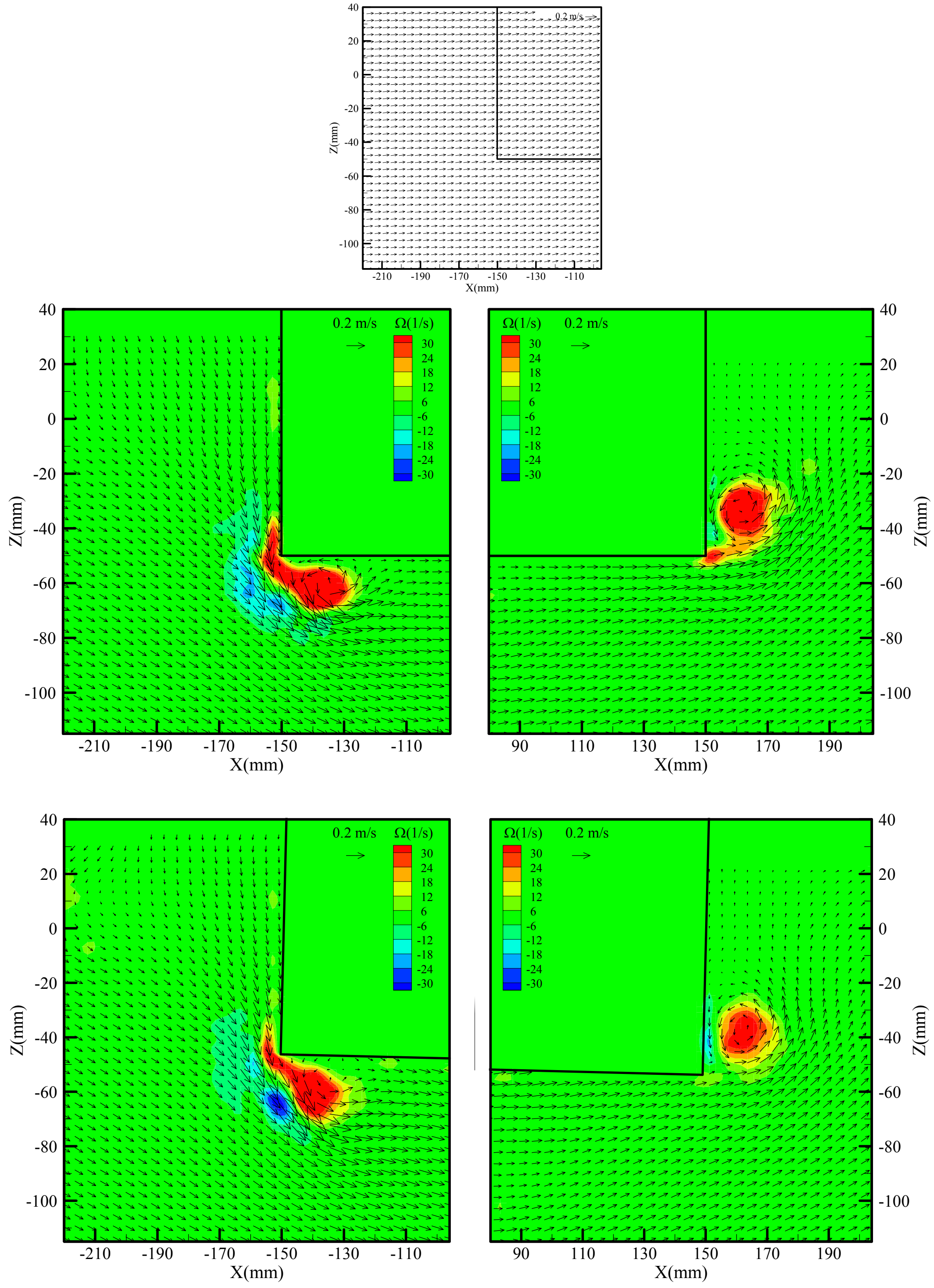

(e) Phase 5

Fig. 6.17 Continued

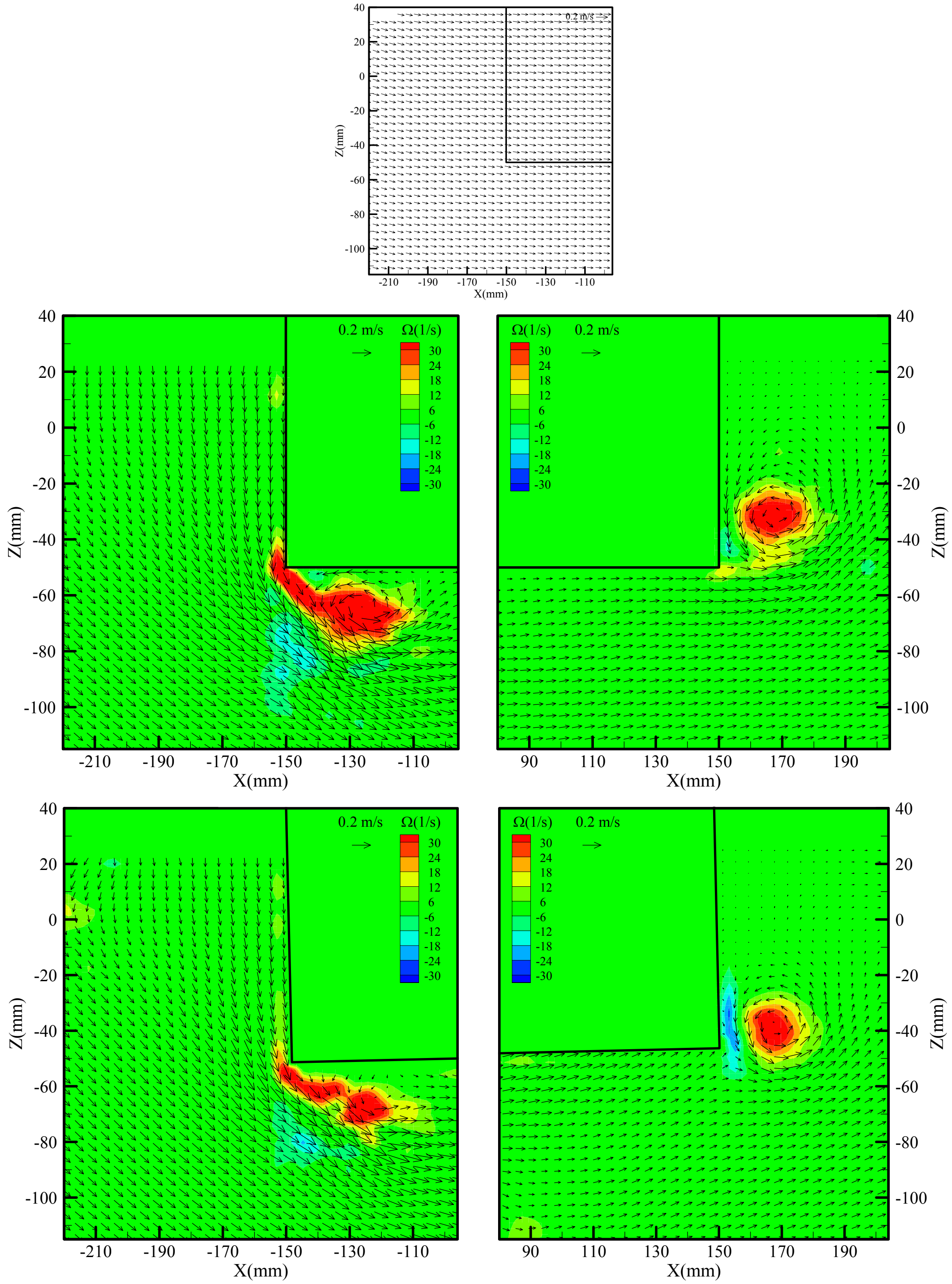

(f) Phase 6

Fig. 6.17 Continued

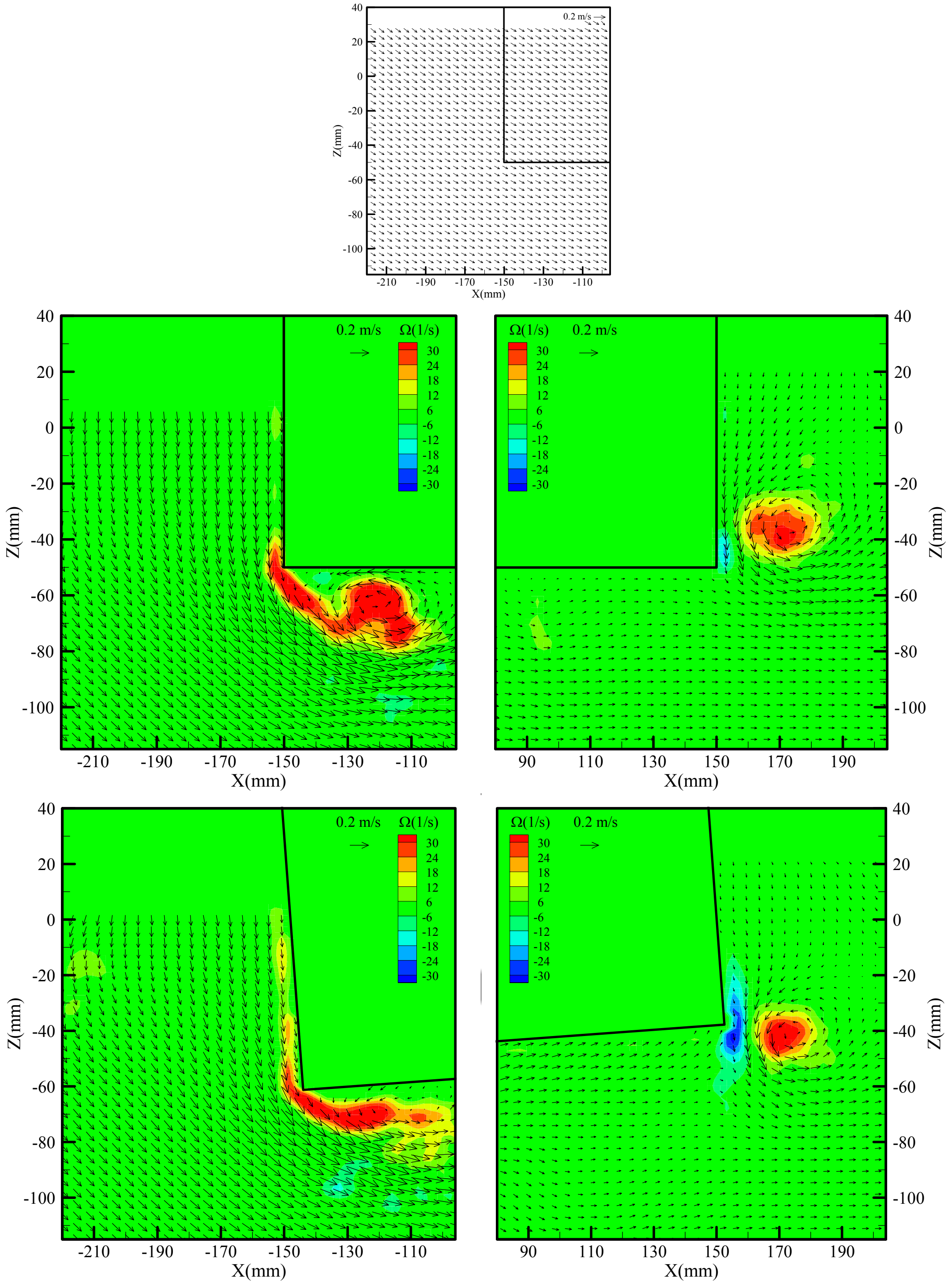

(g) Phase 7

Fig. 6.17 Continued

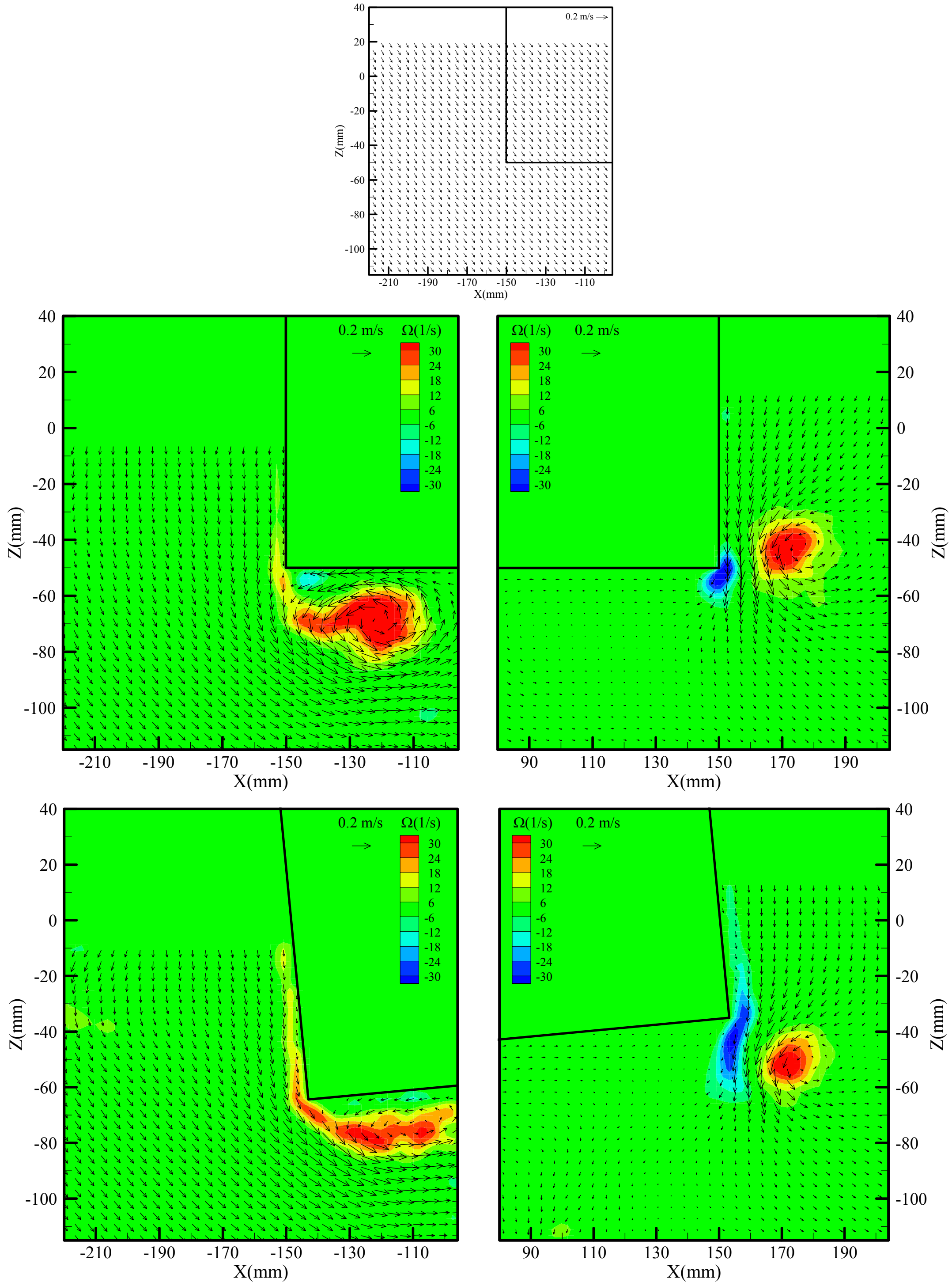

(h) Phase 8

Fig. 6.17 Continued

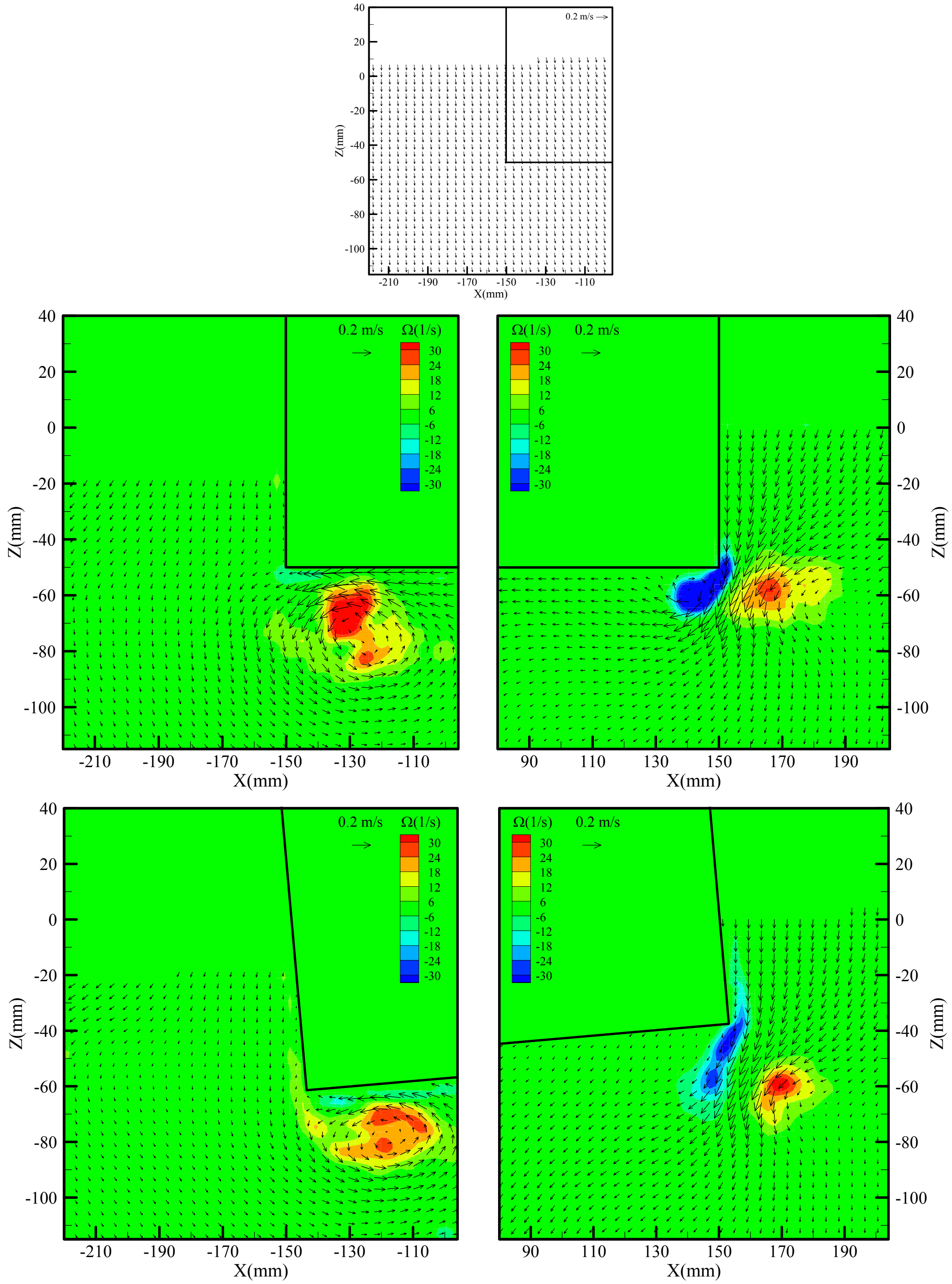

(i) Phase 9

Fig. 6.17 Continued

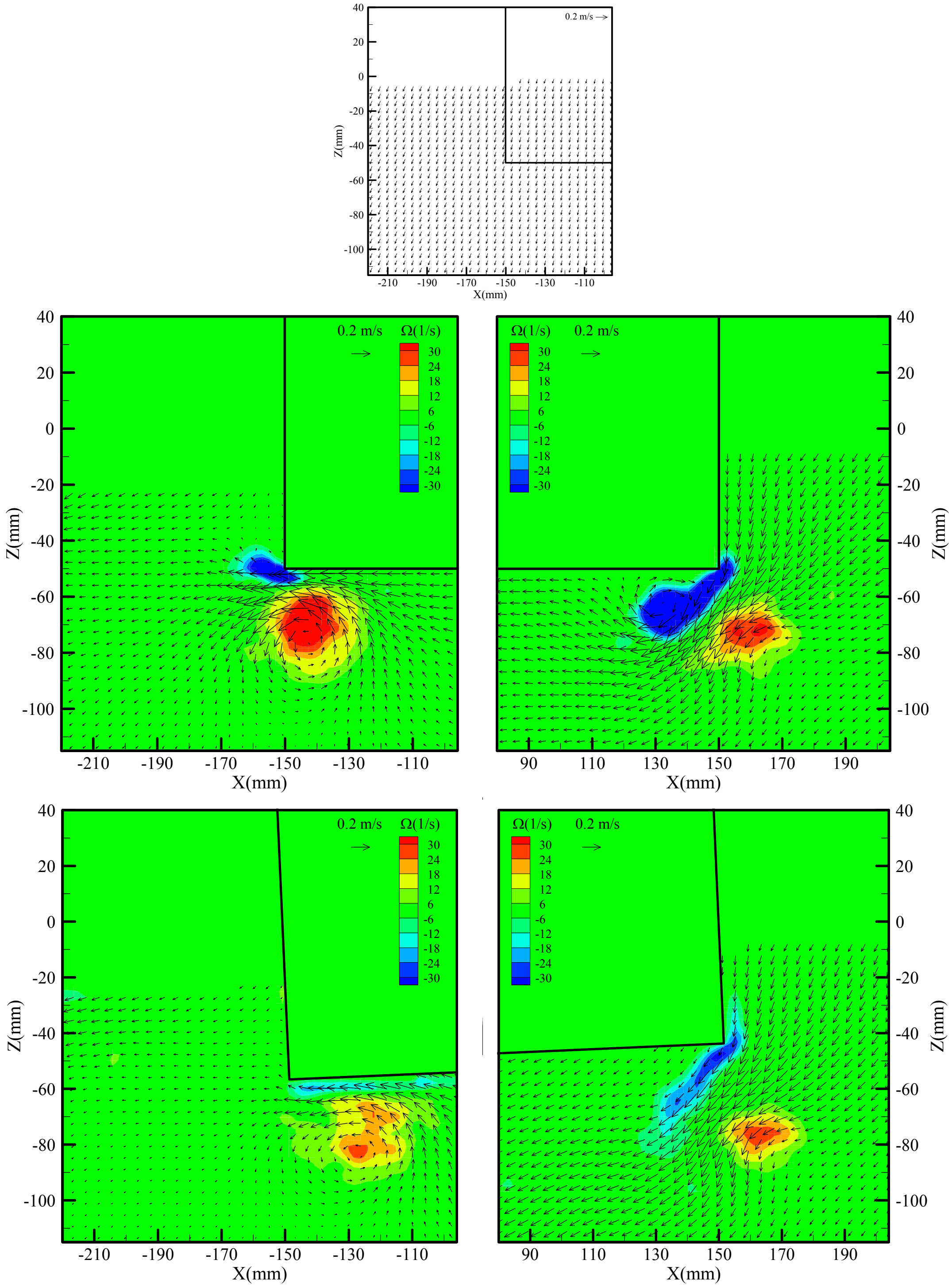

(j) Phase 10

Fig. 6.17 Continued

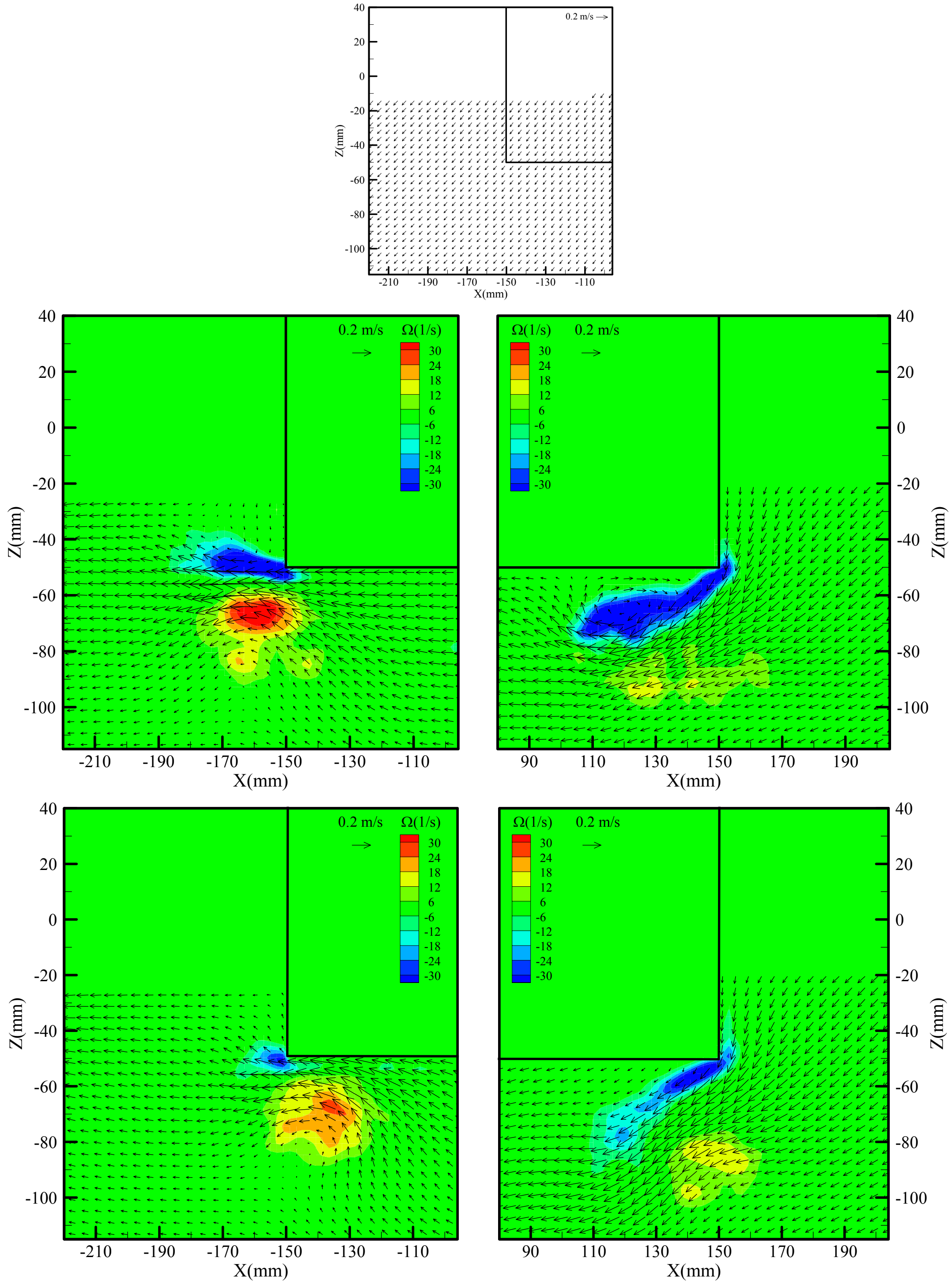

(k) Phase 11

Fig. 6.17 Continued

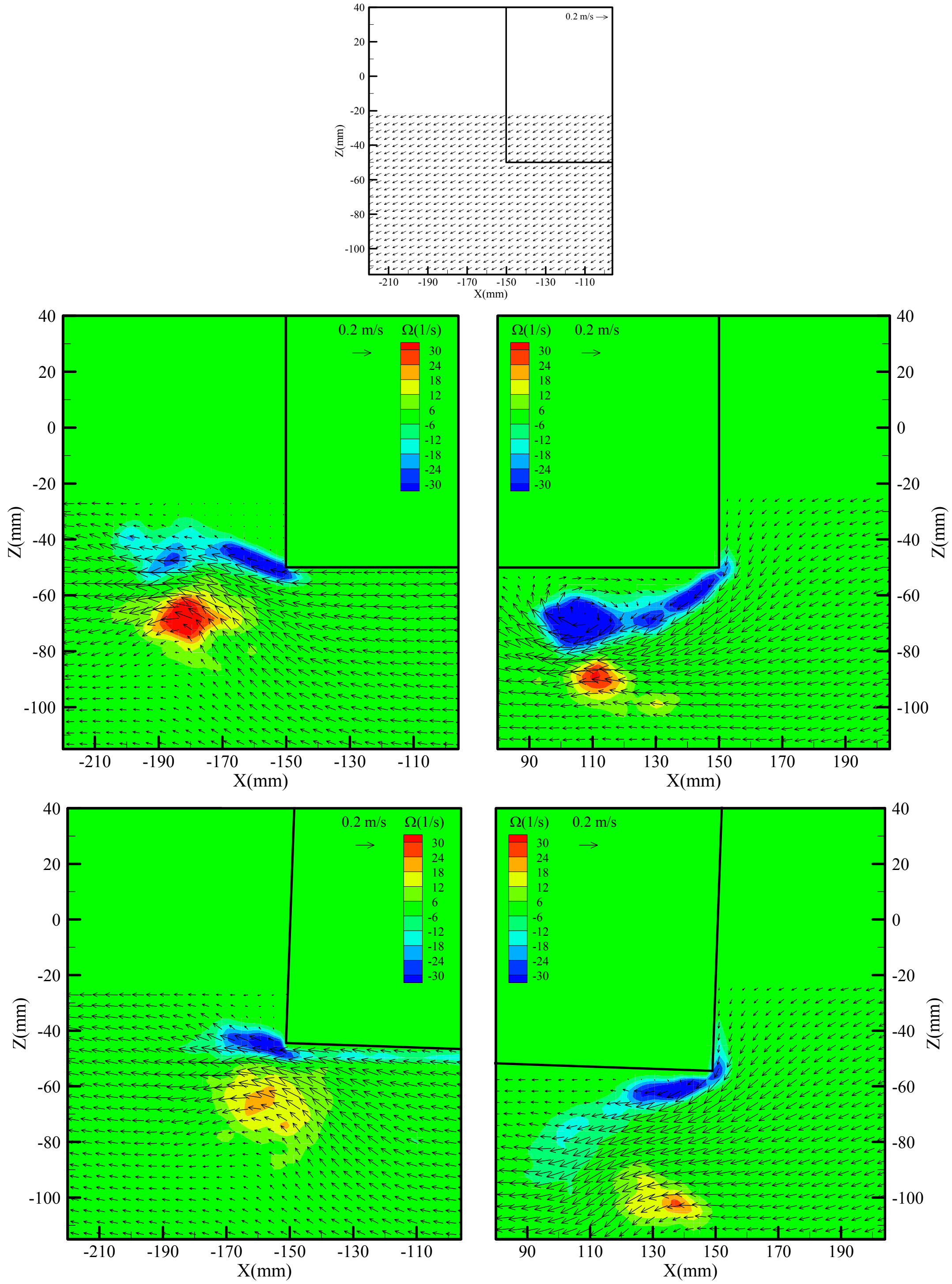

(l) Phase 12

Fig. 6.17 Continued

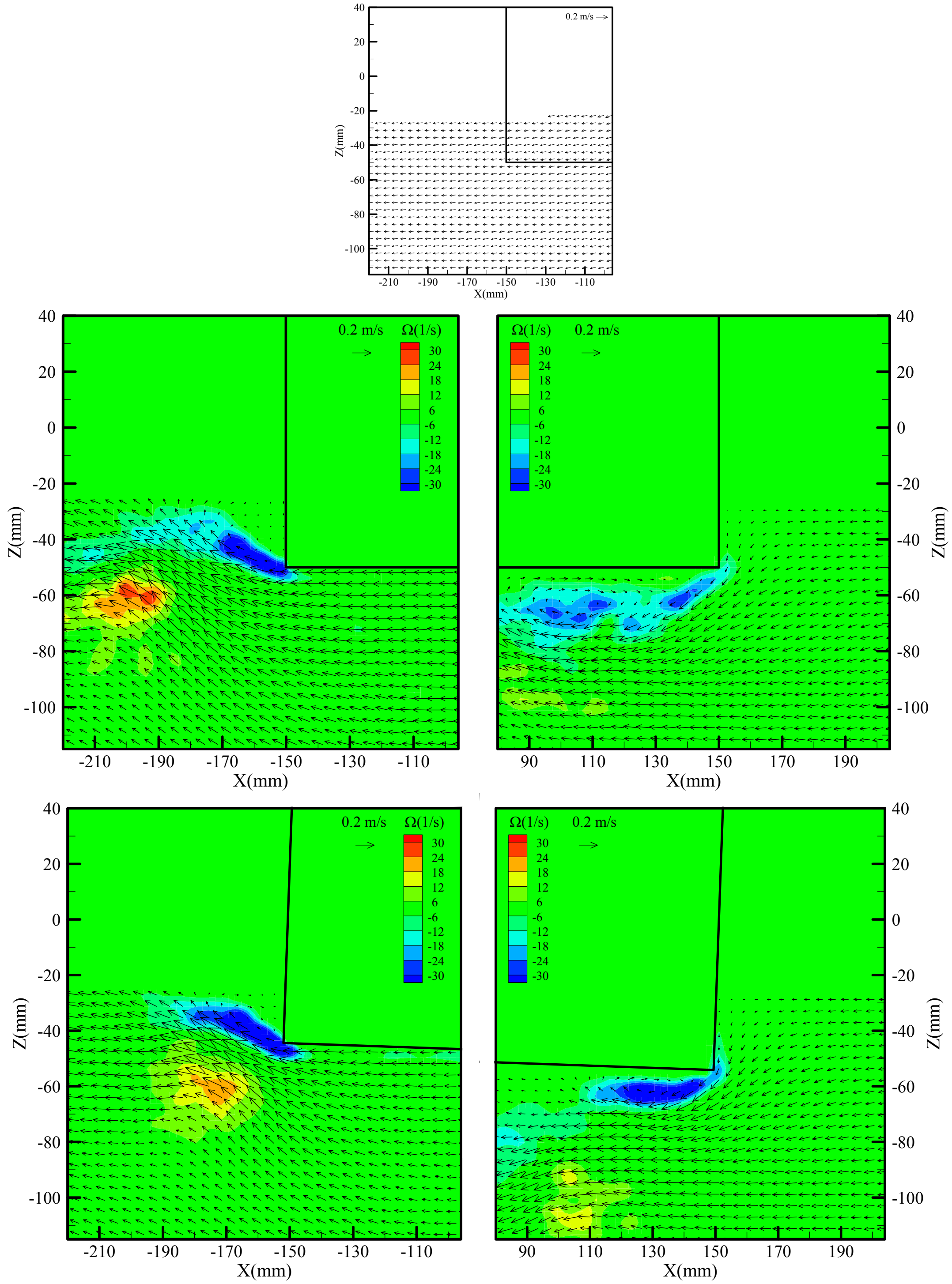

(m) Phase 13

Fig. 6.17 Continued

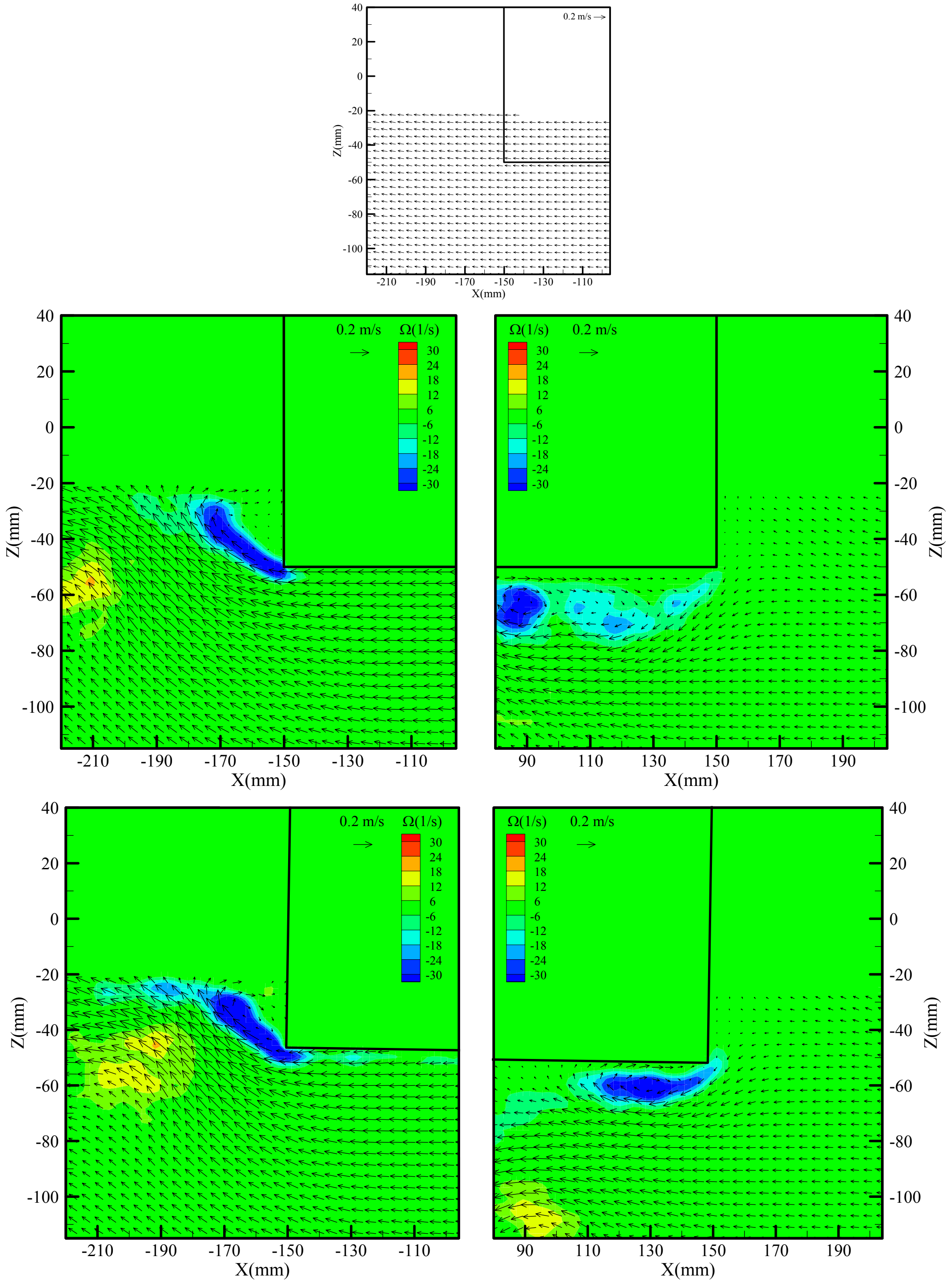

(n) Phase 14

Fig. 6.17 Continued

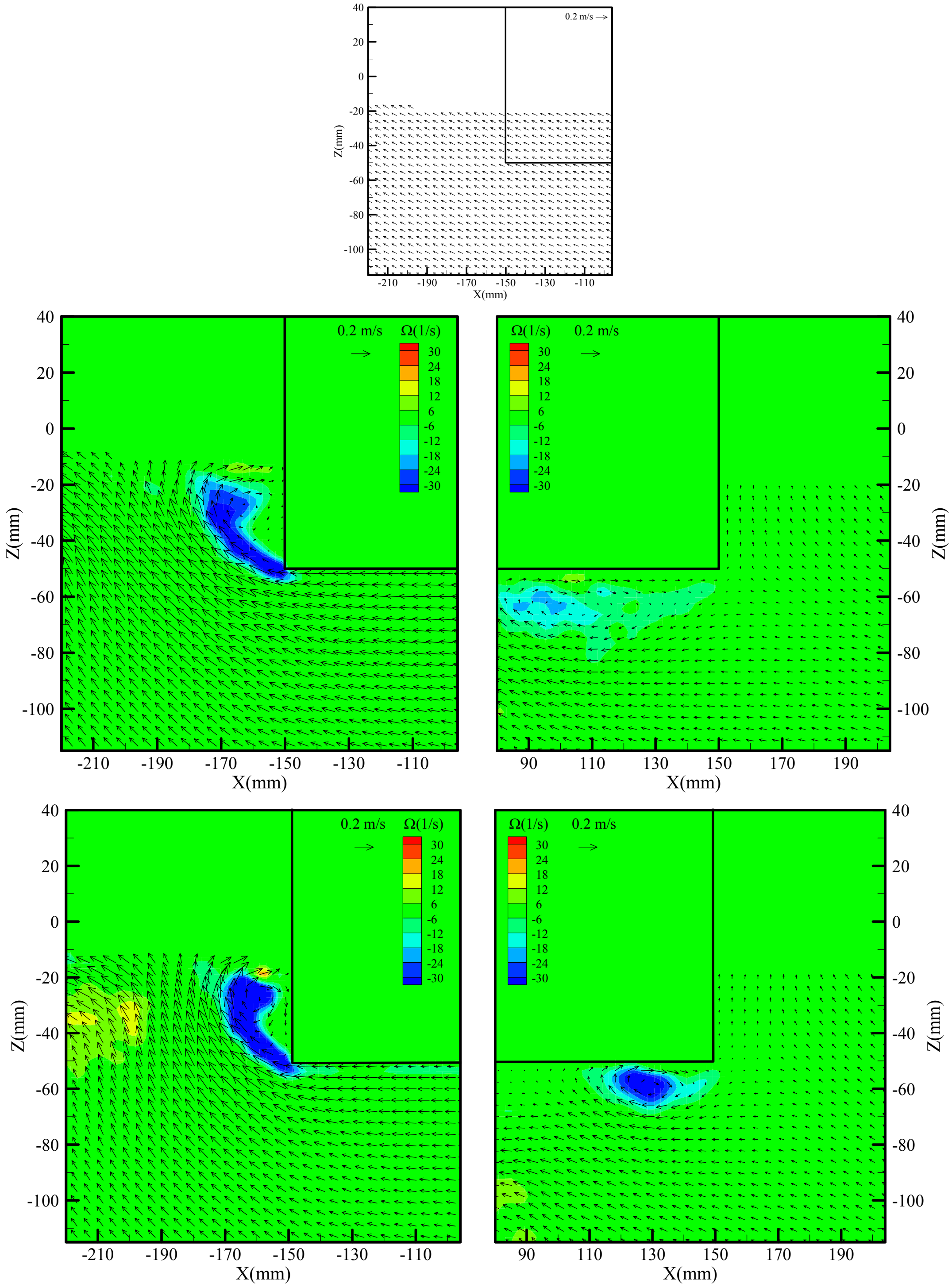

(o) Phase 15

Fig. 6.17 Continued

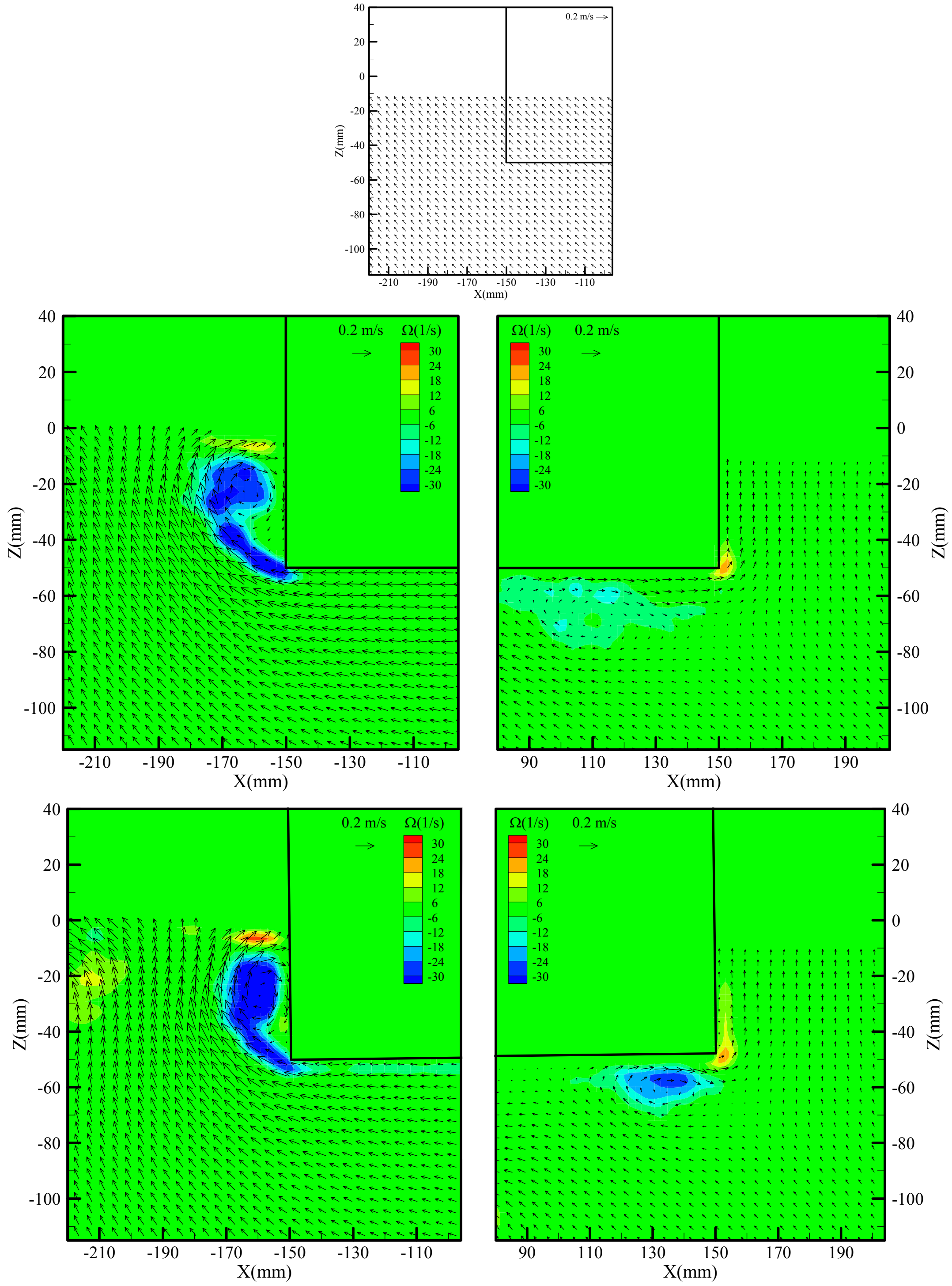

(p) Phase 16

Fig. 6.17 Continued

6.7.3 Shorter period (T=0.8 s) wave than roll natural period

It was experimented to investigate the shorter period wave (T=0.8 s) than the roll natural frequency in Fig. 6.18. Because the transmission coefficient (K_T= 0.45) was small and a transmitted wave were small, the most portion of vortex at the leeward side was generated by the barge motion. The phase of the roll motion versus the incident wave came to be different with the cases of other waves. Unlike other wave, the barge was rolled in the clockwise direction when the free surface of the seaward side came down. As a result, the vortices in the roll motion were larger and stronger than those of the fixed barge. When the barge started to be inclined to the counterclockwise direction at phase 1, the negative vortex developed from phase 6 was mostly decayed and the positive vortex was initiated at the corner of the leeward side. While the positive vortex was developed in the circular shape at the trough of wave in the seaward side (phase 2), the negative vortex began to be separated by the counterclockwise roll motion. It is represented that the negative vortex of the leeward side was mainly caused by the roll motion in comparison with the fixed barge. At phases 3 and 4, the increasing free surface helped the generation of the negative vortex at the seaward side. Although the free surface still rose, the negative vortex was decayed by the clockwise roll motion. The positive vortex was separated by the roll motion at the corner (shown in phase 6). From phase 7, the descending free surface aided to generate the positive vortex at the seaward side. Also, the positive vortex was evolved by the roll motion. That is to say, the vortex evolution at the seaward side were initiated by the roll motion and helped by the free surface motion. The induced dynamic pressure ($P2_D$) on the bottom of the seaward side was changed in its phase and magnitude by the roll motion, which retarded the roll motion. In addition, the induced dynamic pressure ($P3_D$) of the leeward side was mainly caused by the roll motion and resisted the roll motion. It seems that the flow separation due to the roll motion has an effect on the viscous roll damping to reduce the roll motion. However, it was not noticeable (shown in Fig. 6.9) that the roll motion was reduced by the viscous roll damping at the lower period wave than the roll natural period.

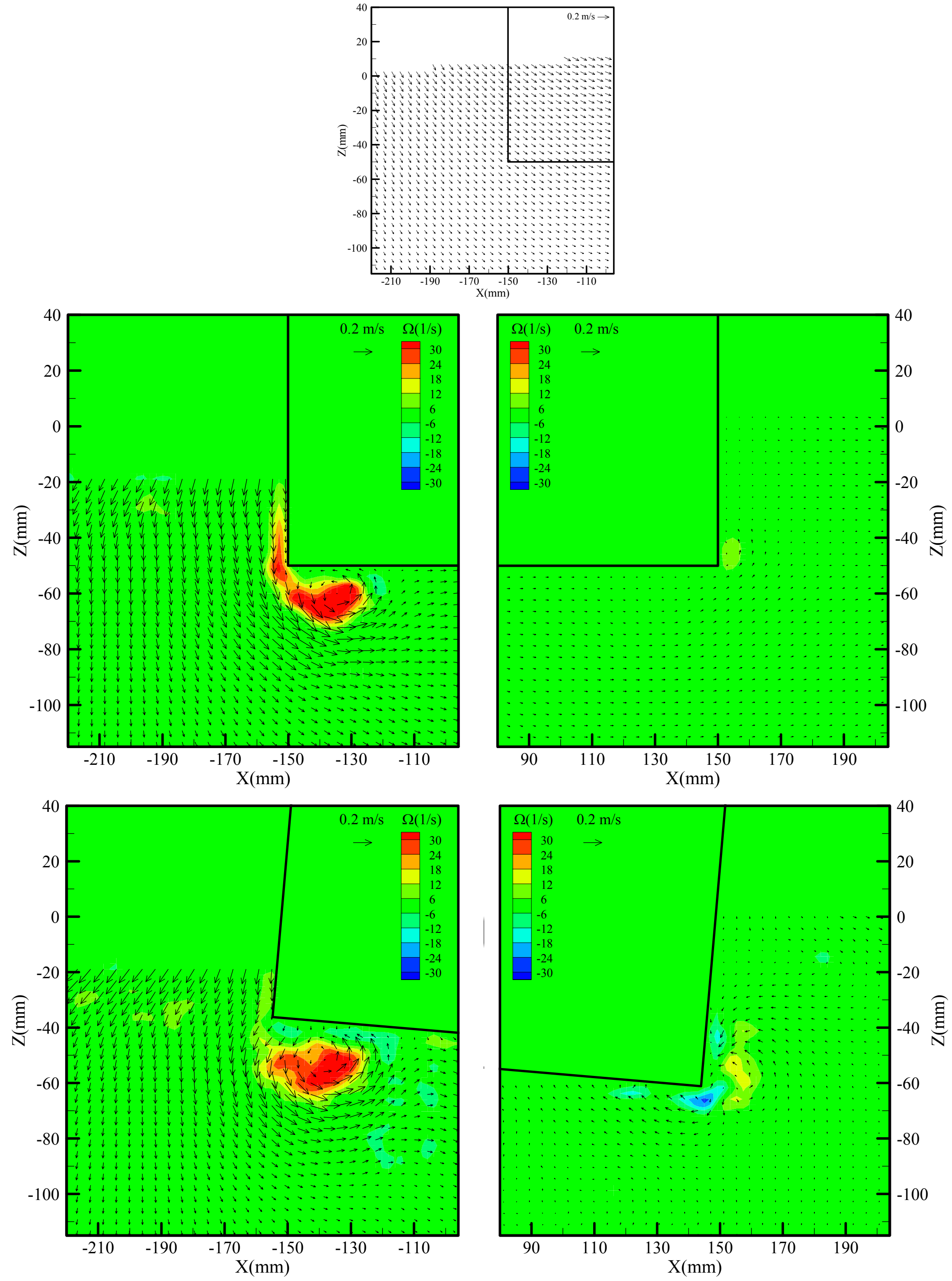

(a) Phase 1

Fig. 6.18 Mean velocity and vorticity (*T*=0.8 s) of the incident wave without the barge (the first row), the fixed barge (the second row), and the barge in roll motion (the third row). Left column: seaward side; right column: leeward side.

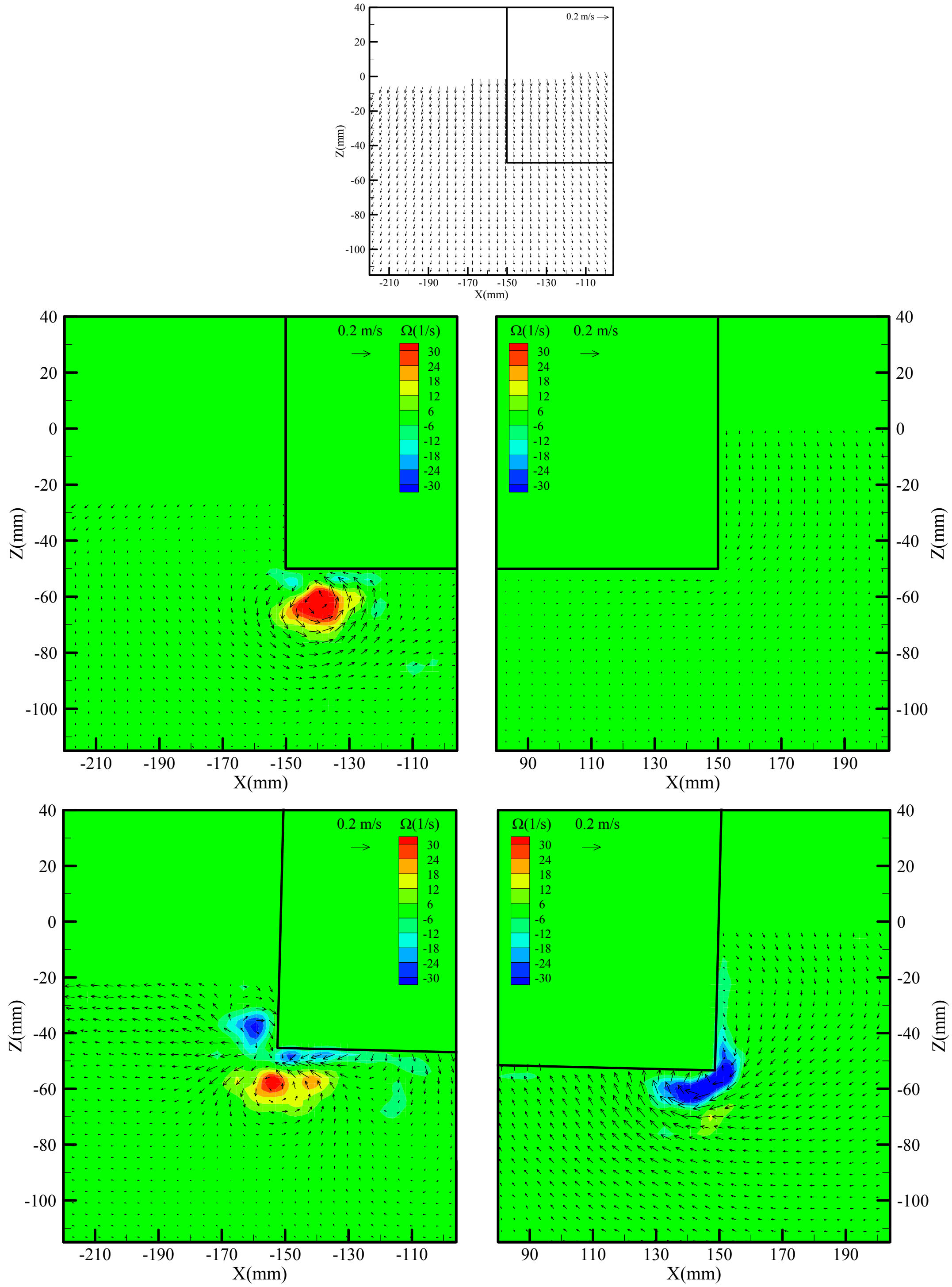

(b) Phase 2

Fig. 6.18 Continued

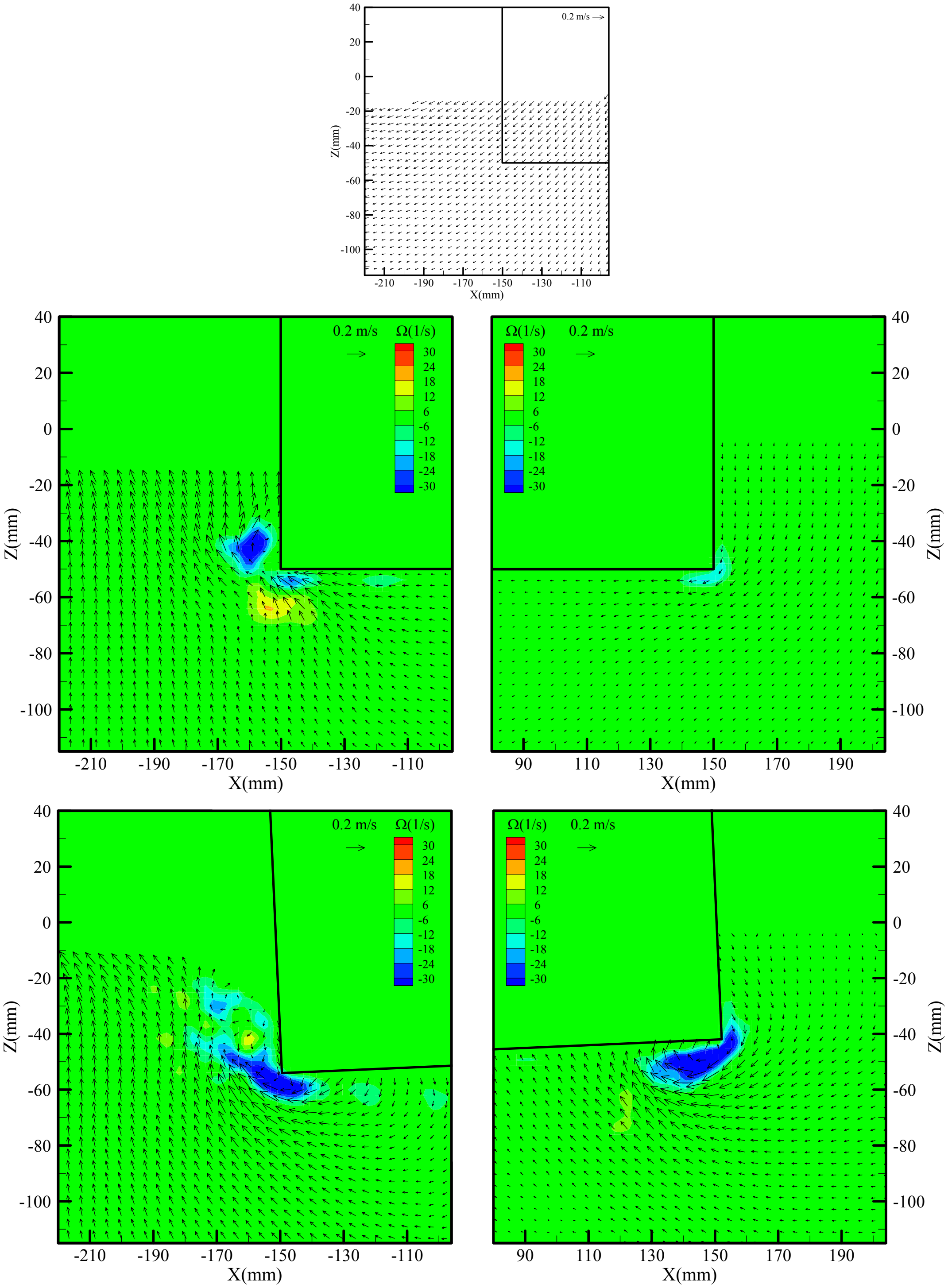

(c) Phase 3

Fig. 6.18 Continued

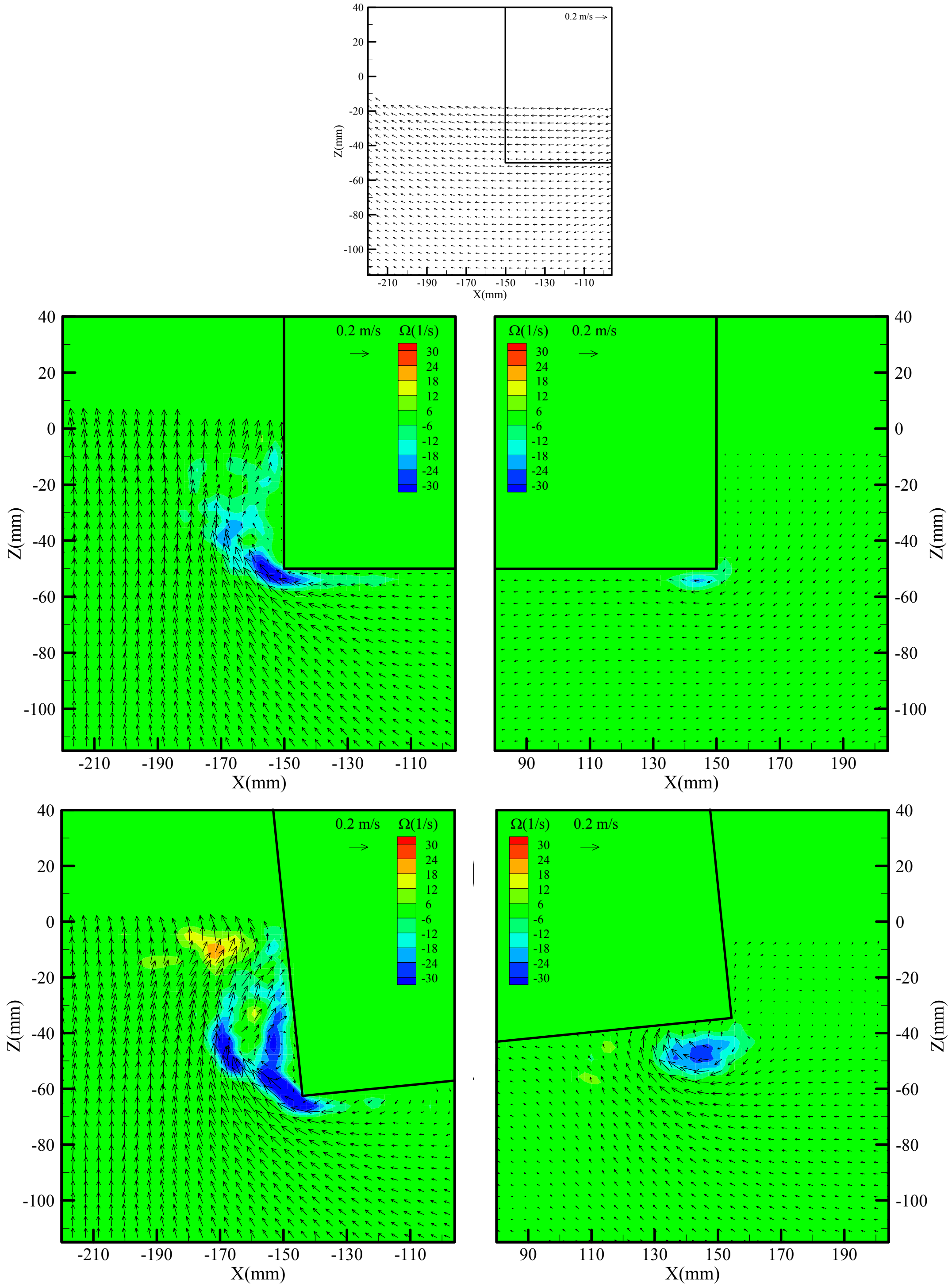

(d) Phase 4

Fig. 6.18 Continued

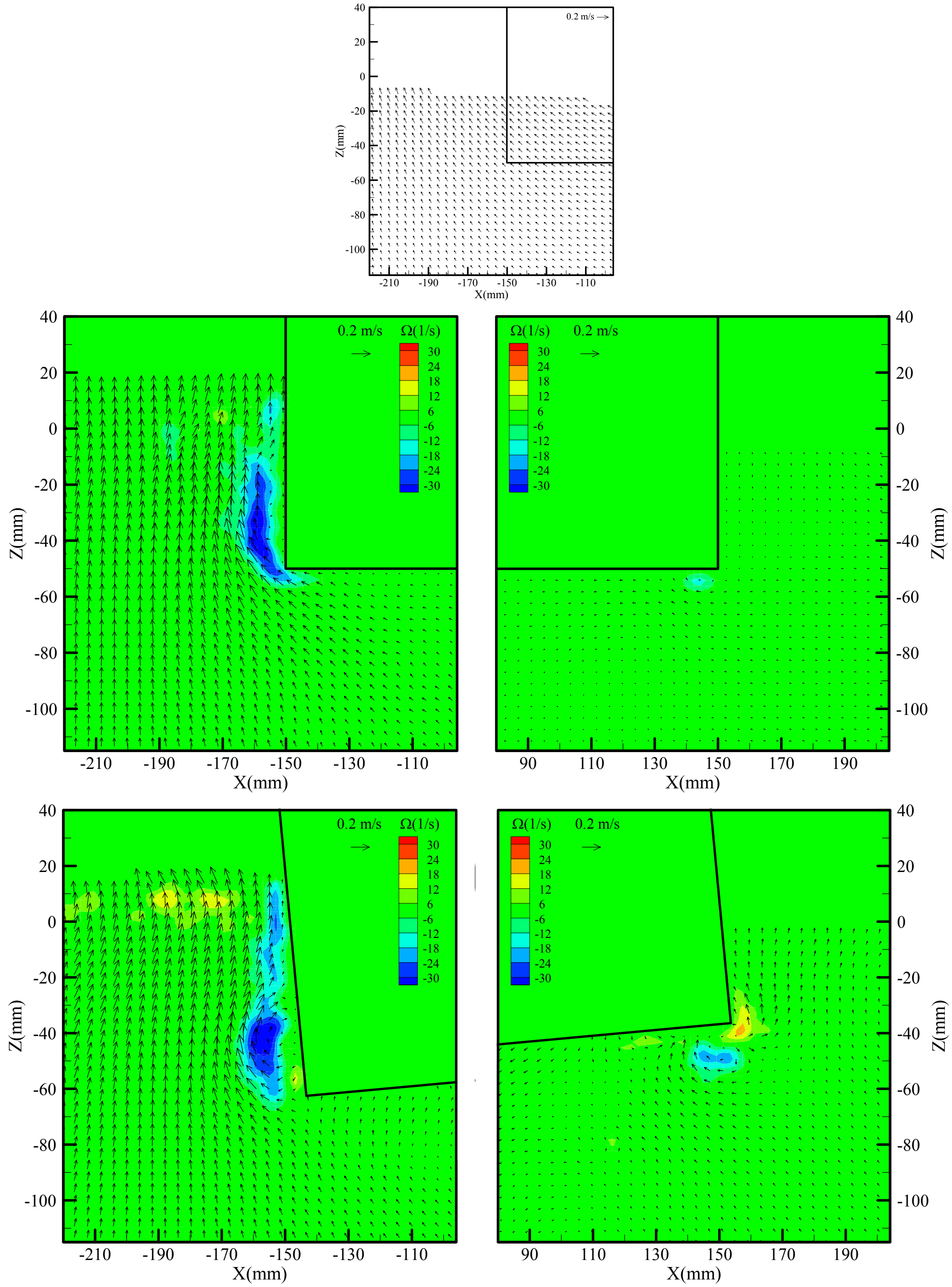

(e) Phase 5

Fig. 6.18 Continued

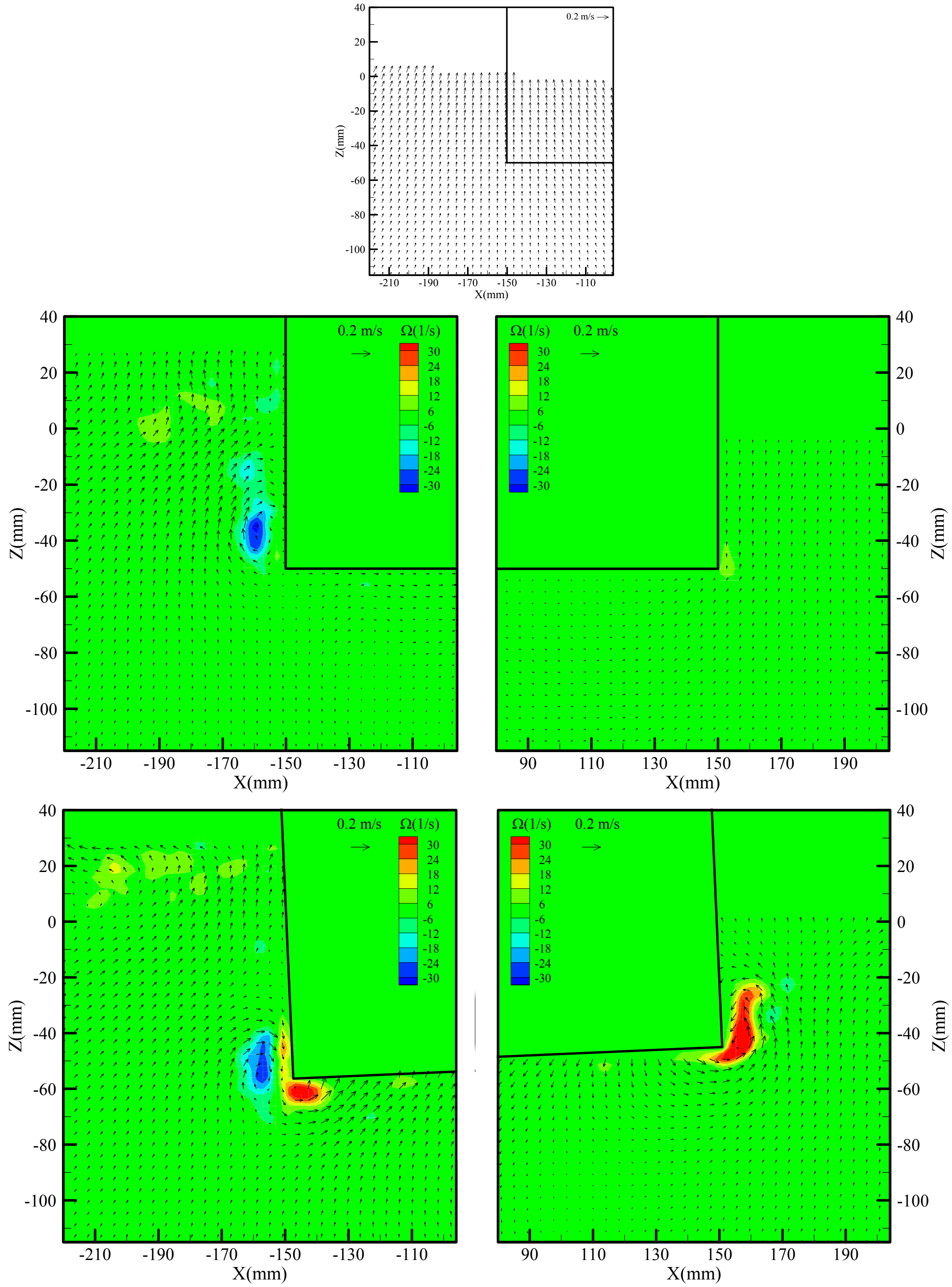

(f) Phase 6

Fig. 6.18 Continued

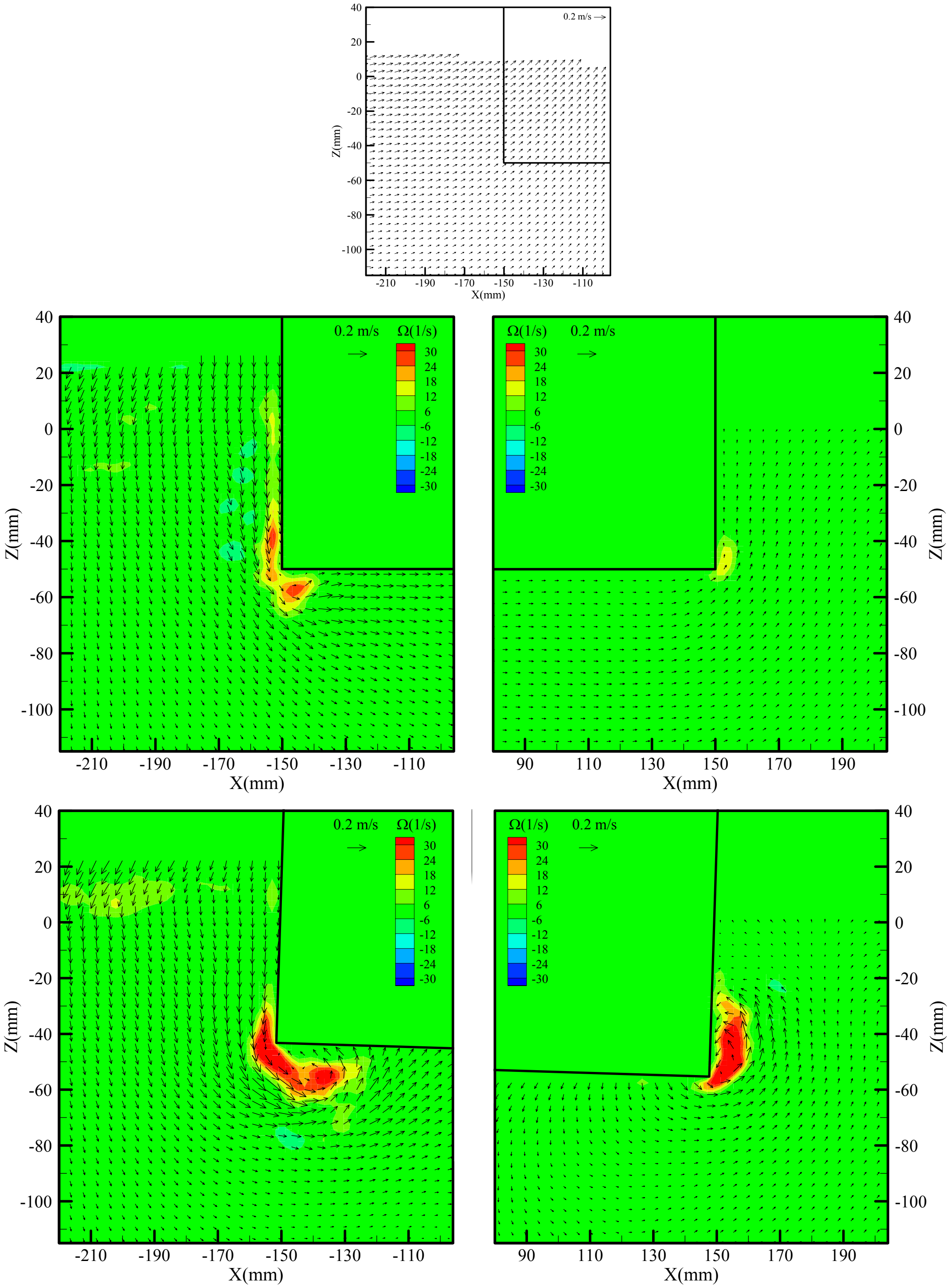

(f) Phase 7

Fig. 6.18 Continued

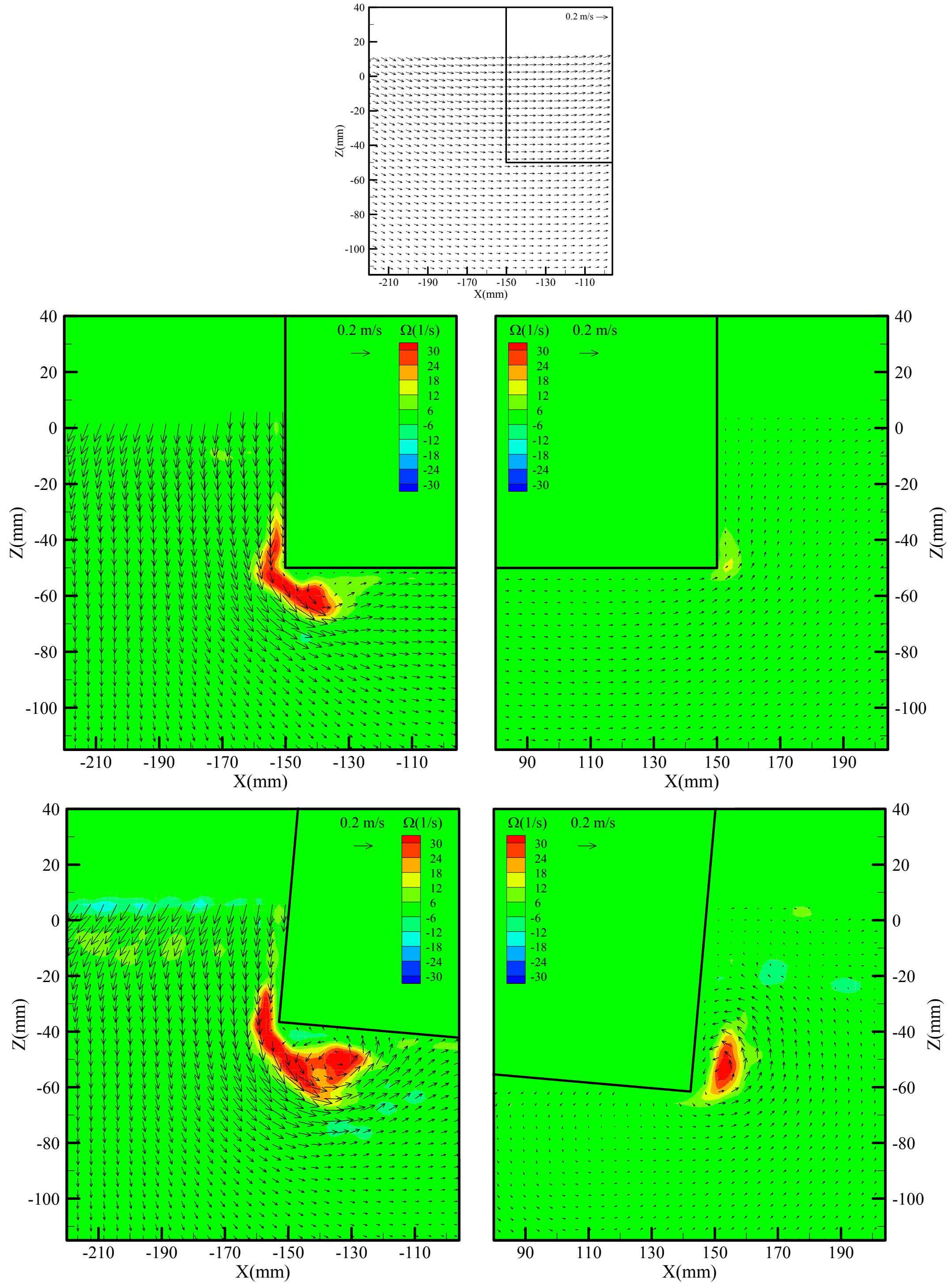

(g) Phase 8

Fig. 6.18 Continued

Because the magnification factor of roll motion was smaller and the vortex generated by the roll motion was less than those of the roll natural period, it was not considerable that the viscous effect due to the vortex came into the reduction of the roll motion.

CHAPTER VII

CONCLUSIONS

An experimental study was performed on the regular wave interactions with a two-dimensional rectangular barge in the fixed condition and the roll motion in a beam sea. The vortex and turbulence due to the wave interaction with the floating rectangular barge were generated and evolved by the water particle motion and the barge motion. To investigate the viscous roll damping effect in the wave condition, the flow pattern in the roll motion was compared with that in the fixed condition. This rectangular barge may be applied to the floating breakwater. The wave transmission coefficient, which represents the efficiency of the breakwater, was lower for the shorter wave period and higher for the longer wave period. The free rolling breakwater is more efficient than the fixed breakwater for the longer period wave than the roll natural period because the transmitted wave may be canceled out with the radiated wave by the roll motion.

The positive and negative vortices were generated due to the flow separation at the corners, migrated in each distinct open trajectory. These vortices caused the rotational and turbulent flow in the vicinity of the barge. Because the rotational and turbulent region was confined within a couple of the water particle trajectory length from the barge surface, the potential flow theory may be applicable out of such region. The turbulent region was relatively larger than the rotational region since the strength of vortex was canceled with the neighborhood counter-rotating vortex. The vorticity and turbulent kinetic energy were stronger at the seaward side than those at the leeward side of the fixed barge because the leeward side interacted with the only transmitted wave. For the longer wave period than the roll natural period, the level of turbulence intensity over the maximum mean velocity at the phase of the strongest turbulence was about 25% for the flow around the barge in roll motion, which was about one-half of the value in wave interactions with a fixed barge. There was the reason in that the relative water particle velocity to the barge corner in roll motion was slower than that in the fixed condition because the barge was inclined into the same direction with the water particle motion. On account of this reason, the vorticity level in the case of roll motion was also lower than that of the fixed barge for the longer wave period than the roll natural period. The integral length scale was similar with the size of vortex separated from the barge corner. Each term in the turbulent kinetic energy budget was measured except the pressure transport term and the viscous dissipation term (being neglected). Turbulent dissipation was estimated with the isotropic dissipation assumption and the balance of the turbulent kinetic energy budget which were comparable results between them.

With the comparison of the velocity profiles of the incident wave and the wave interactions with the fixed barge and the barge in roll motion, it was clearly illustrated that the flow pattern of incident wave was deformed by the fixed barge and the roll motion. In addition, the viscous roll damping (eddy making damping) effect has arisen with the flow separation from both corners at the roll natural period. The flow was separated to the opposite direction of the roll motion in the roll natural period wave. This has been known as the typical viscous damping effect due to the vortex shedding. It was shown at the roll natural period wave that the viscous roll damping effect reduced the roll motion and became noticeable with the increase of wave amplitude. Namely, the viscous roll damping effect led obviously to reduce the roll motion in the roll natural period wave. For the longer period wave than the roll natural period, although the vortex was evolved by both of the water particle motion and the roll motion of barge, the water particle motion mainly contributed to the vortex generation. Therefore, it was similar with that of the fixed barge and did not help in the reduction of the roll motion. In the case of shorter period wave than the roll natural period, the barge was inclined in the opposite direction of the free surface elevation at the seaward side, unlike the other period waves. At the seaward side, the vortex started to be separated by the roll motion and enhanced by the water particle motion. The vortex at the leeward side was mainly generated by the roll motion. Even though the viscous roll damping effect came with the vortex generated by the roll motion, its effect may not be large enough to reduce the roll motion because the roll motion was of relatively small amplitude. The induced dynamic pressure had a similar magnitude with the water level dynamic pressure near the barge corner. The induced dynamic pressure did not only depend on the existing vortex, but the synthetic result of such as the flow pattern and the roll angle. It was periodically changed about in-phase on the side wall and the bottom. For the only roll natural period wave, the pattern of induced dynamic pressure resisted the roll motion and was out of phase on the bottom of both corners, which may imply the viscous roll damping effect.

In conclusion, the vortex was generated by the wave interaction with the floating barge and had an effect on its motion. The vortex in roll motion has been known as the source of the viscous roll damping effect. However, the vortex generation has come from the relative motion of the barge corner to the water particle motion of wave. Because the direction and magnitude of vortices are the function of the wave period and height, the roll natural period and the shape of barge, and the incident angle of wave to the barge, they varied with the wave period if the geometric characteristics of the barge and the wave direction are determined. Particularly, the direction of vortex is determined by the wave period in a beam sea in this study. For the roll natural period waves, the vortex was generated by the barge motion, which was known as the viscous roll damping effect. For the longer period waves, however, the vortex was developed by the wave motion. It may be named as a viscous roll exciting effect since the vortex seemed to help the roll motion.

CHAPTER VIII

RECOMMENDATIONS FOR FUTURE STUDY

The viscous roll damping effect has been a notorious problem in predicting the roll motion of floating structures in an ocean environment. A number of researchers have tried to explain its mechanism and to quantify its effect for the roll motion in the still water condition. It is well-known that the viscous roll damping effect becomes important as the roll motion increased. The severe roll motion of a ship may occur in a certain wave condition, especially in the beam sea condition. To estimate the behavior of roll motion with the more realistic situation, it is recommended to study the floating structure excited by the waves and relatively responded to the waves. Because the barge was allowed only the roll motion in this study, it can be different with the real barge motion which is in 6 degrees of motion. Therefore, the free floating structure close to real case is needed to investigate the coupled effect between motions in each direction such as the roll and sway motions and the roll and heave motion. On the basis of these results, vorticity strength is strongly related to the viscous effect. However, it is very difficult to measure the exact or converged vorticity in the experiment since the vorticity level depends on the spatial resolution of velocities. Thus, the numerical simulation may be required to obtain the absolute vorticity magnitude after the comparison with these experimental results. If the velocity and vorticity profiles can be computed with enough spatial and time resolution, it would be a great contribution to quantify the viscous damping or exciting effect on the roll motion of floating structure in the sea condition.

REFERENCES

Adrian R.J., 1995, Limiting resolution of particle image velocimetry for turbulent flow, in *Advances in Turbulence Research-1995*, end Turbulence Research Assoc. Cong. Pohang Inst, Tech., Korea, 1-99

Arunachalam, V.M. and Raman, H., 1982, Experimental studies on a perforated horizontal floating plate breakwater, Ocean Engineering, 9 (1), 35~45.

Bearman, P. W., Downie, M. J., Graham, J. M. R., and Obasaju, F. D., 1985. Forces on cylinders in viscous oscillatory flow at low Keulegan-Carpenter numbers, Journal of Fluid Mechanics, 154, 337-356

Bhattacharyya, R, 1978, Dynamics of Marine Vehicles, John Wiley & Sons, Inc., New York.

Braza, M., Chassaing, P., and Minh, H. H., 1986. Numerical study and physical analysis of the pressure and velocity fields in the near wake of a circular cylinder, Journal of Fluid Mechanics, 165, 79-130.

Browne, L. W. B., Antonia, A., and Shah, D. A., 1987. Turbulent energy dissipation in a wake, Journal of Fluid Mechanics, 179, 307-326

Bruce, L. and McCartney, M., 1985. Floating breakwater design, Journal of Waterway, Port, Coastal, and Ocean Engineering, 111 (2), 304-318.

Chakrabarti, S., 2001. Empirical calculation of roll damping of ships and barges. Ocean Engineering, 28 (7), 915-932.

Chang, K.-A., Hsu, T.-J., and Liu, P.L.-F, 2001. Vortex generation and evolution in water waves propagating over a submerged rectangular obstacle Part I. Solitary waves, Coastal Engineering, 44, 13-36.

Chaplin, J. R., 1981. On the irrotational flow around a horizontal cylinder in waves, Journal of Applied Mechanics, 48, 689-694.

Chaplin, J. R., 1993. Orbital flow around a circular cylinder. Part 2. Attached flow at larger amplitudes, Journal of Fluid Mechanics, 246, 397-418

Chen, H.C., Liu, T, Chang, K.A., and Huang, E.T., 2002. Time-domain simulation of barge capsizing by a Chimera Domain Decomposition Approach, 12th International Offshore and Polar Engineering Conference, KitaKyushu, Japan, May 26-31, 314-321.

Cozen. P.D., 1987. Numerical modeling of the roll damping of ships due to vortex shedding. Ph.D dissertation. London University, U.K.

Dabiri, D. and Gharib, M., 1997. Experimental investigation of the vorticity generation within a spilling water wave, Journal of Fluid Mechanics, 330, 113-139.

Dong, R.R., Katz, J., and Huang, T.T., 1997. On the structure of bow waves on a ship model. Journal of Fluid Mechanics, 346, 77-115.

Downie, M.J., Bearman, P.W., and Graham, J.M.R., 1988, Effect of vortex shedding on the coupled roll response of bodies in waves. Journal of fluid mechanics, 189, 243~261.

Fugazza, M. and Natale, L., 1988. Energy losses and floating breakwater response, Journal of Waterway, Port, Coastal, and Ocean Engineering, 114 (2), 191-205.

Hughes, S.A., 1993. Physical Models and Laboratory Techniques in Coastal Engineering, World Scientific Publishing, Singapore.

Ikeda, Y., Hemeno, Y., and Tanaka, N., 1977. On eddy making damping component of roll damping force on naked hull. Journal of the Society of Naval Architects of Japan, 142, 54~64 (in Japanese)

Jung, K.H., Chang, K.A., Chen, H.C., and Huang, E.T., 2002. Experimental study on wave interactions with a fixed rectangular barge in a beam Sea, 12th International Offshore and Polar Engineering Conference, KitaKyushu, Japan, May 26-31, 363-370.

Jung, K.H., Chang, K.-A., and Huang, E.T. 2004. Two-dimensional flow characteristics of wave interactions with a fixed rectangular structure. Ocean Engineering, accepted.

Lighthill, J., 1986. Fundamentals concerning wave loading on offshore structures, Journal of Fluid Mechanics, 173, 667-681

Mays, T. W., Plaut, R. H., and Liapis, S. I., 1999. Three-dimensional analysis of submerged, moored, horizontal, rigid cylinders used as breakwaters, Ocean Engineering, 26 (12), 1311-1333.

Oshkai, P. and Rockwell, D., 1999. Free surface wave interaction with a horizontal cylinder, Journal of Fluids and Structures, 13, 935-954

Pope, S. B., 2000. Turbulent Flows, Cambridge University Press, Cambridge

Prasad, A.K., Adrian, R.J., Landreth, C.C., and Offutt, P.W., 1992. Effect of resolution on the speed and accuracy of particle image velocimetry interrogations, Experiments in Fluids, 13, 105-116.

Raffel, M., Willert, C.E., and Kompenhans, J., 1998. Particle Image Velocimetry, Springer-Verlag, Berlin.

Roddier, D., Liao, S.-W., and Yeung, R.W., 2000. On freely-floating cylinders fitted with bilge keels. 10th International Offshore and Polar Engineering Conference, Seattle, USA, May 28-June 2, 377~384.

Rood, E. P., 1994. Interpreting vortex interactions with a free surface, Journal of Fluids Engineering, 116, 91-94.

Salvesen, N. Tuck, E.O., and Faltinsen, O.M., 1970, Ship motions and sea loads. Trans. SNAME, 78, 250~287.

Sarpkaya, T., 1968. An analytical study of separated flow about circular cylinders. Journal of Basic Engineering, 90, 511-520.

Sarpkaya, T., 1989. Computation methods with vortices. Journal of Fluids Engineering, 111, 5-52.

Svendsen, I.A., 1987. Analysis of surf zone turbulence. Journal of Geophysical Research 92C, 5115-5124.

Tennekes, H. and Lumley, J. L., 1972. A First Course in Turbulence, MIT Press, Cambridge.

Townsend, A.A., 1956. The Structure of Turbulent Shear Flow, Cambridge University Press, London.

Unal, M.F., Lin, J.-C., and Rockwell, D., 1997. Force prediction by PIV imaging: a momentum-based approach. Journal of Fluids and Structures, 11, 965-971

Westerweel, J. 1993. Digital particle image velocimetry – Theory and application*,* Ph.D Dissertation, Delft University Press, Delft, The Netherlands.

Westerweel, J. 1994. Efficient detection of spurious vectors in particle image velocimetry data. Experiments in Fluids, 16, 236-247.

Willert, C.E. and Gharib, M 1991 Digital particle image velocimetry. Experiments in Fluids, 10, 181-193.

Williams, A.N. and Abul-Azm, A.G., 1997. Dual pontoon floating breakwater, Ocean Engineering, 24 (5), 465-478.

Williams, A.N., Lee, H.S., and Huang, Z., 2000. Floating pontoon breakwaters, Ocean Engineering, 27 (3), 221-240.

Yeung, R.W., Cermelli C., and Liao, S.-W., 1996. Vorticity fields due to rolling bodies in a free surface - experiment and theory. 21st Symposium on Naval Hydrodynamics, Trondheim, Norway, 359-376.

Yeung, R.W. and Liao, S.-W., 1999. Time-domain solution of freely floating cylinders in a viscous fluid. 9th International Offshore and Polar Engineering Conference, Brest, France, May 30-June 4, 454-462.

Yeung, R.W., Liao, S.-W., and Roddier, D., 1998. Hydrodynamic coefficients of rolling rectangular cylinders. 8th International Journal of Offshore and Polar Engineers, 8, 242-250.

VITA

Kwang Hyo Jung, who is a son of Dae Chul Jung, was born on July 7, 1970, in Pusan, Republic of Korea. He graduated from Pusan National University with a Bachelor of Science degree in naval architecture and ocean engineering in February 1996. He entered the graduate school at Pusan National University in March, 1996 and received a Master of Science degree in naval architecture in February, 1998. In August, 1999, he started the Ph.D study in ocean engineering of the Civil Engineering Department at Texas A&M University and received the Ph.D. in May, 2004. He is married to Mi Jeong Kim and has a son, Ho Joon Jung.

His permanent address is:

141 Naesukri Sangbookmyun, Yangsan

Kyungnam, Korea

e-mail address: will_jung@hotmail.com